Understanding and controlling condensation and frosting phenomena on engineered surfaces

by

Mohammad Rejaul Haque

B.S., Bangladesh University of Engineering and Technology, 2013
M.S., Bangladesh University of Engineering and Technology, 2016

AN ABSTRACT OF A DISSERTATION

submitted in partial fulfillment of the requirements for the degree

DOCTOR OF PHILOSOPHY

Department of Mechanical and Nuclear Engineering
College of Engineering

KANSAS STATE UNIVERSITY
Manhattan, Kansas

2019

Abstract

The significant advancement of micro/nano-structured surface engineering, demands the integration of material science with the heat transfer applications such as condensate harvesting, passive freezing, and frost formation etc. The energy and texture of the solid surface have significant effects on phase change phenomena. This phenomenon is also significantly influenced by environmental factors (temperature and humidity). At atmospheric pressure, a surface below the freezing point temperature for a given relative humidity nucleates water droplets heterogeneously on the surface, and subsequent freezing occurs resulting in frost formation which is a complex and fascinating phenomenon. Frequent defrosting is required to remove the ice that causes substantial economic losses. This work examines the combined effect of surface properties and environmental factors into the fundamental understanding of coalescence and pinning behavior in droplet growth mechanism, and freezing front propagation. Various nano-structured surfaces and engineered surfaces were fabricated to get the different surface energies and texture effects on droplet dynamics. After testing the wetting properties of every individual samples, condensation/freezing tests were conducted on the samples in humidity and temperature controlled chamber. The nanopillar surfaces had a significant effect on droplet dynamics via the pinning mechanism, and reduced the occurrences of coalescence events. Nanopillared surface accelerated freezing by order of magnitude compared to a plain hydrophilic surface at 60% RH. A mathematical model was developed for the pinning mechanism as a function of design parameters (pillar height, spacing, and radius) of the fabricated nanopillar surface. For the condensation test on graphene oxide (GO) coated copper surface, the pinning of droplets into the micro/nanostructures of the surfaces leads to the enhancement of condensate harvesting. The hydrophobic aluminum (Al-H), and hydrophobic graphene coated surface delays

the freezing. The change in freezing kinetics, freezing time, the size of droplets at freezing, and the surface area covered at freezing, are all related to the rate of coalescence of droplets on the surface. Approximate ~6.78×, ~13.12× and ~17.32× freezing delay was observed at 269 K, 270 K, and 271 K surface temperatures respectively for the hydrophobic graphene surface compared to the plain silicon surface under same operating condition. The result promises the applicability of different engineered surfaces for significant energy savings in frost delaying, thermal management, and condensate harvesting applications.

Understanding and controlling condensation and frosting phenomena on engineered surfaces

by

Mohammad Rejaul Haque

B.S., Bangladesh University of Engineering and Technology, 2013
M.S., Bangladesh University of Engineering and Technology, 2016

A DISSERTATION

submitted in partial fulfillment of the requirements for the degree

DOCTOR OF PHILOSOPHY

Department of Mechanical and Nuclear Engineering
College of Engineering

KANSAS STATE UNIVERSITY
Manhattan, Kansas

2019

Approved by:

Major Professor
Dr. Amy Rachel Betz

Copyright

Abstract

The significant advancement of micro/nano-structured surface engineering, demands the integration of material science with the heat transfer applications such as condensate harvesting, passive freezing, and frost formation etc. The energy and texture of the solid surface have significant effects on phase change phenomena. This phenomenon is also significantly influenced by environmental factors (temperature and humidity). At atmospheric pressure, a surface below the freezing point temperature for a given relative humidity nucleates water droplets heterogeneously on the surface, and subsequent freezing occurs resulting in frost formation which is a complex and fascinating phenomenon. Frequent defrosting is required to remove the ice that causes substantial economic losses. This work examines the combined effect of surface properties and environmental factors into the fundamental understanding of coalescence and pinning behavior in droplet growth mechanism, and freezing front propagation. Various nano-structured surfaces and engineered surfaces were fabricated to get the different surface energies and texture effects on droplet dynamics. After testing the wetting properties of every individual samples, condensation/freezing tests were conducted on the samples in humidity and temperature controlled chamber. The nanopillar surfaces had a significant effect on droplet dynamics via the pinning mechanism, and reduced the occurrences of coalescence events. Nanopillared surface accelerated freezing by order of magnitude compared to a plain hydrophilic surface at 60% RH. A mathematical model was developed for the pinning mechanism as a function of design parameters (pillar height, spacing, and radius) of the fabricated nanopillar surface. For the condensation test on graphene oxide (GO) coated copper surface, the pinning of droplets into the micro/nanostructures of the surfaces leads to the enhancement of condensate harvesting. The hydrophobic aluminum (Al-H), and hydrophobic graphene coated surface delays

the freezing. The change in freezing kinetics, freezing time, the size of droplets at freezing, and the surface area covered at freezing, are all related to the rate of coalescence of droplets on the surface. Approximate ~6.78×, ~13.12× and ~17.32× freezing delay was observed at 269 K, 270 K, and 271 K surface temperatures respectively for the hydrophobic graphene surface compared to the plain silicon surface under same operating condition. The result promises the applicability of different engineered surfaces for significant energy savings in frost delaying, thermal management, and condensate harvesting applications.

Table of Contents

List of Figures

List of Tables

List of Abbreviations

CA	Contact Angle
CVD	Chemical Vapor Deposition
CF	Carbon Fibers
CFD	Computational Fluid Dynamics
CNT	Carbon Nanotubes
DPLW	Direct-Pulsed Laser Writing
DwC	Dropwise Condensation
ESEM	Environmental Scanning Electron Microscope
HTC	Heat Transfer Coefficient
IPG	InkJet-Printed Graphene
IER	Institute of Environmental Research
MD	Molecular Dynamics
RH	Relative Humidity
SEM	Scanning Electron Microscope

Nomenclature

d = diameter of liquid droplet (μm)

P = partial pressure of water vapor (Pa)

P_s = pressure of water vapor at saturation (Pa)

ΔG = Gibbs free energy (J)

h_{fg} = latent heat of vaporization (J/Kg)

K_w = thermal conductivity of water (W/mK)

l = bridging length (μm)

R = droplet radius (μm)

R_m = the gas constant for water vapor (J/kgK)

R_c = conduction resistance (W/K)

S = bridging parameter

t = time (s or minutes)

T = temperature (K)

T_w = surface temperature (K)

T_{sat} = saturation temperature (K)

Greek Symbols

γ = surface tension of water in air (mN/m)

θ = apparent contact angle of droplet (°)

ρ_d = droplet density (Kg/m^3)

β = constant

Acknowledgements

I would like to express the deepest appreciation to my advisor Dr. Amy Rachel Betz for her continuous guidance and help for my research. I would like to express my gratitude to my committee members, Dr. Eckels, Dr. Jones, Dr. Hansen, and Dr. Rudenko. In addition, I would like to thank Dr. Kinzel and Dr. Das for their input to my research. I would also like to thank Dr. Eckels and Matt Campbell of IER, for the use of their environmental chambers. I would like to acknowledge Alex, Rachel for their support in building experimental setup and experimentation. At the end, I would also like to give my heartiest love and thanks to my newborn baby Ramisa Haque Rayya; wife, Kazi Shayla Shorme; as well as other friends for their constant support in my pursuit of the PhD Degree.

This work was supported by the National Science Foundation under Grant No. 1604183.

Dedication

This work is dedicated to my mother, Irin Akhtar and my father, Mohammad Aminul Haque. I would also grateful to my brother, Mohammad Merajul Haque. Without their unconditional support, care, and love, I would never have gone this far both in the academic world and in personal life.

Chapter 1 - Introduction

1.1 Condensation

At atmospheric pressure, the surface below the dew point temperature for a specific relative humidity generates water droplets on a surface, known as dropwise condensation (DwC). The field of dropwise condensation has been investigated for many years [1-3]. The heat transfer through a single droplet and for the whole surface has been calculated based on the size distribution of the droplet on that surface [1]. The growth of breath figures has been established when the vapor is condensed on a cold surface. Furthermore, the studies concluded the droplet growth procedure as self-similar, and coalescence did not alter the size distribution. In addition, the study conducted by Rose *et al.* [3] shows the review of the dropwise condensation from 1930 to 2002. The presence of air in the vapor makes it challenging to measure the dropwise heat transfer. The transition of dropwise condensation to film condensation is still not well understood. From a practical point of view, a reliable means of promoting dropwise condensation under industrial conditions have yet need to be convincingly demonstrated [3]. Dropwise condensation of water droplets was investigated by Leach *et al.* [4] on hydrophobic polymer film and silanized glass slide; by conducting both numerical and experimental studies. The condensation rates per unit substrate area were found much higher for areas occupied by smaller droplets compared to larger droplets. Promotion of heat transfer rate might be accomplished by increasing the droplet nucleation density and removing the larger droplets for further renucleation on the surface [4]. Moreover, droplet growth was studied on a super-hydrophobic spike surface and growth stage is characterized by the nucleation of the droplets at the bottom of the spikes, smaller droplets surround the larger droplets, and the last stage is characterized by Wenzel-type droplets [5]. Studies [6-38] have been conducted based on surface

modification inducing different wetting properties such as hydrophobicity, superhydrophobicity, lubricant-impregnated nanotextured, different wettability patterning, nano-engineered materials, water repellent surfaces, and effect of geometric features etc. Chen *et al.* [6] investigated that dropwise condensation can enhance heat transfer by order of magnitude compared to filmwise condensation [6]. They have studied dropwise condensation on a two-tier texture mimicking lotus. On such micro/nano-structured surfaces, the condensate droplets prefer the Cassie state, which is thermodynamically more stable than the Wenzel state [6]. The research [7] stated that the condensed droplet on rough hydrophobic substrates (shown in Figure 1.1) shows different wetting behavior compared to the deposited or impinging droplets on the surface. The promotion of dropwise condensation through effective surface coating by diamond-like carbon films and ion implantation were discussed.

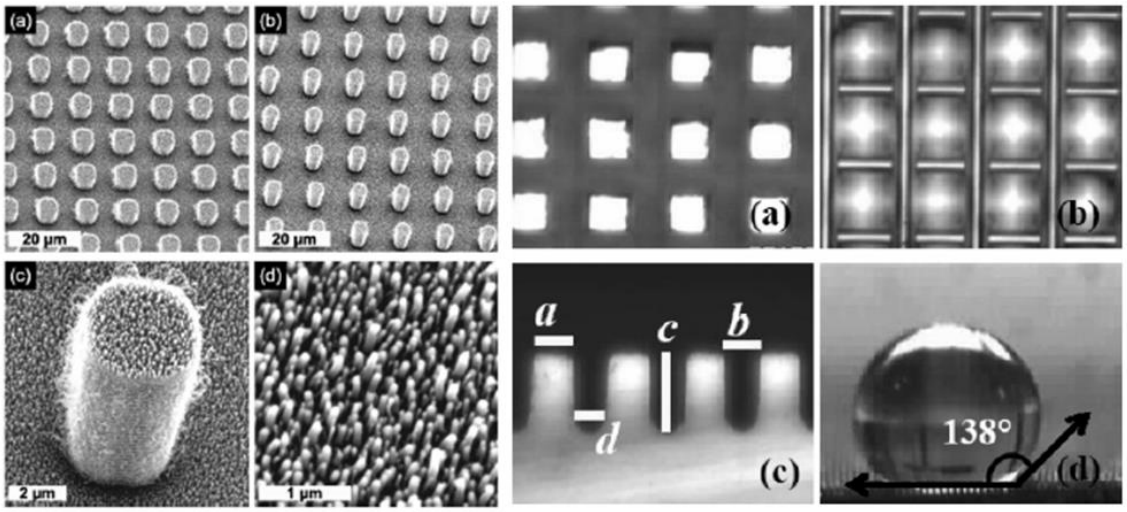

[6] [7]

Figure 1.1 Two-tier textures: micropillars are etched in silicon, and CNT nanopillars are subsequently deposited on the side of the micropillars via CVD. The substrate was then hydrophobicized either by a 10 nm layer of parylene C coating or by a 10 nm layer of gold coated with a monolayer of 1-hexadecanethiol [6]. Optical microscopic image of a square-pillar-patterned silicon substrate [7].

The main parameters that affect the condensation are the surface tension of the condensing fluid, the surface roughness or structure, and the surface energy of the condenser surface [8]; effect of pressure on the evolution of transient condensation [9] and condensation at lower and ultra-lower pressure [10] have also been discussed. Droplet size distribution at different growth stages [9] and the significance of initial droplet size distribution on overall droplet growth [11] have also been discussed. In the study [13], dropwise condensation on textured surfaces, both horizontal and inclined has been modeled mathematically. The model has been represented in terms of thermo-physical properties of liquid and vapor phases, the surface properties, contact angle, and surface tension of the liquids.

Moreover, past studies [14-38] have also been conducted on the nano-engineered surface, superhydrophobic surface, hydrophobic surface, wettability gradient surface etc. to promote condensation for different applications such as energy conversion, condenser unit for power plant, efficient condensate harvesting, and high-performance thermal management. Nanostructured superhydrophobic surfaces [15] have been applied in condensation experiment to elucidate the droplet wetting state and the morphology of the droplet in heat and mass transfer. Nanotechnology has the advantages to manipulate the local energy barrier of heterogeneous nucleation by effective and proper surface structuring. However, the importance of local energy barrier on the droplet growth procedure and nucleation site density for different nanostructured surfaces was also studied. Using environmental scanning electron microscopy (ESEM) images, the growth stages of the droplet has been elucidated in a single cell to the point of coalescence with neighboring droplet shown in Figure 1.2 [16].

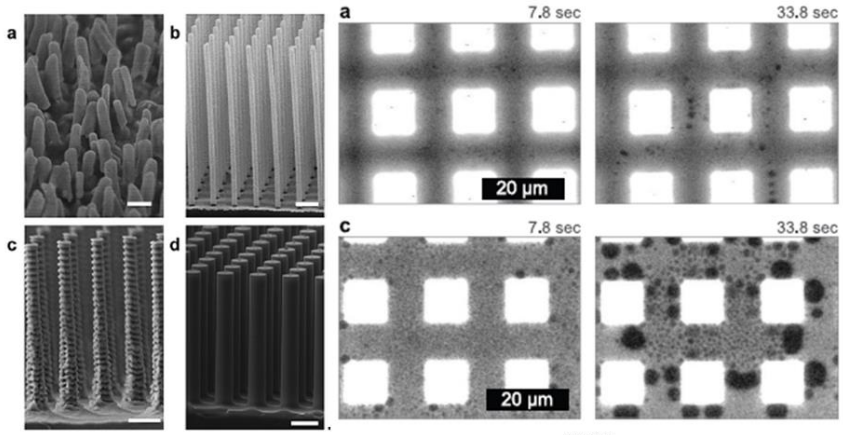

[16] [19]

Figure 1.2 Au and Si nanopillar geometries were fabricated for dropwise condensation applications [16]. ESEM image sequence of condensation on a micropost surface impregnated with (a) Krytox (b) BMIm [19].

The condensation behavior of water on a superhydrophobic carbon fibers (CF) network with high-aspect-ratio hair-like nanostructures has been studied [17]. The surface can prevent the flooding and sustain the dropwise condensation. Likewise, metallic superhydrophobic aluminum surfaces with different low-surface-energy coatings and lubricant-impregnated nanotextured surfaces have also been tested for condensation test, as shown in Figure 1.2 [18, 19]. Failure of droplet shedding from the superhydrophobic surface has also been investigated [20]. Through the environmental scanning electron microscope (ESEM) imaging, a hydrophobic textured surface may appear into a hydrophilic surface when water vapor condenses on the surface, and filmwise condensation happens [24]. Additionally, biotemplated nanostructured surfaces have been fabricated via the self-assembly of the Tobacco mosaic virus combined with initiated chemical vapor deposition technique. The droplet morphology, wetting dynamics, and condensation heat transfer performance of the virus-structured surfaces have been investigated via the role of the local energy barrier [27]. Different wettability gradient surface has been tested to facilitate pumpless liquid drainage in DWC applications [29], and the wettability gradient can decrease the mean size of the droplets to enhance the heat transfer rate [30]. Self-propelled sweeping removal

of dropwise condensate on micropillared surface has been observed [31]. Moreover, numerical modeling, as well as experimental validation, has been conducted via the study of condensed water droplet growth using optical microscopy and ESEM on biphilic samples consisting of hydrophobic and nanostructured superhydrophobic regions [32]. Scalable Cu-based nano-engineered surfaces were fabricated, and microscale droplet formation has been observed. Also, the comparison of heat transfer for hydrophobic and superhydrophobic surfaces was done [33]. Optimal heat transfer surface is estimated based on the measurement of full 3D temperature distribution and interfacial surface area of the droplet via numerical simulation [34]. Nanostructured superhydrophobic surface with tapered nanogaps and nanowired hydrophobic surface is fabricated to demonstrate the wetting state of the condensed droplet with a view to self-cleaning performance, improve anti-icing, and increase thermal diode efficiency [35-36]. On a uniform superhydrophobic surface, the droplet nucleation rate can be increased by the reasonable increase of the nanostructure density [37]. Recently, the effects of millimetric surface structures on DwC under pure vapor and an air-vapor mixture have also been studied. The study concludes that heat transfer mainly depends on the thermal resistances involved in the system [38]. Moreover, surface chemistry to induce hydrophobicity, the scalable coating, the impact of surface texture for droplet mobility, and the multiscale surface texture for enhancing droplet mobility was demonstrated [39]. To date, several studies [2, 4, 5, 7, 10-12, 14,15,17,19, 24, 26, 33, 36, 37] have been carried out in pure vapor condition and in absence of pure atmosphere. Non-condensable gases in the humid chamber provide an additional component of heat and mass transfer resistance to droplet growth [40, 41]. During condensation and evaporation applications, the detrimental effect of atmospheric sulfur based volatile compounds and aerosols on coating longevity has been revealed in the presence of non-condensable gases [42].

In real applications, frost is initiated by the formation of condensate droplet from the air-vapor mixture where non-condensable gases (compounds in the air) have found [43]. Hence, the present work motivates to run the test in the presence of non-condensable gases, which is more practical.

At higher vapor pressure, better image quality can be obtained from optical microscopy test [22]. Additionally, this test has the benefits to validate the droplet growth data concerning numerical modeling. The test can include the presence of non-condensable content of the saturated vapor [32]. Hence, in present work, all the condensation and frosting experiments have been done via optical microscopy instead of doing it in ESEM.

1.2 Condensate frosting

Frost is often undesirable as it has detrimental consequences for power lines, crops, aircraft, wind turbines, and heating, ventilation, and air conditioning (HVAC) systems [44]. Moreover, the frost accumulation on HVAC components increases the pumping cost resulting in losses of billions of dollars. The passive approach of ice removal is often desirable as deicing is still expensive. Superhydrophobic surfaces have the potential to prevent ice buildup down to a surface temperature -25 to -30 °C, for individual deposited or impacting droplets [45]. However, the typical working conditions encountered in industrial HVAC applications are better represented by condensate frosting [46]. Condensate frost is formed when a surface is cooled below the dew and freezing point temperature. To date, passive anti-frosting surfaces with good durability are still in demand [47]. Condensation and frost growth on the surface has been controlled via effective chemical micropatterns. The ice bridge formation can be passively suppressed by controlling the nucleation sites and the onset of the freezing events [43].

Introducing early freezing events by spatial control of freezing, can maximize the dry zones and reduces the chance of subsequent ice bride formation [43].

The importance of coalescence behavior in delaying frost formation has been observed for the biphilic patterns (surfaces which combine hydrophilic and hydrophobic regions). The surface shown in Figure 1.3 decreased the temperature required for freezing by 6K due to the alteration of the size distribution of the condensed droplet during the freezing process [44].

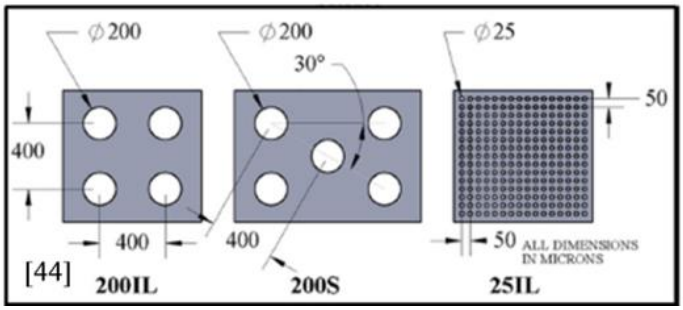

Figure 1.3 Schematic of biphilic surfaces tested [44].

Frost nucleation on flat surfaces has been investigated. It embodies the effect of surrounding air temperature and humidity, and the surface conditions (temperature, roughness, and contact angle) on the frost formation process [48]. Delay of frost growth was observed for the super-hydrophobic isotactic polypropylene surface. Delay is due to the oscillation of the wettability induced by the micro and nanometer structures that can lead to the effective design of anti-frost materials [49]. The increased adhesion of frost on the superhydrophobic surface compared to plain surface imposes the limitations of its use for both on-ground and in-flight applications. The test has been conducted via ESEM imaging that reveals frost formation everywhere on the superhydrophobic surface [50]. However, some of the surfaces lose its superhydrophobicity at a low surface temperature [51]. Higher ice adhesion strength was also observed for textured surfaces compared to smooth surfaces [52].

However, creating highly textured surfaces to decrease the ice-contacting area, as well as a smooth surface with low wettability, can be a way to delay the frost formation [53].

Liquid-infused nanostructured surfaces [53] and through the control of surface chemistry and texturing [54], frost can be delayed under low-humid conditions. Although the defect in any sample leads the start of frost front propagation, delay of frost formation has been observed due to the jumping-drop effect of droplets. This effect controls the average size distribution and separation of the droplet [55]. The process of freezing subcooled condensate and frost formation on lubricant-impregnated surfaces has been described where lubricant may migrate from the textured surface to the surface of frozen droplets [58]. Around 62 s of the freezing delay was observed for the deposited droplet on Si substrate with Silver nanocolumns grown by glancing angle deposition method [59]. By implementing different features on the metal surfaces, frost formation, frost growth, and their properties, and defrosting have been studied [60-62]. Spongy and loose frost suggests the formation of less dense frost on the microgrooved brass surface compared to the plain surface [60]. Microgrooved samples with the deepest groove and widest pillar showed lower frost thickness, as well as higher frost density [61].

Decreased roughness can increase the free energy barrier for heterogeneous nucleation, result in significant freezing delay [63]. For the same roughness, surface coating with lower energy material can promote the freezing delay. Conversely, for the same wettability, higher roughness can slow the frost growth [64]. Freezing delay on the metallic aluminum surface has been investigated at different conditions by adding hydrophobic and coral-like superhydrophobic surface [65, 66]. Both analytical, as well as experimental results, have been presented on frost formation for superhydrophobic silicon substrates fabricated with patterned micropillars of small aspect ratio [67]. The causes of frost retardation with hydrophobic or superhydrophobic surface

treatments can be investigated via the observation of microscopic seed behavior [68]. Frost delaying has been observed for CNT-coated steel surfaces, and perfluoro-coated CNT [69]. At the superhydrophobic substrate-water/ice interface, heat conduction through the functional coatings plays a less vital role in the freezing process compared to the heat conduction through the bulk water/ice layer [70]. Also, superhydrophobic coatings by spray-coating silica paint have been investigated for micro-scale dew formation. The continuous and spontaneous jumping behaviors of the droplets was seen due to the presences of abundant nano-pores from random multilayer stacking of nano-chains shown in Figure 1.4 [71]. The inter-droplet freezing wave propagation is studied on micropillar patterned superhydrophobic silicon surfaces for varying pitch size of the pillars. However, by selecting proper pitch sizes, freezing delay can be achieved [72].

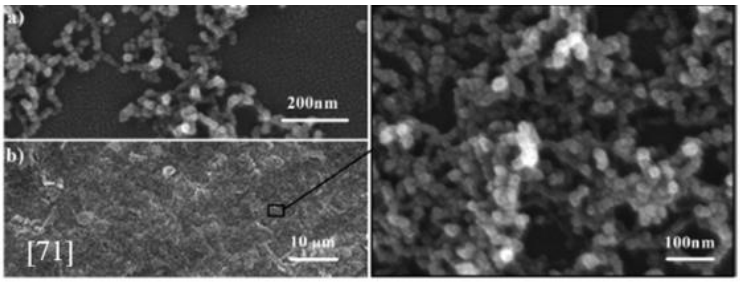

Figure 1.4 Schematic of sprayable superhydrophobic nano-chains coating [71].

To date, the important effect of relative humidity on ice bridging is still lacking in the literature [73]. Additionally, a protective and durable coating is expected for long term applications that would not degrade the wetting properties extensively over the period. For hydrophobic coating, the kinetics and characteristics of ice bridges [43] have not explicitly discussed. Moreover, the effect of wetting properties of graphene on freezing phenomena is still missing. Hence, the present work focuses on running tests in order to address the following issues.

1.3 Acceleration of freezing

Active techniques have been used by the researchers to make the freezing process faster in food processing. The available methods are ultrasound assisted freezing, high-pressure freezing, pressure shift freezing, and air-blast freezing etc. [74-79]. Also, nanopillars create favorable conditions for the formation of amorphous ice, microcrystalline, or cubic crystals. It also creates transparent and cubic ice growth [80]. Nanopillared surface suppresses the coalescence events due to pinning of droplets with discontinuous three-phase contact line at the edges of pillars resulting in irregular shaped droplet [80]. Hence, the surface has the potential to accelerate the freezing due to higher occurrence of coalescence events that delays the frost formation [44]. It would also be expected to reduce the daily power consumption for applications such as food processing, agriculture, and freezing based desalination.

1.4 Condensate harvesting

All over the world, research is going on to mitigate the need of pure water for the increasing global population. About 97.5% of the world's water is seawater, while 2.5% of the water is freshwater. People usually do not like to purify the sea water to satisfy the need as the desalination process is primarily cost and labor intensive. Additionally, the desalination process creates a concentrated brine solution that needs to be wisely managed to keep balance in the ecosystem as it is a health hazard. Moreover, surface engineering has been introduced to enhance the water collection over the surfaces. There is currently significant research on improving fog harvesting and water collection. For example, mesh screens have been employed to recover water from fog in dry environments and from steam evaporate in power plant cooling towers. However, the process is inefficient, and much of the water in these applications remains unrecovered. Therefore, there is a need for ways to increase water recovery.

In present work, nanopillared surface and Graphene Oxide (GO) coated copper surface has been characterized for the condensate harvesting.

1.5 Effect of RH on heterogeneous nucleation

The mechanism of ice bridging is dominating the condensation frosting phenomena on hydrophobic and mildly hydrophilic surfaces. The bridging happens in between the frozen droplet and the neighboring condensed liquid droplet [47]. Hence, before studying the condensate frost formation, detailed condensation dynamics need to be known to get a better understanding of droplet shape and size distribution. For heterogeneous nucleation of droplets [37, 81] in Figure 1.5(a), Gibbs free energy can be expressed as-

$$\Delta G_{heterogeneous} = \Delta G_{homogeneous} \times s(\theta) \qquad \text{Eq. 1.1}$$

$$\Delta G_{heterogeneous} = [-\frac{4}{3}\pi\rho_d R_m T\ln(\frac{P}{P_S})R^3 + 4\pi\gamma R^2] \times s(\theta)$$

$$X = -\frac{4}{3}\pi\rho_d R_m T\ln(\frac{P}{P_S})$$

$$Y = 4\pi\gamma$$

$$\Delta G_{heterogeneous} = [XR^3(a) + YR^2(b)] \times s(\theta) \qquad \text{Eq. 1.2}$$

According to Eq. 1.1, the heterogeneous nucleation energy barrier is less than the homogeneous nucleation energy barrier. For a surface whose wettability is known, Gibbs free energy determines the energy requirement for the nuclei formation. The bulk energy term (a) of Eq. 1.2 can be increased by nearly 80% for changing the relative humidity (RH) to 40% from 60% for nucleating a similar sized droplet under the same operating condition. Hence, less energy is required to form a nucleus at relatively higher humidity. Through useful coatings, the term of Eq. 1.2 can be altered to change the nucleation energy barrier, as shown in Figure 1.5(b).

Hence, desired nucleation rates can be obtained by the manipulation of both ambient condition and surface wettability.

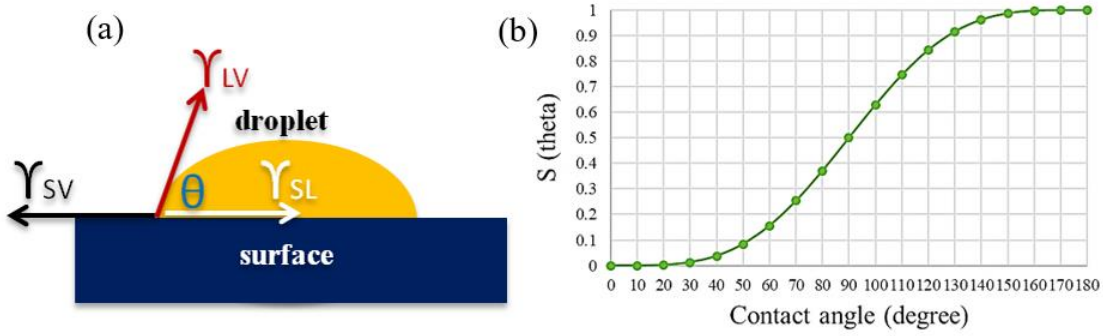

Figure 1.5 (a) Schematic of surface tension components for the heterogeneous nucleation of a droplet on a surface and (b) variation of S (theta) with contact angle

1.6 Objectives

In the past, much effort was given to enhance the performance of dropwise condensation heat transfer and frost delay. Many methods have been proven to be able to increase the heat transfer coefficient (HTC) and freezing time, as shown in Figure 1.6. However, most of these studies were conducted at a particular RH and temperature. Moreover, the effect of change of relative humidity (RH) is considered in only 23% of our reviewed literature; even though the majority of applications are subjected to varying ambient conditions. Also, the durability of the engineered surface was tested in a few of the reviewed studies. Hence, the main focus of the present research is to investigate the droplet dynamics in condensation and freezing phenomena on engineered surfaces. The objectives are-

- To study the effect of surface condition (structure, wettability, or both) on droplet dynamics accompanied with the durability check of the surface as well as repeatability of the test
- The effect of environmental conditions (temperature and relative humidity) on droplet dynamics in the presence of non-condensable gases

- By the integration of surface and environmental effects; fundamental understanding of coalescence events and pinning behavior in droplet growth as well as freezing front propagation on different engineered surfaces
- The results are explored for condensate harvesting, acceleration of freezing and frost delaying

The main aspects of present work have been illustrated in Figure 1.6.

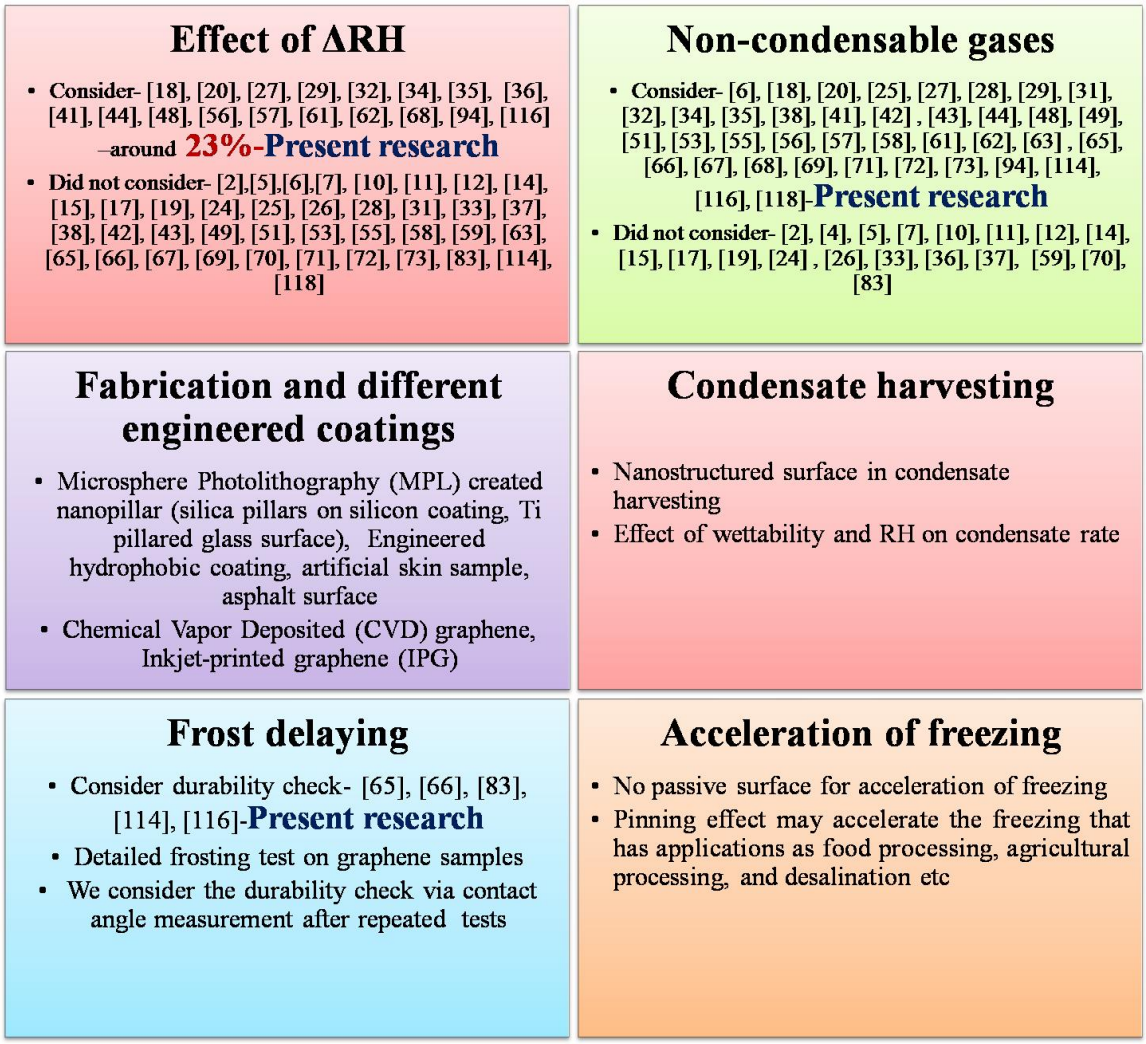

Figure 1.6 Main aspects of the present work were tabulated.

Chapter 2 - Experimental setup

2.1 Test setup

The experimental setup for condensation and freezing tests is shown in Figure 2.1 [82]. The controlled relative humidity and temperature of the chamber (the chamber is situated at the Institute for Environmental Research, Kansas State University) were independently verified using an Omega RHXL3SD thermometer/hygrometer with a rated uncertainty of ± 3% RH. Steam injection valves and desiccant dehumidifier were used to control the humidity inside the chamber. The temperature of room air was controlled through a chiller (glycol mixed water solution) and a resistance heater. Moreover, the room temperature was also monitored by a FLUKE 1523 reference thermometer with a rated accuracy of 0.004% and a resolution of 0.0001°C. The dew point temperature of the room was also monitored by an HYGRO M4-Dew point indicator (General Eastern) with a specification of ± 0.2°C, to ensure the room humidity. Mainly two different room conditions have been established for most of the test cases such as- Condition 1: 40% RH, 295 K and Condition 2: 60% RH, 295 K. Relative humidity of the room was also monitored through the combination of room temperature and dew point temperature measurements. Relative humidity was estimated by using the Psychometric chart. Maximum 1%-2% deviation in RH measurement was observed from the desired conditions. Around 1%-2% variations were also observed during Omega RHXL3SD hygrometer measurement. Moreover, the computer controlled chamber was under quiescent flow (maximum 1-2 m/s) conditions for the convenient operation. After the engineered surfaces are made, they were placed on a Peltier device and bonded with a small amount of high thermal conductivity paste (OMEGATHERM "201"). The Peltier cooler was connected to a TE Technologies TC-720 temperature controller which reads the temperature of the surface by using an MP-3176 thermistor pasted on the Peltier

cooler. A 12 V power source fed the temperature controller. An additional thin film Omega thermocouple was placed under the surface to make sure that the temperature controller was working correctly. The thermocouple was calibrated with an uncertainty of ± 0.5 K. Around ±0.1-0.2 K temperature fluctuations was observed during measurement. The thermocouple was connected to a National Instruments data acquisition system (DAQ-9174 with NI 9211 module). For most of the cases, the cooler was cooled down to 278 K for the condensation test which was 9 K (60% RH) and 3 K (40% RH) below the dew point temperature for the considered environmental conditions. Initially, the surface was kept to 3-5 degrees above the dew point temperature to avoid any unwanted nucleation, and later the surface was brought to desired temperature (Table 2.1) by hitting the button on the temperature controller. For freezing tests, a dust cleaner was used to remove the unwanted droplets on surfaces that reach the steady state set temperature, as well as the video recording button was pushed simultaneously for the data collection. The setup consists of a microscope, the base of the module, and the heat sink was pasted to Peltier cooler, as shown in Figure 2.1.

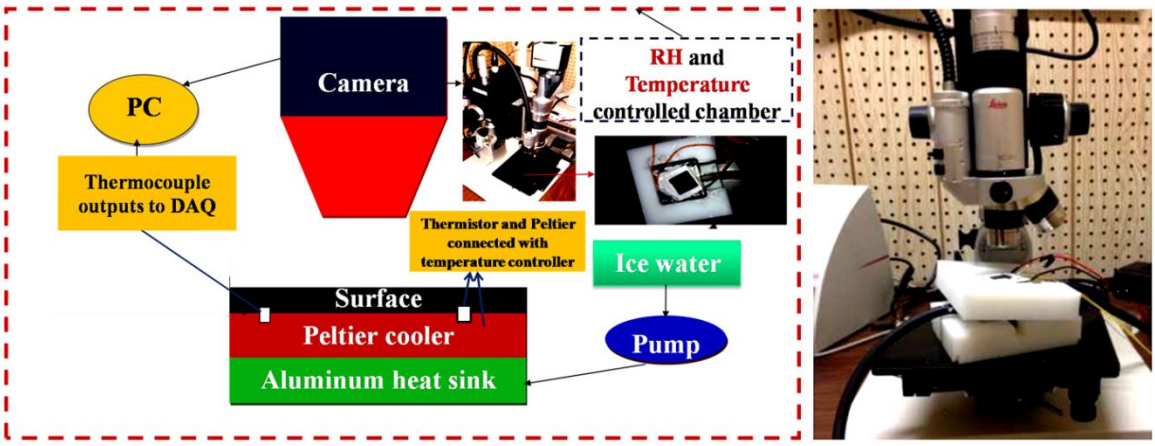

Figure 2.1 Schematic diagram of the experimental setup was shown within the chamber. The sample was horizontally mounted [82].

The base of the test module was polyethylene, and the heatsink was aluminum, comprised of solid bottom half, and finned top half. Half of the heat sink sat inside the polyethylene for insulation. The heat sink was cooled continuously by circulating ice-mixed water via a pump (Fisher Scientific FH100D peristaltic). All the images and videos were captured *in-situ* using a Leica DVM2500 microscope at a rate of 25 frames/second or 100 frames/second focusing near to the center of the sample under different magnifications mentioned in Table 2.1. Repeated measurements were conducted for each combination of surface and relative humidity. Image analysis was performed using the software embedded in the Leica microscope.

2.2 Uncertainty analysis

The maximum uncertainty for the single droplet diameter and single ice bridging length measurement was ± 0.5 μm. The conservative approximation of maximum uncertainty for the count of droplet number was ± 5-10, area coverage was ± 2-5 %, and freezing time was ± 2-4 s. For the post-processing of the results, all the average values (diameter, contact angle, and freezing time) were plotted with the standard deviation, and the other parameters were plotted with uncertainties. If function *f* is dependent on variables $x, y, ..., z$ where the measured quantities have uncertainties $\Delta x, \Delta y, ..., \Delta z$, the uncertainty of *f* is determined as a function of the first partial derivatives of f to its components by Eq. 2.1 similar to the literature [83].

$$f = f(x, y, ..., z)$$

$$df = \sqrt{\left(\frac{\partial f}{\partial x}\Delta x\right)^2 + \left(\frac{\partial f}{\partial y}\Delta y\right)^2 + ... + \left(\frac{\partial f}{\partial z}\Delta z\right)^2} \qquad \text{Eq. 2.1}$$

The uncertainty propagation for the dependent variables such as bridging parameter (*S*), the ratio of frozen to cooled droplet diameter (d_i/d_l), ice bridge velocity has been calculated from the

generalized error propagation Eq. 2.1. The specific experimental condition for each of the surfaces is mentioned below in Table 2.1.

Table 2.1 Different experimental conditions.

Cases	**Environmental temperature (K)**	**RH (%)**	**Surface temperature ['C'-Condensation, 'F'-Frosting], T (K)**	**Magnification**
Silica nanopillar on silicon coated glass surface	295 K	40% or 60%	278 K (C), 265 K (F)	2500×, 600×
Ti nanopillared glass surface and Teflon© coated glass surface	295 K	30 ± 5% to 60 ± 5%	274 K-278 K (C) 265 K (F)	350×
Graphene Oxide (GO) coated copper surface	295 K	40% or 60%	278 K (C)	2500×
Chemical Vapor Deposited (CVD) graphene and Ink-Jet Printed Graphene (IPG)	295 K	40% or 60%	278 K (C), 267 K-271 K (F)	350×
Plain aluminum (Al) and Teflon© coated hydrophobic aluminum (Al-H)	295 K	40% or 60%	265 K (F)	350×

Chapter 3 - Condensation on nanopillared surfaces

3.1 Sample characteristics

Nanosphere Lithography [84] or Microsphere Photolithography [MPL] [85-88] techniques are available for patterning a surface. MPL was used to pattern the silica nanopillars on silicon coated glass surface [82], as shown in Figure 3.1.

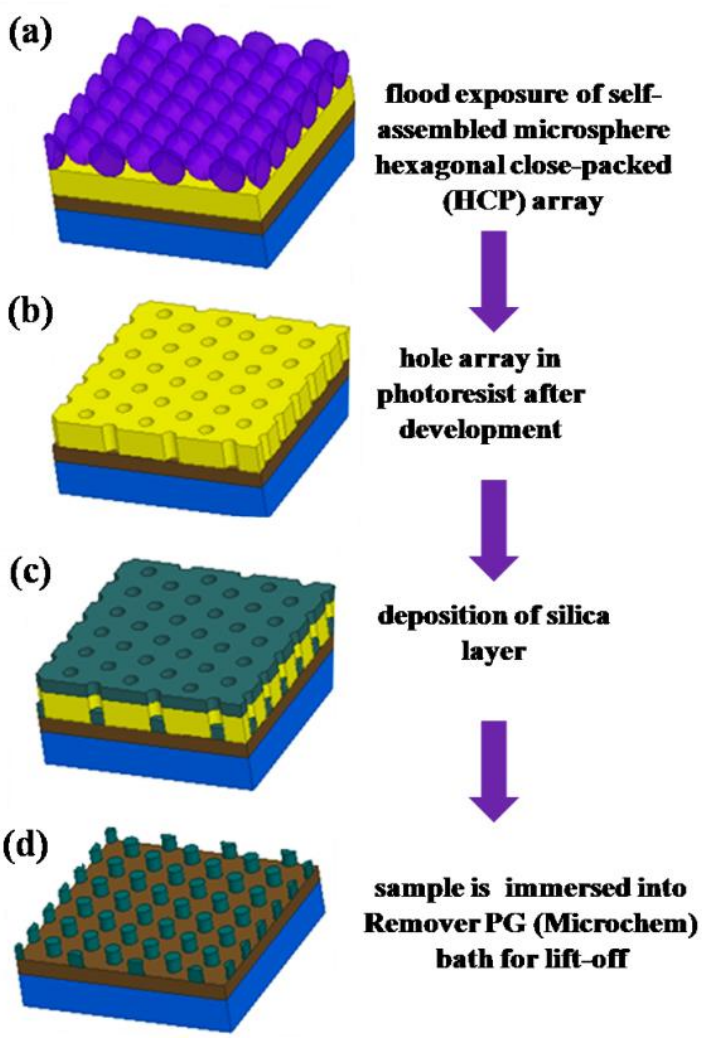

Figure 3.1 Microsphere Photolithography process showing the detailed and sequential fabrication process of silica nanopillar (dark green) on the silicon coating (brown). The yellow color is for 'Photoresist' [82].

3.2 Wetting state of a water droplet on nanopillared surface

Apparent contact angle measurements of injected water droplets on nanopillared and silicon surfaces have been conducted. Recently, theoretical contact angle model for injected water droplets on rough surfaces have been provided in Suzuki *et al.* [89]. They considered the pinning effect at the edge of a pillar. The model represents the apparent contact angle as a function of pillar pitch, pillar width, pillar height, and the forces acting at all interfaces of the droplet. However, this model has been modified for the present study considering the effect of surface material and geometry. The interfacial force balance to determine the apparent contact angle (θ') is shown in Figure 3.2.

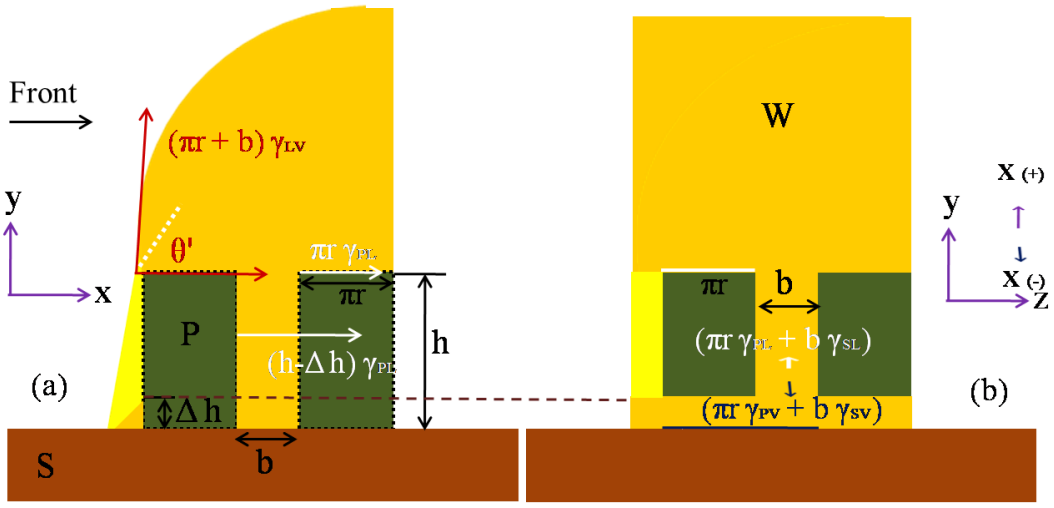

Figure 3.2 The figure shows an equilibrium of interfacial tensions at a pinned three-phase contact line of an injected droplet on a circular pillar-patterned surface (a) side view of a droplet sitting on pillars (b) front view of the wetting state of the droplet [82].

The view-plane has been shown separately for each of the diagrams. In figure (b), the blue arrow represents the negative X-direction which is perpendicular to the paper (S = silicon; P = silica pillar; and W = water droplet). The apparent contact angle is presented by θ'. Figures are not to scale.

The droplet is pinned at the edge of the pillar. The liquid droplet goes through the gap between the pillars (Wenzel wetting state). The color ( ) represents the droplet probable curvature shape without pinning from the edge of the pillar. The equilibrium equation for the components of the interfacial tension (liquid-vapor tension: red color, solid-liquid tension: white color, and solid-vapor tension: blue color) in the horizontal direction is presented below where 'Δh' is a height of the liquid that goes around the bottom of the pillar (a). When 'Δh' is much smaller than 'h' and neglecting Δh, the balance of interfacial tension along the positive X-axis can be written as:-

$$(\pi r + b)\gamma_{LV}\cos\theta' + (\pi r\gamma_{PL} + b\gamma_{SL}) + \pi r\gamma_{PL} + 2(h - \Delta h)\gamma_{PL} - (\pi r\gamma_{PV} + b\gamma_{SV}) = 0$$

$$\Rightarrow \cos\theta' = \frac{(\pi r\gamma_{PV} + b\gamma_{SV}) - 2(\pi r + h)\gamma_{PL} - b\gamma_{SL}}{(\pi r + b)\gamma_{LV}} \quad \text{Eq. 3.1}$$

$$\cos\theta_{0P/0S} = \frac{\gamma_{PV/SV} - \gamma_{PL/SL}}{\gamma_{LV}} \quad \text{Eq. 3.2}$$

$$\cos\theta_1 = -\frac{\gamma_{PL}}{\gamma_{LV}} \quad \text{Eq. 3.3}$$

The measured apparent contact angle is consistent with the theoretical apparent contact angle derived from Eq. 3.1. The surface tension of water (γ_{LV}) is ~72.8 mN/m, silicon (γ_{SV}) is ~61.22 mN/m, and silica (γ_{PV}) is ~57.71 mN/m [90]. Contact angles are extremely sensitive to contamination as well as it can be increased by the presence of an oxide layer or contaminants on the solid surface. The Young's angle of silicon (θ_{0S}) and silica (θ_{0P}) was found to be 38 ± 4^{o} and 60 ± 2^{o} [91] from measurements. Using Eq. 3.2, the interfacial tension forces for the pillar (γ_{PL}) and substrate (γ_{SL}) were calculated. The pinning angle (θ_1) was found from Eq. 3.3. Finally, Eq. 3.1 has been introduced to evaluate the theoretical apparent contact angle considering the penetration of water droplets into the grooves between the pillars, which is Wenzel wetting state.

For the fabricated nanopillar geometry, the designed parameters were- pillar radius, r=0.35 µm, and height, h=0.3 µm. The apparent contact angle was measured by placing a single droplet on the pillared surface, as shown in Figure 3.3. Moreover, the measured values of the apparent contact angle of a water droplet on the pillared surface (83 ± 1.99º) showed well agreement with the derived values (~77º) from Eq. 3.1 and the maximum deviation was observed to be ~7%-8%. Although the wetting state of the injected droplet on the pillared surface was found to be Wenzel wetting state, could not be easily described by the classical Wenzel equation [92], but showing good agreement with the approach [89] based on the balance of horizontal equilibrium interfacial tension forces of a droplet positioned on rough pillared surface.

Figure 3.3 Apparent average contact angle measurement for the injected water droplet on (a) nanopillar surface (b) silicon surface [82].

3.3 Droplet growth mechanism on a nanopillared surface

The time-lapsed growth of condensed droplets for both silicon and nanopillared surfaces at 40% RH and 60% RH has been reported in Figure 3.4. Regular spherical-shaped droplets were observed for the bare silicon surfaces at 40% RH and 60% RH. However, the droplet dynamics changed significantly for the nanopillar surfaces due to the unique pinning effect.

On nanopillar surface, droplets were observed to be span along the pillars, as shown in Figure 3.4(a) and Figure 3.5. Once droplets span multiple pillars with the elapsed of time, they grew by stretching, due to the pinning caused by the pillars. Hence, non-spherical and asymmetrical droplets were observed on the nanopillared surface. The droplets are perceived to be in coalescence only when they touch each other. The droplet pinning on the surface did not prevent droplet growth or merging since droplets continue to grow due to direct condensation at the vapor-liquid interface. At 60% RH, the diameter of the condensed droplets was found larger than 40% RH as shown in Figure 3.4, due to higher occurrences of coalescence events and the increased mass of water vapor accumulation from the humid air into the vapor-liquid interface of the droplets. Higher coalescence rate was also found for the silicon surface. For both surfaces, at t = 120 s, lower droplet density and higher surface coverage were observed for 60% RH compared to 40% RH as shown in Figure 3.4. Although the lower direct growth rate was found for the droplets condensed on the nanopillar surface for a particular humidity, the pinning effect enhanced the number of stable droplets on this surface compared to plain silicon surface over a time-lapsed. The higher droplet density over a specific period signifies the importance of this fabricated nanopillar surface in long-term condensate harvesting [93].

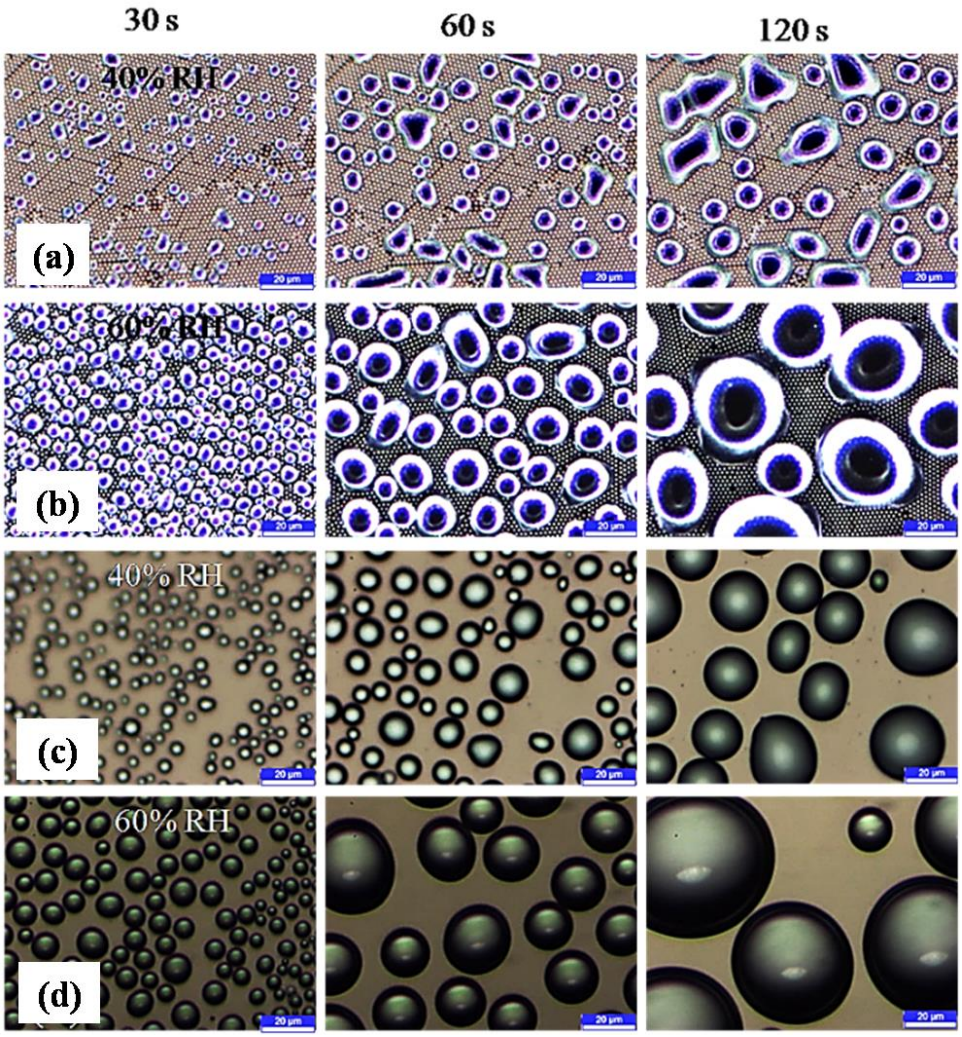

Figure 3.4 Early stage of condensation images for first 30 s, 60 s and 120 s (a) nanopillar-40% RH (b) nanopillar-60% RH (c) silicon-40% RH (d) silicon-60% RH [82].

3.4 Pinning mechanism and wetting state of the condensed droplet

From Eq. 1.1, relative humidity can manipulate the nucleation energy barrier as well as nucleation site density significantly. Hence, the condensation test was conducted under different environmental conditions [37, 94]. The pinned and irregular droplets were observed. The bottom of the condensed water droplet was not circular, and a three-phase contact line ended along the edge of the pillar. The directional anisotropy was also observed. It ensures the condensed droplets' wetting state as Wenzel consistent to literature [16, 35].

A theoretical model of the apparent contact angle has been formulated for the condensed droplet based on the energetic state. To prevent coalescence, the energy required to overcome the capillary pressure ($E_{capillary}$) must be higher than the surface energy reduction (E_s) by coalescing of droplets mentioned in Eq. 3.4 -

$$E_{capillary} \geq E_S \qquad \text{Eq. 3.4}$$

The capillary energy was calculated from work done by the volume of the water at the liquid-solid interface. It depends on capillary pressure ($P_{capillary} \approx 2\gamma_{LV} \cos\theta^{'}/r$) working at the interface multiplied by the volume of water (V), the base contact area of a droplet (A), and the pillar density (α). The pillar density (α) was assumed to be the function of pillar radius and can be calculated as $\alpha = 2/9\sqrt{3}r^2$ for a unit cell depicted in Figure 3.5 (b).

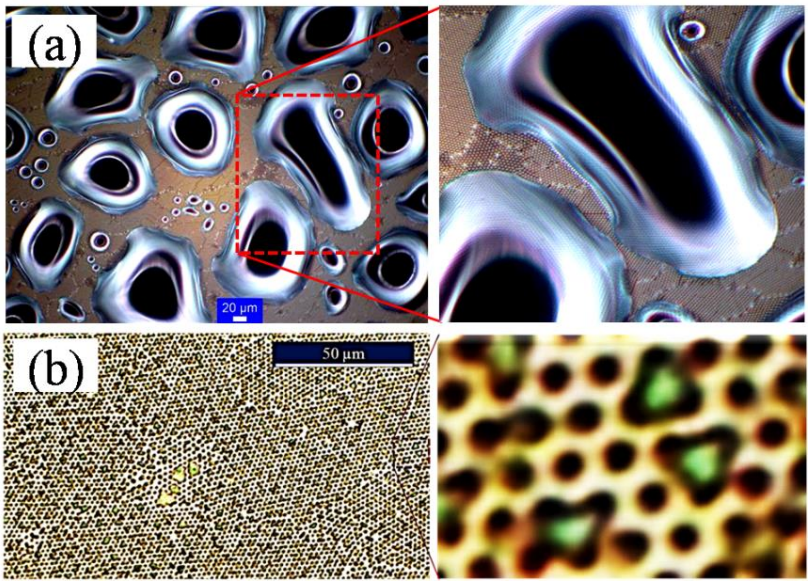

Figure 3.5 Wenzel wetting state was observed with irregular and pinned droplets. Contact line pinning of the droplets is observed in (a), and condensed state of the droplets was zoomed to the unit cell in (b) [82].

So, capillary energy equation can be written as -

$$E_{capillary} = P_{capillary} \times V \times \alpha \times A \qquad \text{Eq. 3.5}$$

$$S = R \times (1 - \cos\theta') \qquad \text{Eq. 3.6}$$

$$r_b = R \times \sin\theta'$$

$$V_s = \frac{\pi R^3}{3}(2 + \cos\theta')(1 - \cos\theta')^2$$

$$E_S = \frac{2\pi R^2 \times \gamma_{LV} \times \sin^2\theta' \times (2 - 2^{2/3})}{1 + \cos\theta'} \qquad \text{Eq. 3.7}$$

$$2\gamma_{LV} \cos\theta' \times \pi \times r \times h \times \alpha \times A \geq \frac{2\pi R^2 \times \gamma_{LV} \times \sin^2\theta' \times (2 - 2^{2/3})}{1 + \cos\theta'}$$

$$r \leq 1.55 \times h \times \cos\theta' \times (1 + \cos\theta') \qquad \text{Eq. 3.8}$$

By definition, r_b is the base radius of the spherical cap, S is the height of the cap, and V_s is the volume of the cap which all are related to the apparent contact angle mentioned in Eq. 3.6 [95]. The surface area reduction from two coalescing droplets (R_1 and R_2) has been calculated based on the spherical cap assumption, and the radius of the droplets are considered the same (R_1=R_2=R). The reduction in surface energy (E_s) can be written as Eq. 3.7. Hence, the minimum radius of the pillar required to pin the droplets as a function of pillar height (h) and apparent contact angle (θ') has been found from Eq. 3.8.

The fabricated pillar radius was within the limit depicted by Eq. 3.8 and exhibit droplet pinning behavior for a specific range of apparent contact angle based on the pillar height and spacing. The apparent contact angle for the condensed droplet was observed to be ~60º-70º (solid circle) shown in Figure 3.6.

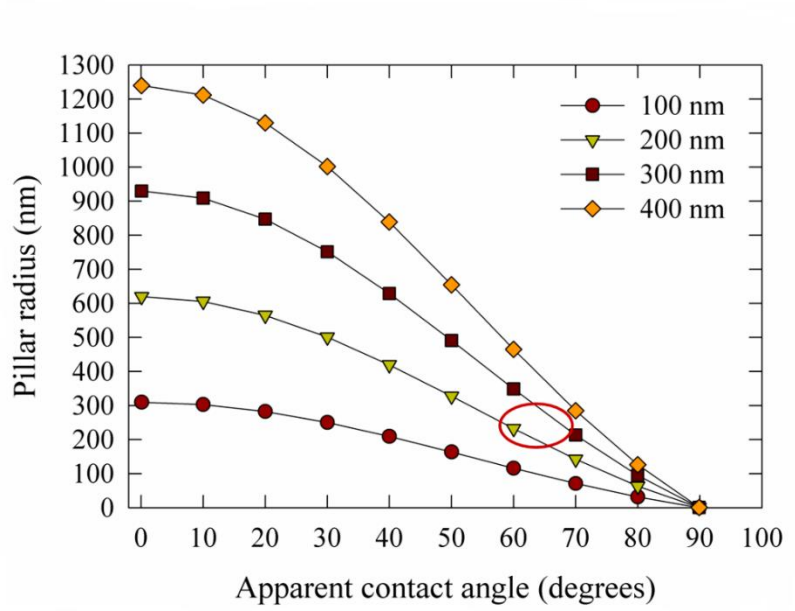

Figure 3.6 The pillar radius required for exhibiting pinning mechanism at varying apparent contact angles and pillar heights [82].

The calculated apparent contact angle and images are shown in Figure 3.5 (a-b) which elucidated the wetting state of the condensed droplet as 'Wenzel state'.

3.5 Mechanism of droplet regeneration

Repeated coalescence and regeneration phenomenon have been observed for the silicon and nanopillared surface. The regeneration of droplet was likely to have occurred at pre-coalesced space (void space) rather than bare spaces with no previous nucleation at 40% RH and 60% RH. From Figure 3.7(c)(e), the nucleated droplets approach nearly equal diameter within a minute at two different time regions (~10 minutes lapse) elucidating almost constant growth rate for the newly generated population. From the time-lapsed images, just before the first regeneration, the coalescence happens and triggers the rejuvenation of droplets to relieve high surface energy. The nanopillared surface impedes coalescence rate, delaying the regeneration (of the droplet at 40% RH and 60% RH mentioned in Figure 3.8.

This behavior of droplet confirms the more extended stability (~duration of stay) of the condensed droplet on nanopillared surface compared to the silicon surface.

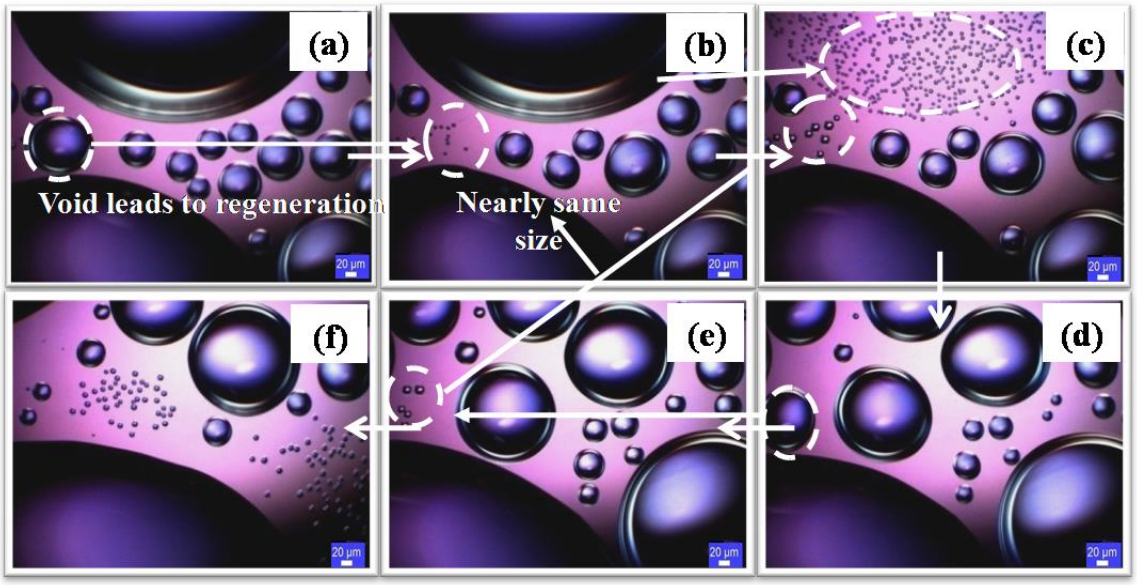

Figure 3.7 Droplet growth images for silicon surfaces at 60% RH (a) 22 min 30 s (b) 23 min (c) 23 min 30 s (d) 32 min (e) 33 min (f) 34 min [82].

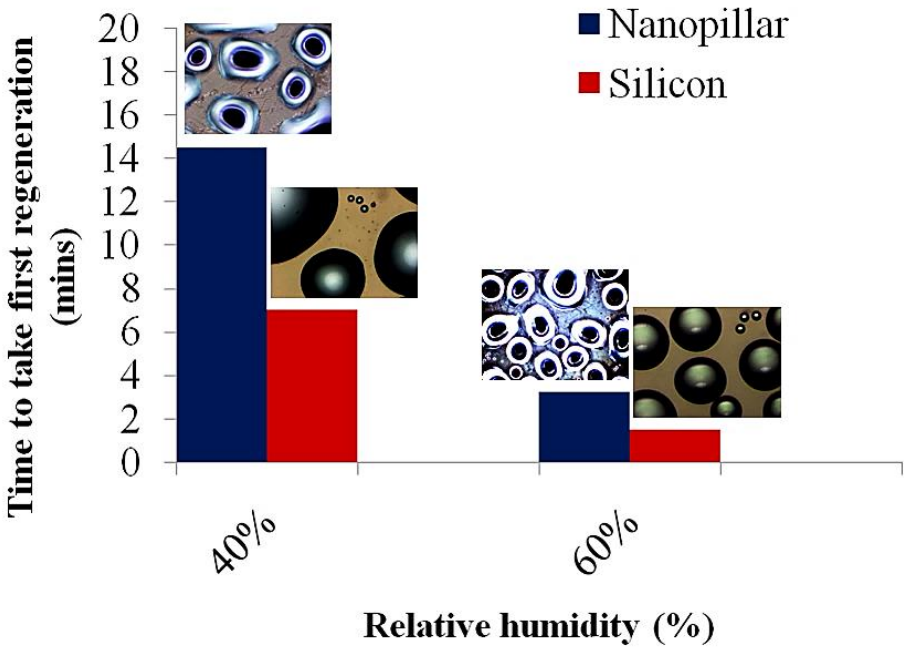

Figure 3.8 Time to reach first regeneration. The regeneration of droplets was seen to be delayed by the patterned surface. The pinning of droplets made the droplet less movable (water stability and more time for condensate collection) [82].

3.6 Effect of relative humidity (RH)

Relative humidity (RH) has the potential to regulate the nucleation energy barrier mentioned in Eq. 1.1. Hence, the humidity not only controls the initial spatial and temporal distribution of the droplets on the condensing surface but also determines the subsequent growth rate of the droplet. Increasing the relative humidity during the condensation test significantly influences the size distribution of the droplets on the nanopillared surface. Altering environmental conditions to 60% RH from 40% RH produces a noticeable increase in droplet size.

The growth of droplets on nanopillar surfaces for first 10 minutes can be well fitted by power-law growth -$d \propto t^{0.56}$ for 40% RH and $d \propto t^{0.68}$ for 60% RH as shown in Figure 3.9(a-b).

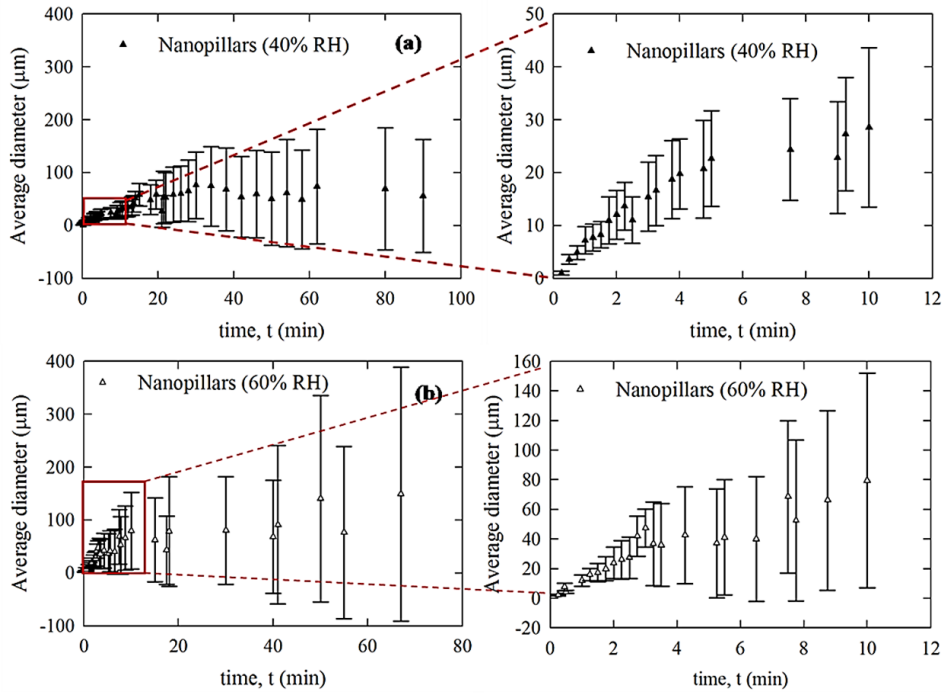

Figure 3.9 Distribution of average diameter for condensed droplets on nanopillared surface at (a) 40% RH (b) 60% RH [82].

The maximum average diameter of the droplet was found ~150 µm for 60% RH. As earlier stated, this more substantial growth can be accompanied by both mass accumulation and coalescence events. The mass transfer across the vapor-liquid interface at a specific relative humidity [22, 34] can be expressed as Eq. 3.9-

$$m'' = \phi(T_{sat} - T_S) \qquad \text{Eq. 3.9}$$

Where T_{sat} is the saturation temperature of the system (varies with RH and room temperature), m'' is the mass transfer rate across the interface, ϕ represents the kinetic mobility, which can be found from Eq. 3.10-

$$\phi = \frac{2\beta}{2-\beta} \frac{h_{fg}}{\sqrt{2\pi R_m T_{sat}}} \frac{1}{(1/\rho_G - 1/\rho_D)T_{sat}} \qquad \text{Eq. 3.10}$$

β is the constant, which ranges from 0.04 to 1 depending on the fluid [22]. In the present experimental condition, β is assumed to be '1' similar to the literature [34]. Considering Eq. 3.9, ~12.5× mass transfer through the vapor-liquid interface was found at 60% RH compared to ~2.8× for 40% RH.

3.7 Effect of different surfaces on droplet growth

The relative significance of the coalescence phenomenon over direct condensation has been studied via the local growth dynamics of the individual droplet. In Figure 3.10, the dominance of small coalescence events on droplet's final diameter was observed for the silicon surface. Interestingly, for the nanopillared surface, the tracked droplets underwent three significant coalescence events during their growth within this period to reach an equivalent diameter of ~65 µm.

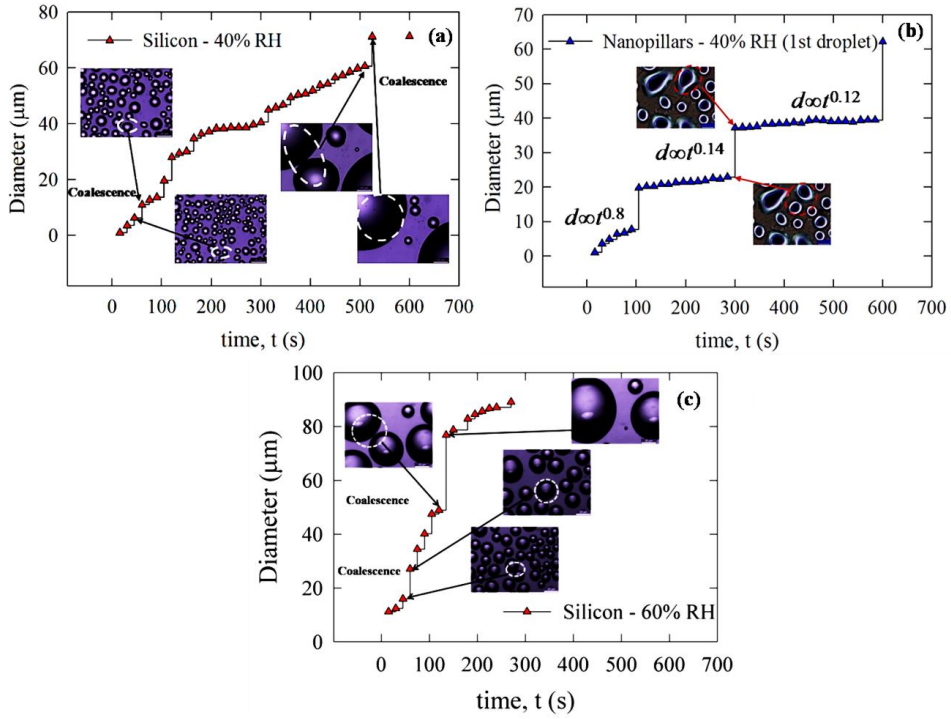

Figure 3.10 Individual droplet growth with time (a) silicon (b) nanopillared surface at 40% RH, and (c) silicon at 60% RH [82].

The rest of the period, direct condensation happened. However, the final diameter of the tracked droplet within the first 600 s was dominated by large coalescence events. The direct growth was subdivided into three phases before facing each of the large coalescence events. During the 1st phase of direct condensation, the droplet diameter increased according to power law growth, $t^{0.80}$. At later stages, growth rate reduces to $t^{0.12}$, indicating lower direct condensation rate for the larger droplets. The reason might be the higher conduction resistance (R_c) of the larger growing droplet [22, 33] given by the Eq. 3.11-

$$R_c = \frac{R\theta'}{4K_w \sin\theta'} \qquad \text{Eq. 3.11}$$

Also observed in Figure 3.10, 40% RH exhibits ~6× time delay to reach an equivalent diameter (~70 μm) of a droplet compared to 60% RH.

The surface coverage is defined as the ratio of accumulated droplet's projected area to the observed view field area. For 50 minutes of condensation test, ~12.87% and ~24.13% increment of surface coverage were observed for nanopillar surface compared to the silicon surface, as shown in Figure 3.11(a).

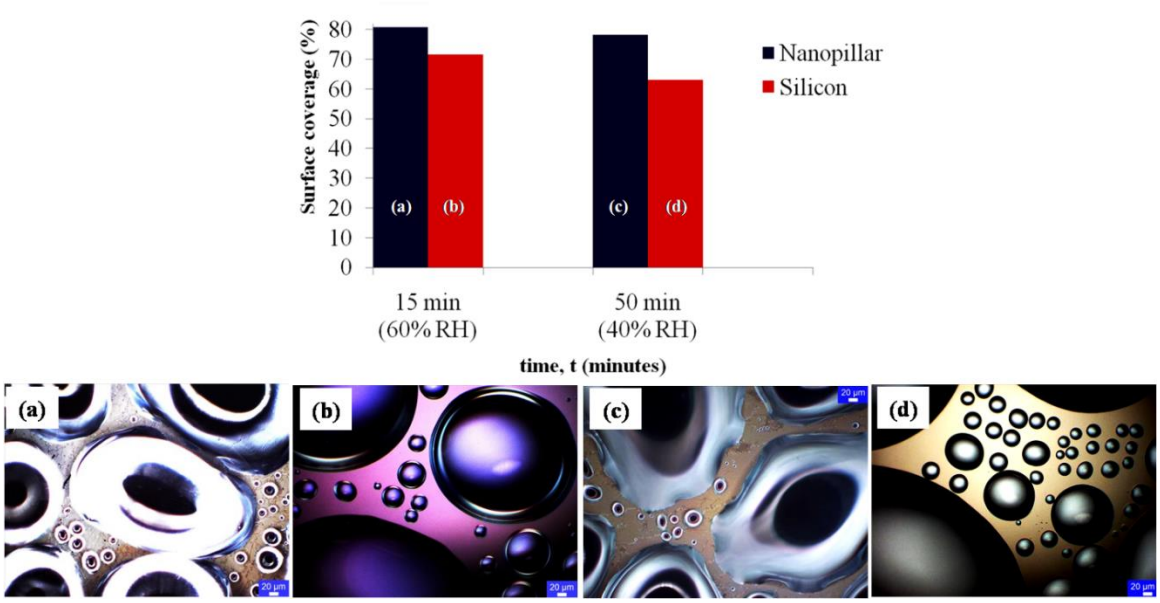

Figure 3.11 Surface coverage was shown for different cases. (a-d) droplet size distribution for the stated cases [82].

For both surfaces, it required ~3× higher time for 40% RH to reach a surface coverage equivalent to 60% RH. Hence, increasing relative humidity accelerated surface coverage. The number of droplets per unit area of observed view field is defined as droplet density. Droplet density was found higher for nanopillared surfaces for a longer duration, from the start of the condensation test. Initial droplet density $10^8/cm^2$ found in this research is well consistent with the literature [4].

3.8 Conclusion

The nanopillar surfaces have a significant impact on condensation behavior. By pinning droplets, coalescence is suppressed for the nanopillar surface and increases the droplet density over a larger area that would yield higher condensate. The pinning state of the condensed droplets enhances the stability of the droplets on the nanopillar surfaces compared to the plain silicon surfaces. The coalescence event is contributing highly to the final diameter of the droplets that emerged on nanopillared surface within the first ten minutes. The work eventually shows that how the nanopillared surface can effectively affect the nucleation energy, nucleation site density, droplet size distribution, and percentage of surface coverage under different ambient conditions.

Chapter 4 - Freezing on nanopillared surface

4.1 Nanopillar characteristics and wetting state of the droplet

This chapter of the study examines the effect of nanopillared surface on the nucleation, growth, and subsequent freezing processes [96]. As discussed in chapter 3, the nanopillared surfaces had a different impact on droplet dynamics, and may also have different freezing behavior.

Experiments were conducted on Microsphere Photolithography (MPL) created silica nanopillar on a silicon coated glass surface, as shown in Figure 4.1(a-b).

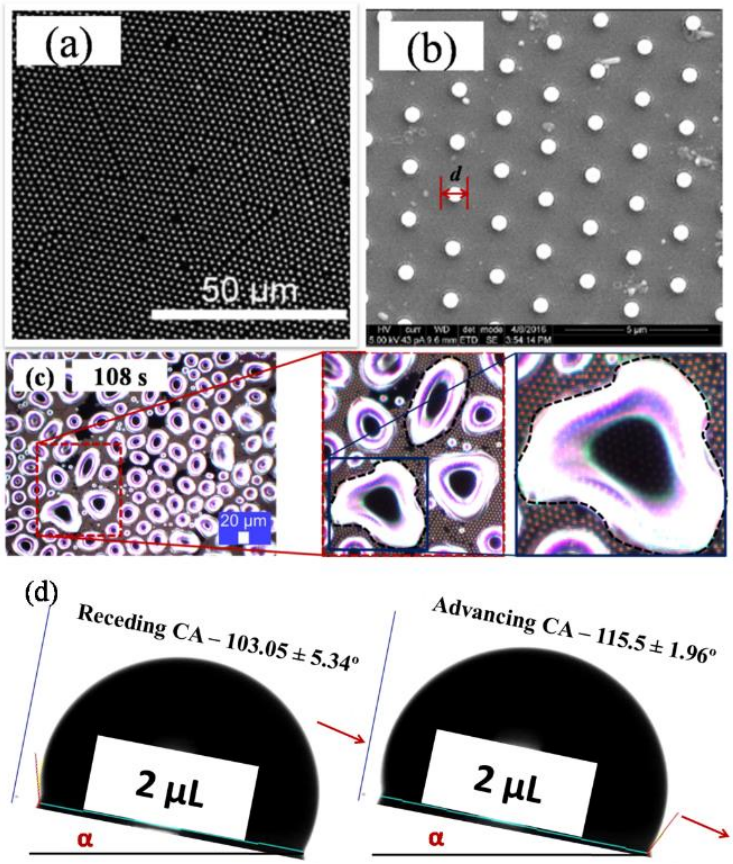

Figure 4.1 (a) Microscopic image (b) SEM image of the finished fabricated surface (c) wetting state of the condensed droplet (d) Advancing and receding contact angle measurement on Teflon© coated silicon surface [96].

The relationship between the ‘onset of freezing’ and the ‘freezing front propagation rate’ was investigated. The propagation rate can also be expressed as the time difference between the ‘onset of freezing’ and the ‘final freezing time’ [43, 67]. The results are compared with a plain silicon (hydrophilic), and Teflon© coated silicon surface (hydrophobic). For an injected droplet, contact angle (CA) on a plain surface, and nanopillar surface can be found from Figure 3.3. CA on Teflon© coated silicon surface was measured by the tilt table method using a goniometer shown in Figure 4.1(d). The droplet volume was taken as 2 µL-3 µL for neglecting the effect of gravity [97]. The CA measurement uncertainty was ±1-2º. The CA shows the different intrinsic wetting properties of the surfaces.

4.2 Initial nucleation site density

Initial nucleation site density has been reported in Figure 4.2 for both surfaces. The pinning mechanism impedes droplet mobility, coalescence, and growth. Hence, the condensed/frozen droplets were in Wenzel wetting state consistent to the literature [16, 35] shown in Figure 4.1(c). Although the initial nucleation site density seems comparable for both surface at t=1 s (Figure 4.2), the droplets appear to be much smaller in size for the nanopillared surface compared to the plain surface when the surfaces finish freezing. When droplets froze on the surfaces, there was very little change in the index of refraction or reflectance.

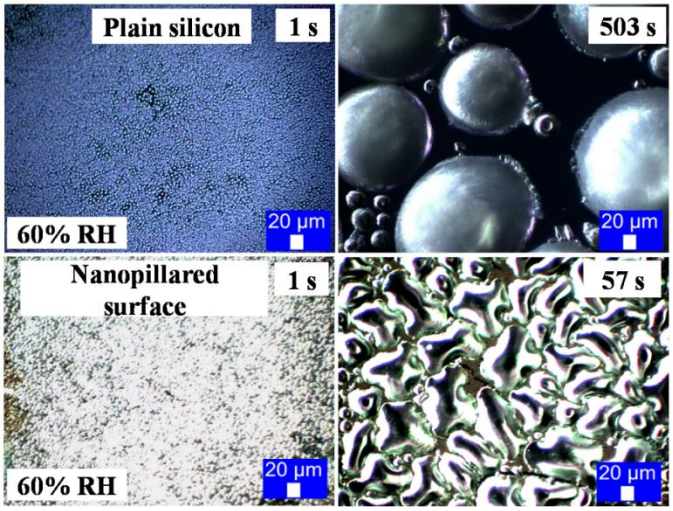

Figure 4.2 The image of nucleation site density (t=1 s) on plain silicon and nano-pillared surfaces. The images are presented until the freezing of all droplets [96].

4.3 Different freezing trials on a nanopillared surface

The droplets on nanopillared surface are consistently irregular in shape and little ice bridges [47] were observed. Ice bridge forms due to different vapor pressure gradient over the frozen and liquid droplets on the same field of view. Frozen droplet has a lower vapor pressure compared to a nearby liquid droplet; hence, frozen droplet harvests water from the liquid droplet. The source-sink interaction between the droplets (frozen and liquid) leads to the formation of interdroplet ice bridging [47]. For the plain silicon surface, larger voids were observed in Figure 4.3(d) between the droplets. The larger void delays the required ice bridging. The freezing tests were also conducted for Teflon© coated silicon surface, as shown in Figure 4.3(e), which shows higher freezing time than the plain silicon and nanopillared surface. Nanopillared surface accelerated freezing compared to both of the control surfaces (silicon and Teflon© coated silicon surface) due to the pinning effect.

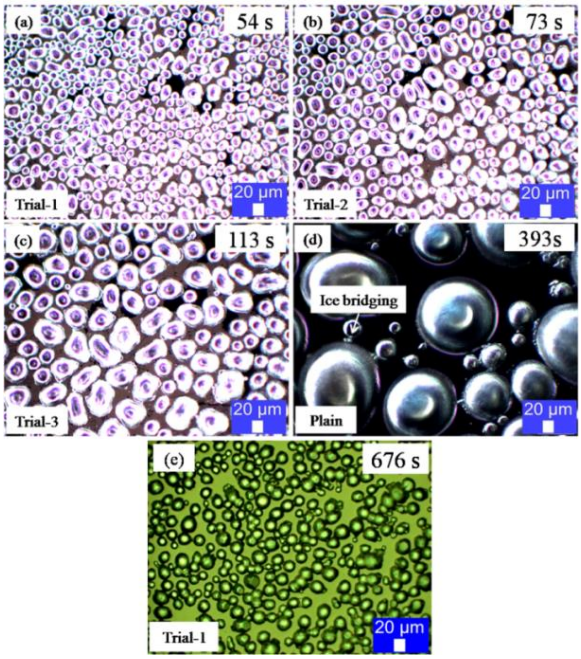

Figure 4.3 nanopillars frozen at (a) 54 s, (b) 73 s, (c) 113 s, (d) plain surface frozen at 393 s (e) Teflon© coated surface frozen at 676 s. (a), (b), (c) are different trials on the same nanopillared surface at 40% RH [96].

4.4 Freezing mechanism on a nanopillared surface

The different coalescence behavior resulted from the pinning of the pillars alters the size distribution of the droplets. Large sized droplets with lower droplet density (number of droplets per unit area) delay the freezing process, as shown in Figure 4.4. The higher the occurrence of coalescence events, the longer the freezing delay, well consistent to the literature [44]. Energy is released due to surface area reduction (coalescence events). Hence, it increases the energy required for the freezing as droplet volume increases [44]. The maximum droplet diameter on plain surfaces has been 2×-2.4× higher than the corresponding droplet diameter observed on nanopillar surface, as shown in Figure 4.4(d).

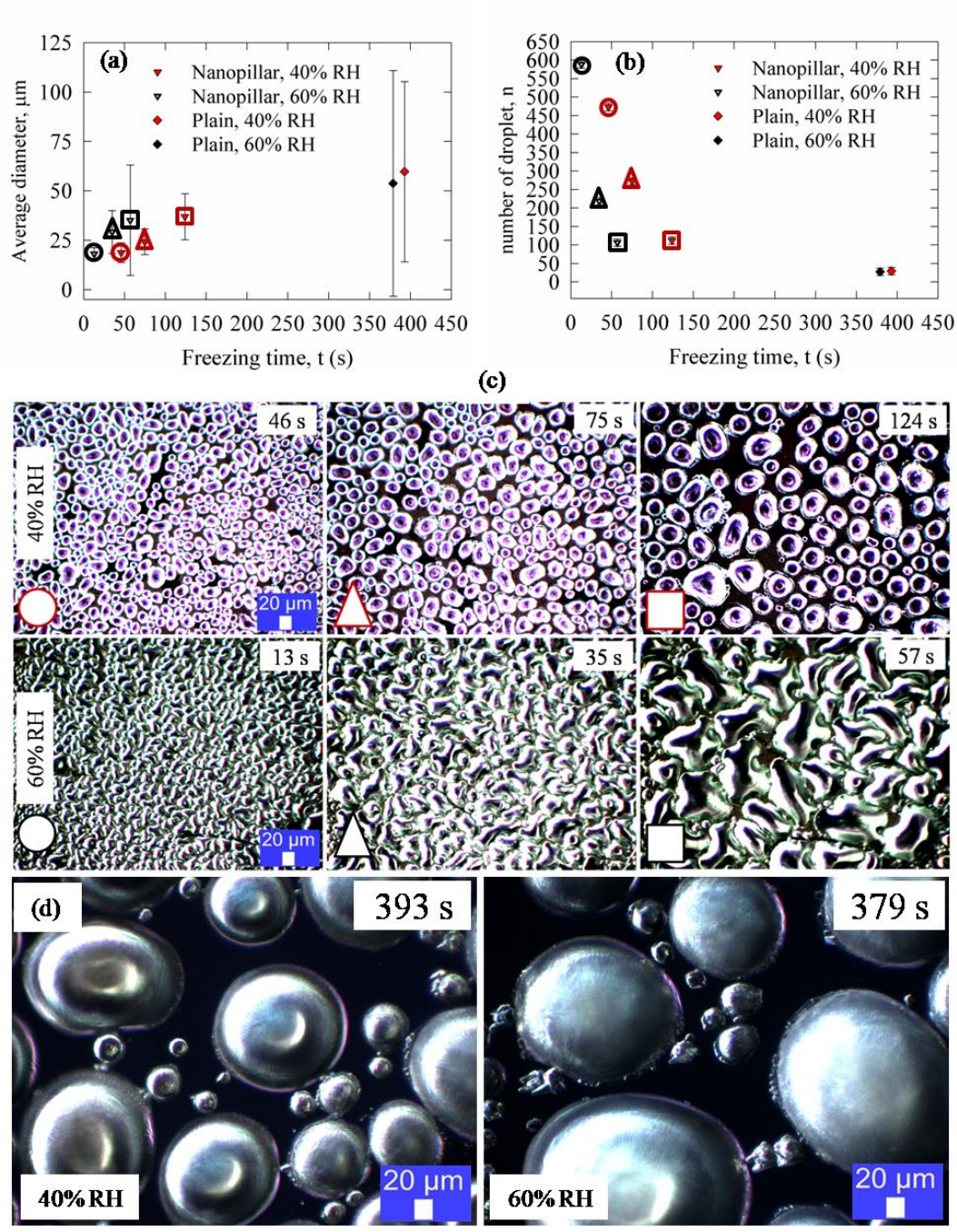

Figure 4.4 Variation of (a) average diameter (b) droplet density, and (c) images for minimum (circular), average (triangular), maximum (rectangular) freezing time at 40% RH and 60% RH (d) droplet size distribution for the plain surface [96].

4.5 Different freezing trials on plain and Teflon© coated surface

The detailed freezing dynamics on Teflon© coated surface was presented in Figure 4.5. The onset of freezing within the observed view field was observed at 585 s. The final freezing time was 676 s with a freezing delta of 91 s.

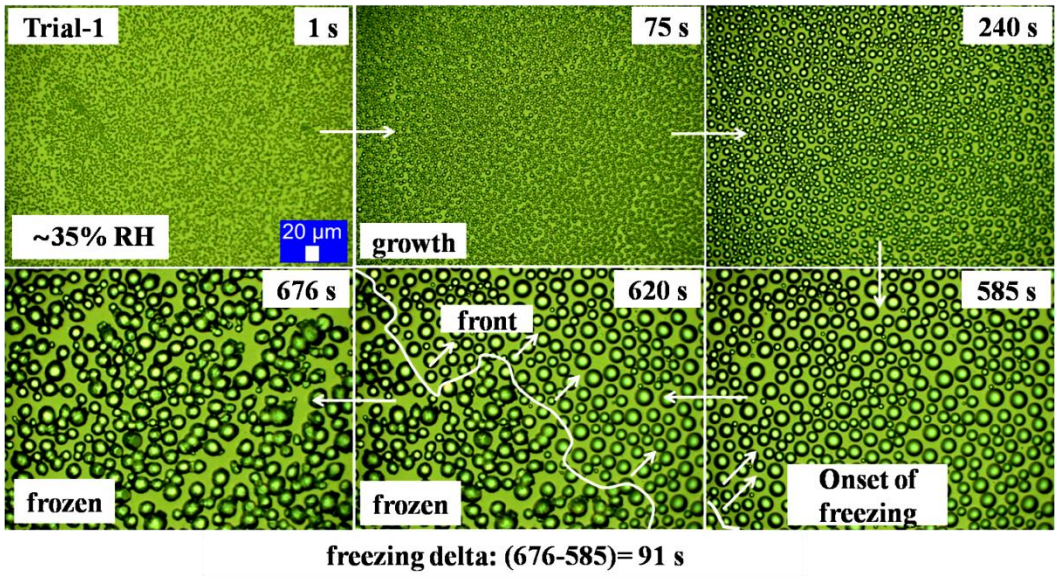

Figure 4.5 Freezing dynamics on the Teflon© coated silicon surface [96].

4.6 Final freezing time

The 'final freezing time', is defined as the moment when all the droplets on the surface under the microscope have frozen. Additionally, the 'onset of freezing' is defined as the time when the first droplet in the view of the microscope freezes. The 'delta freezing time' is the difference between the 'onset of freezing time' and the 'final freezing time'. For silicon and Teflon© coated surface, the average freezing time is reported in Table 4.1.

Table 4.1 Reported freezing times for different cases.

Surface	Freezing time	Standard deviation	Range
40% RH nanopillared	73.6 s	17.3 s	46 s-124 s
40% RH plain silicon	369.5 s		
35% RH Teflon© coated	721.75 s	60.96 s	664 s- 870 s
60% RH nanopillared	34.5 s	11.6 s	13 s-57 s
60% RH plain silicon	414.0 s		
Surface	**Delta freezing time**	**Standard deviation**	**Range**
40% RH nanopillared	11.7 s	3.7 s	7 s-21 s
40% RH plain silicon	36 s		
35% RH Teflon© coated	86.5 s		67 s-94 s
60% RH nanopillared	2.6 s	1.3 s	1 s-8 s
60% RH plain silicon	42.2 s		

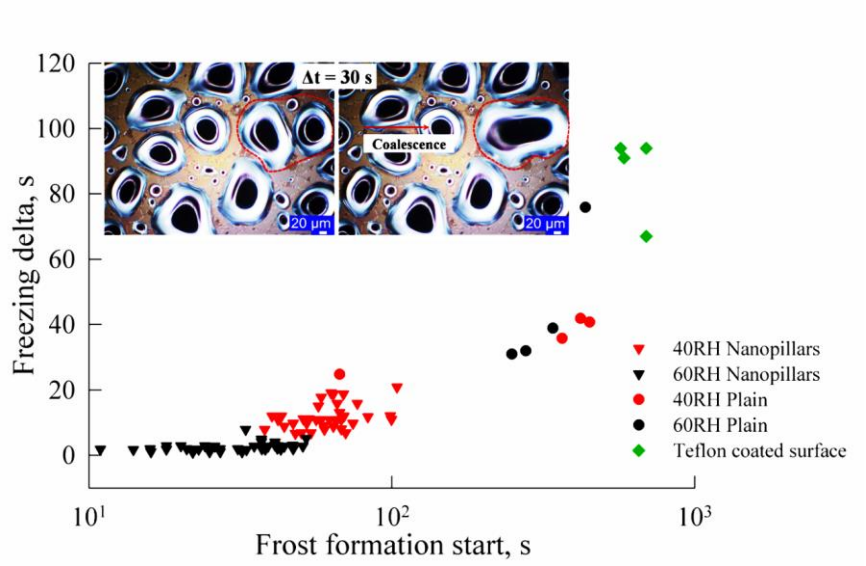

Figure 4.6 Relationship between the start of frost formation and the freezing delta time for both plain and nanopillared surfaces at both 40% RH and 60% RH [96].

The data for Teflon© coated surface at 35 ± 5% RH has also been presented for the comparison. The inset images show the coalescence of droplets on nanopillared surface in 30 seconds at 40% RH. Furthermore, in Figure 4.6, it is also observed that, the beginning freezing time (frost formation start), and freezing delta appears to be proportionately related.

4.7 Conclusion

For the plain surface, the ice bridges need to cover a larger void for the propagation of the freezing front within the growing droplets. By pinning droplets, coalescence is suppressed for the nanopillared surface, altering the size distribution of droplets and accelerated the freezing process. To illustrate, at 60% RH, the average freezing time of a nanopillared surface (34.5 s) is an order of magnitude faster than a plain hydrophilic surface (414.0 s). The larger voids in the plain surface may require a longer time to propagate the freezing front. Hence, this passive acceleration of freezing process has potential to reduce the daily power consumption for applications such as food processing, agriculture, and freezing based desalination.

Chapter 5 - Condensation and freezing phenomenon on Titanium (Ti) nanopillared glass surfaces

5.1 Surface characteristics

The high fracture toughness of Titanium (Ti) makes it an excellent material for the fabrication of thin, lightweight, and flexible applications. Hence, MPL followed by lift-off was used to pattern hexagonal close-packed arrays of Ti pillars, as illustrated in literature [98]. The SEM images of the fabricated surfaces are shown in Figure 5.1.

- Sample-1: 2 µm periodicity, 200 nm tall, and 800 nm diameter
- Sample-2: 2 µm periodicity, 200 nm tall, and 781-1006 nm diameter

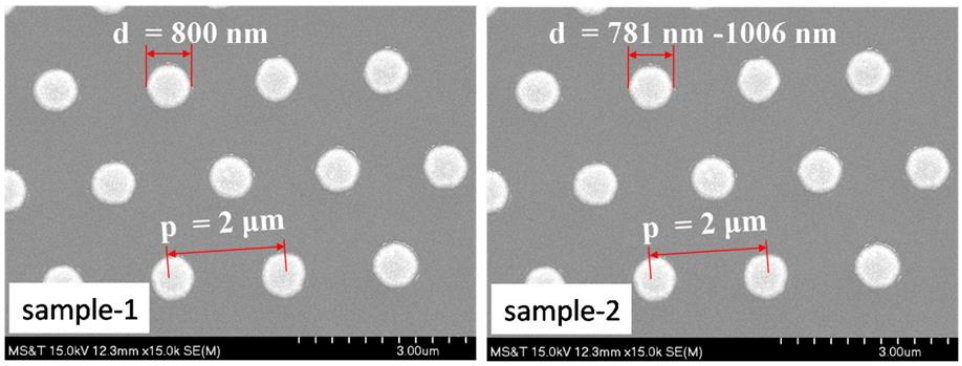

Figure 5.1 SEM images of the finished fabricated Ti nanopillared glass surface.

The hydrophobic Ti nanopillared surface was created by spray coating of the Teflon© and FC-40 solutions as a coating agent [98].

5.2 Wetting properties

The Ti nanopillared surfaces were cleaned before measuring the contact angle (CA) to describe the wetting behavior of the surface. CA measurements of an injected water droplet are reported in Figure 5.2 to characterize the wetting behavior of the surfaces considered.

The static CA for the hydrophilic Ti nanopillared glass surface was 37.2 ± 4.8º. For the Teflon© coated surface, the advancing CA was 115.1 ± 3.3º and the receding CA was 109.3 ± 3.2º. The CA value ensures the different wetting properties of the considered samples.

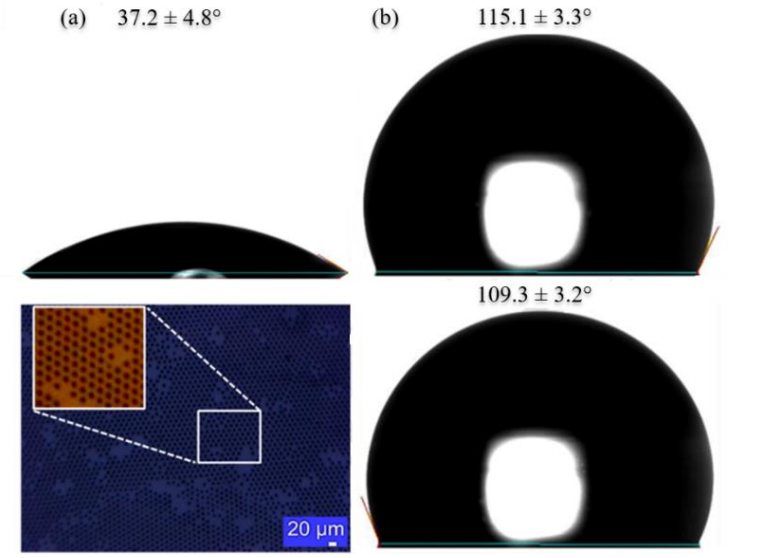

Figure 5.2 Static and dynamic contact angle measurement on (a) plain Ti nanopillared (Sample-1) (b) Teflon© coated Ti nanopillared glass surfaces (coating on Sample-1) respectively. Average CA was considered over 5-6 different spots on the sample.

5.3 Effect of relative humidity on droplet growth

For Sample-1, droplet growth stages: followed by nucleation, direct growth, coalescence were observed within the view field. However, some droplets sweep off from the microscopic view field for Sample-2 at both humidities. The rate of coalescence was higher for Sample-2 compared to Sample-1 under the same condition. Time-lapsed images of the droplet growth on the Sample-1 kept at 278 K have been shown in Figure 5.3. At 295 K room temperature and 60% RH, a lower nucleation energy barrier and higher nucleation rates were observed from Eq. 1.1. For Sample-1, within the first 130 s, droplet density decreases for 60% RH compared to 40% RH due to a higher rate of coalescence events.

However, irregular shaped droplets were observed for both 40% RH and 60% RH, due to the pinning effect from the Ti nanopillared surface. The pinning impedes droplet mobility, coalescence, and growth.

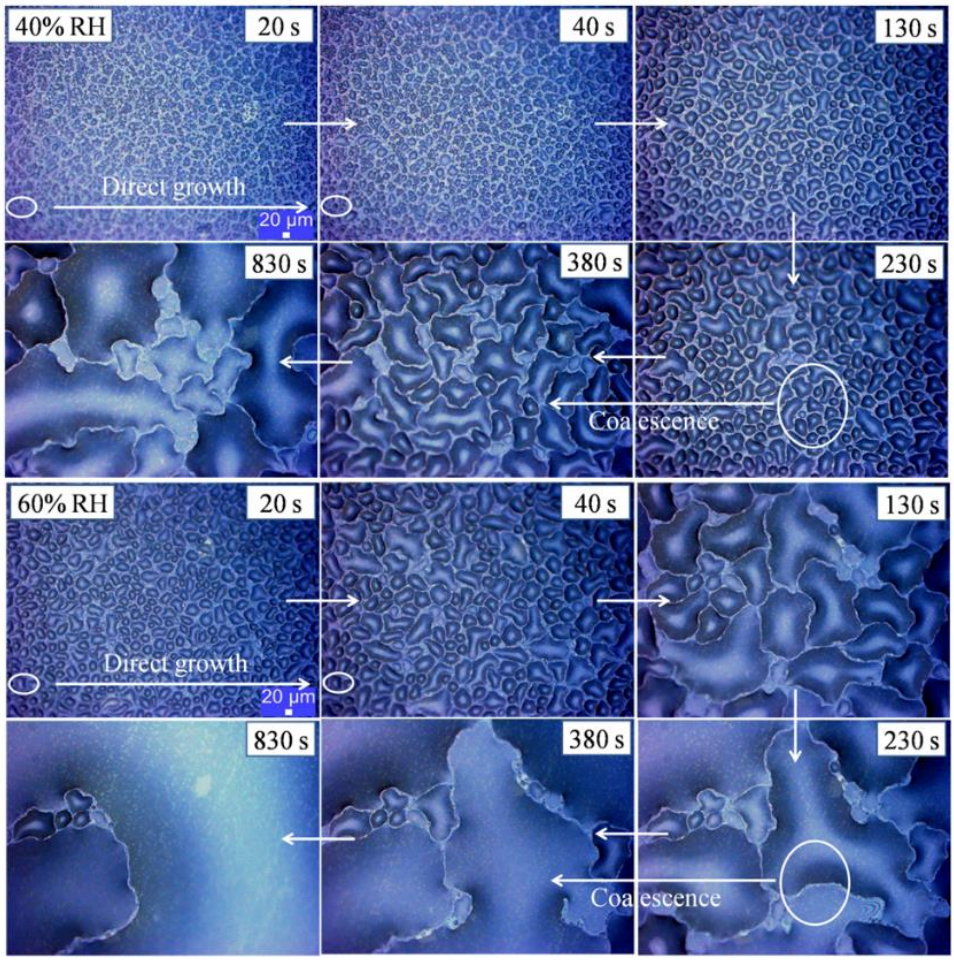

Figure 5.3 Time-lapsed droplet growth on plain Ti nanopillared glass surface (Sample-1) at 40% RH and 60% [98].

Wide variations of droplet diameter was observed in Figure 5.4. The rate of coalescence events and direct growth varies at 40% RH and 60% RH. Hence, variability was observed in droplet diameter compared to 40% RH. Moreover, at t=830 s, lower droplet density and higher area coverage were seen for 60% RH.

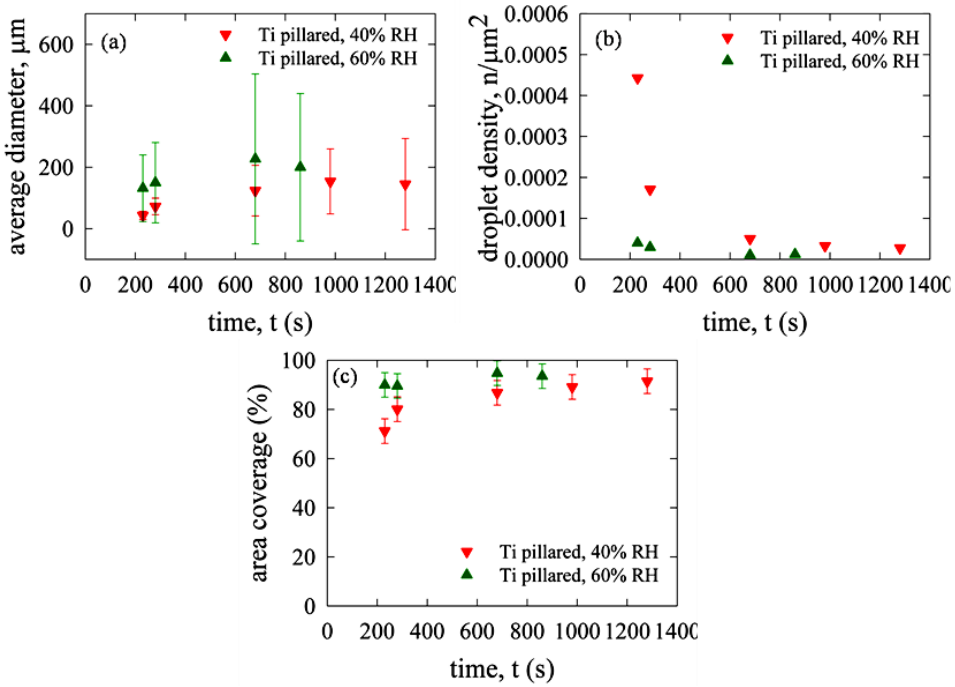

Figure 5.4 Droplet average diameter, density, and area coverage on plain Ti nanopillared glass surface (Sample-1) at 40% RH and 60% RH [98].

5.4 Effect of nanopillared surface on droplet shape and growth

Due to different pinning effect, the more asymmetrical and irregular shaped droplet was observed for 'Sample-1' compared to 'Sample-2', as shown in Figure 5.3 and Figure 5.5.

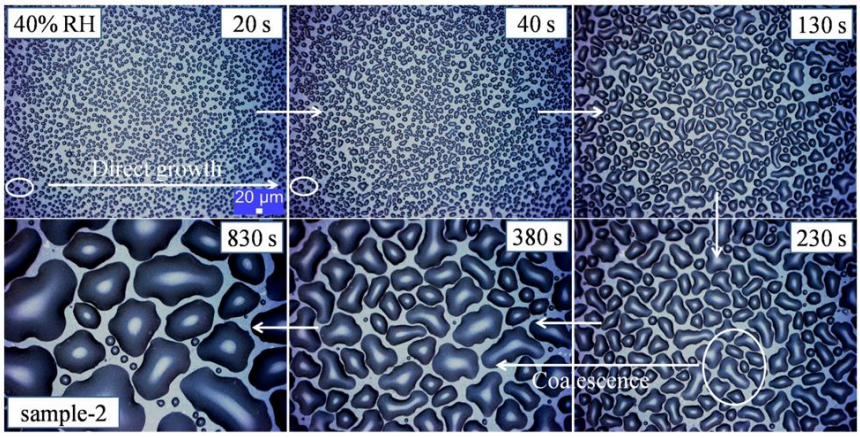

Figure 5.5 Time-lapsed droplet growth on plain Ti nanopillared glass surface (Sample-2) at 40% RH [98].

As less pinning happens for the droplet growing on Sample-2, relatively higher rate of coalescence event occurs.

5.5 Effect of hydrophobic coating on droplet growth

Droplet dynamics changed for the hydrophobic Ti nanopillared glass surface, as shown in Figure 5.6. Due to higher nucleation energy barrier, a lower nucleation rate of the droplet was observed for the coating, as shown in Figure 5.6(b). Fewer coalescence events and less area coverage were also observed. The lower average diameter and lower droplet density were found for the coated surface, as shown in Figure 5.7. Spherical cap shaped condensed droplets with average contact angle higher than 90° has also been observed (side-view) in Figure 5.8.

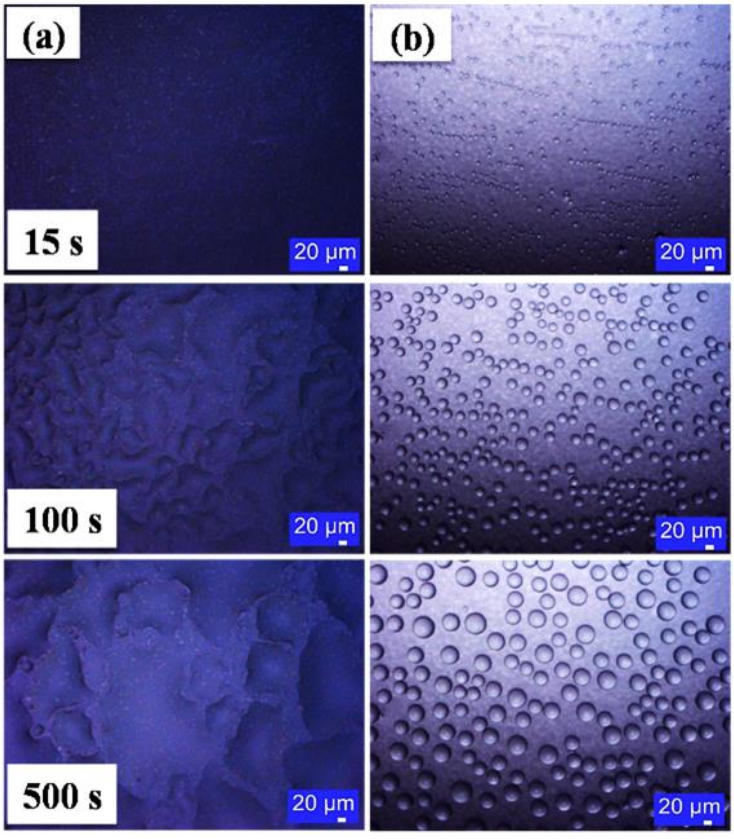

Figure 5.6 Time-lapsed droplet growth on (a) plain Ti nanopillared (b) Teflon© coated hydrophobic Ti nanopillared glass surfaces at 35 ± 5 % RH and 275 K surface temperature [98].

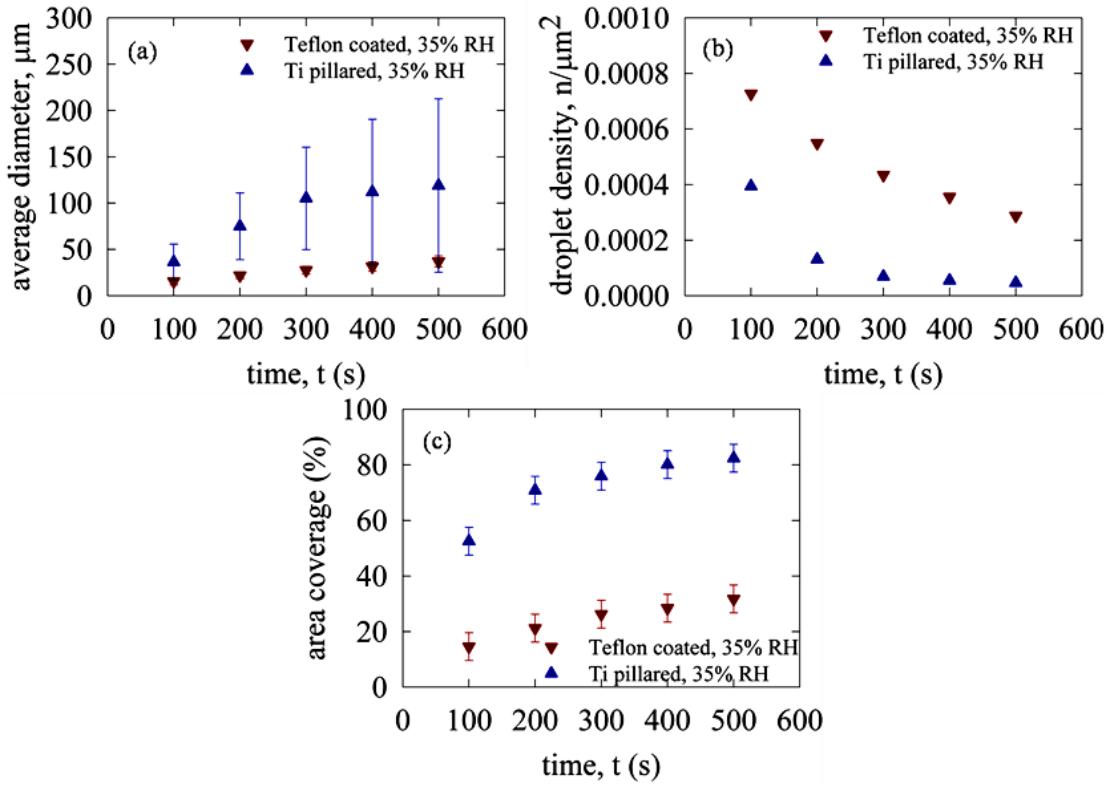

Figure 5.7 Variation of (a) droplet average diameter (b) density and (c) area coverage.

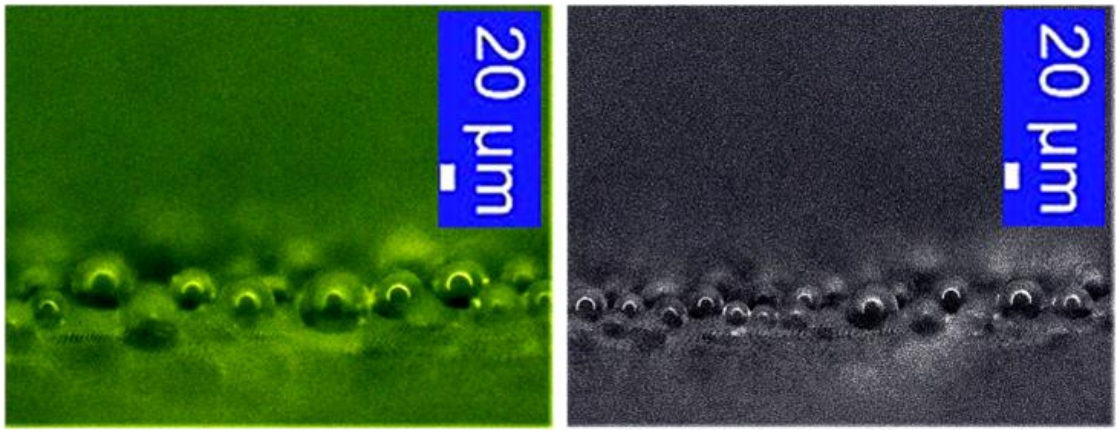

Figure 5.8 Droplet growth images (side view) for Teflon© coated nanopillared surface [98].

5.6 Freezing mechanism on Ti nanopillared glass surface

After the completion of the condensation test, 15 trials of the freezing test have been conducted on the surfaces. Ti nanopillared glass surfaces (Sample-1 and Sample-2) significantly accelerate freezing by pinning droplets. The pinning mechanism impedes droplet mobility, coalescence, and subsequent growth. As observed from Figure 5.9, the coalescence behavior differs between the samples, which eventually alters the size distribution of the droplets.

The surface with lower droplet density and larger sized droplet delays the freezing process. Irregular shaped droplets are observed for both surfaces with some visible ice bridging within the microscopic view field. Pinned and irregular condensed droplets were observed. Detailed quantification of the freezing time is plotted in Figure 5.10.

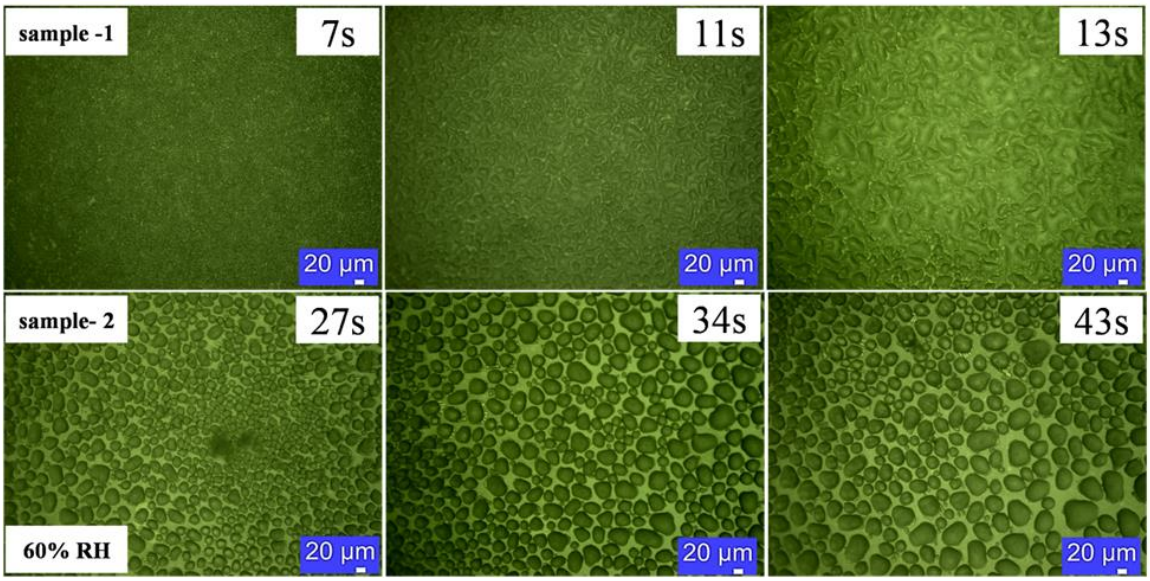

Figure 5.9 Different images taken when the surface under the microscopic view field freezes for 60% RH on 'Sample-1' and 'Sample-2'. Three different trials are shown in a row for each of the samples [98].

5.7 ‘Onset of freezing’ and ‘Freezing delta’ for the considered cases

The ‘Onset of freezing’ is defined as the time when the first droplet in the view of the microscope freeze. When all the droplets on the surface under the microscopic view field have frozen is termed as ‘Final freezing time’. The 'Freezing delta' is defined as the time gap between the ‘Onset of freezing’ and the ‘Final freezing time’. Total freezing time described in Figure 5.10 has two components that are evaluated in details in Figure 5.11 to elucidate the physics of the freezing dynamics. At 40% RH, the Ti nanopillared surface (Sample-1) has an average onset of freezing time of 20.93 s, ranging from 16 s to 25 s with a standard deviation of 2.31 s. Conversely, the Sample-2 has an average onset of freezing of 33.94 s, ranging from 15 s to 52 s, with a standard deviation of 10.64 s. At 60% RH, Sample-1 has the average onset of freezing of 8.95 s, varies from 5 s to 16 s. The standard deviation is 2.68 s. In comparison, the average onset of freezing for Sample-2 at 60% RH is 16.45 s, ranging from 9 s to 27 s, with a standard deviation of 4.35 s. For Sample-1 and Sample-2, the longer the onset of freezing, the higher the final freezing time. Hence, the onset of freezing is an important parameter that finally determines the final freezing time. Moreover, for the case of Sample-1, the droplets are highly pinned and very close to each other. Freezing delta is observed to be 3×-4× lower than the onset of freezing for 40% RH and 60% RH. For Sample-2, at 60% RH, the freezing delta is comparable to the onset of freezing as droplet grows larger in diameter due to less pinning and a higher rate of coalescence events. Hence, for Sample-2, a larger average sized droplet with lower droplet density was observed at 60% RH. Energy is released due to surface area reduction (coalescence events). As a result, it increases the energy required for the freezing as droplet volume increases [44].

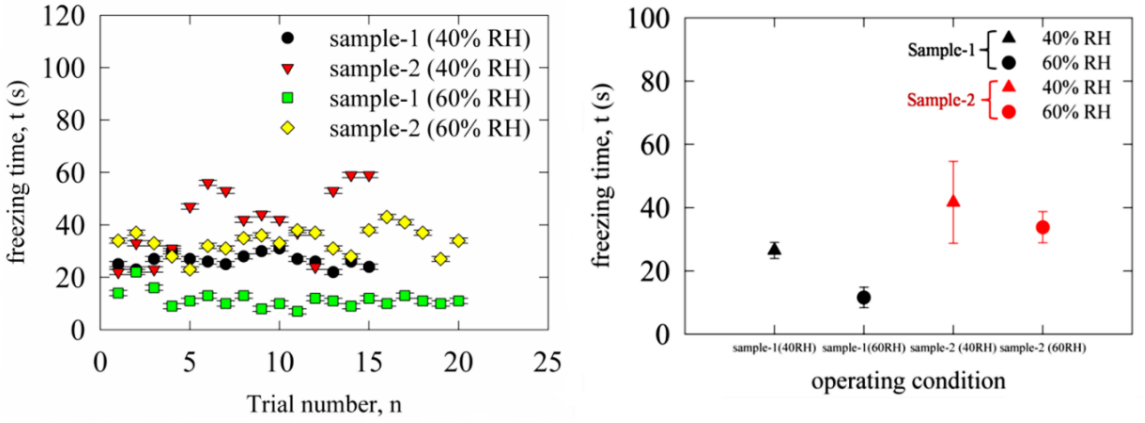

Figure 5.10 Estimation of the freezing times for different trials and the average freezing times for various operating conditions [98].

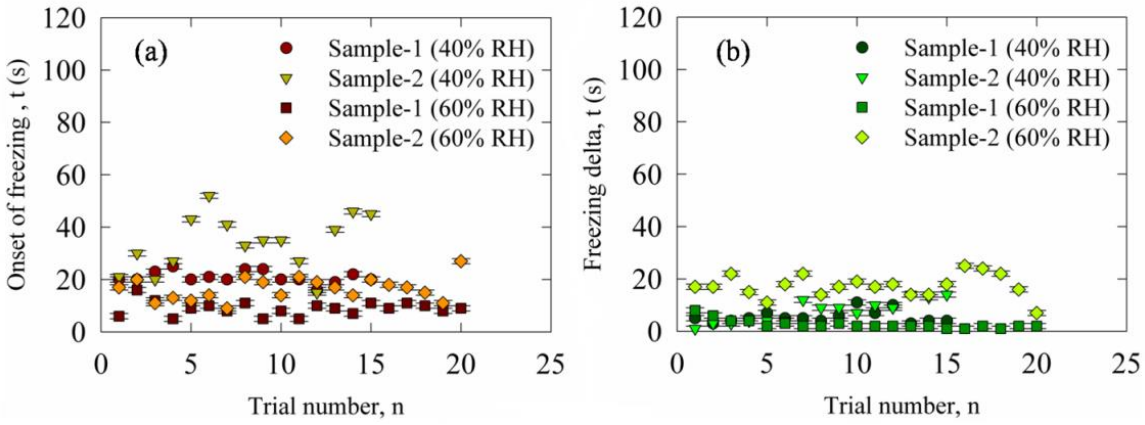

Figure 5.11 Estimation of the 'onset of freezing' and 'freezing delta' for different trials under the stated conditions [98].

5.8 Final freezing time

As earlier mentioned, freezing on nanopillared surfaces showed substantial statistical variations, the final freezing time specified here is compared with the later reported (chapter 7) freezing results on hydrophilic aluminum (Al) and hydrophobic aluminum surface (Al-H). The reported freezing times are summarized in Table 5.1. From Table 5.1, it can be understood that both of the samples (Sample-1 and Sample-2) can accelerate the freezing by order of magnitude compared to plain and both of the mentioned hydrophobic surfaces.

Table 5.1 Total freezing time comparison with a plain surface and hydrophobic surface.

Surface	RH	Final freezing time	Magnification
Ti nanopillared glass surface, Sample-1	40%	26.47 ± 2.55 s	350×
Ti nanopillared glass surface, Sample-1	60%	11.6 ± 3.23 s	350×
Ti nanopillared glass surface, Sample-2	40%	41.67 ± 12.97 s	350×
Ti nanopillared glass surface, Sample-2	60%	33.8 ± 4.92 s	350×
Al	40%	600 ± 60 s	350×
Al	60%	390 ± 60 s	350×
Al-H	40%	900 ± 60 s	350×
Al-H	60%	630 ± 60 s	350×
Silica nanopillars on silicon coated glass surface	40%	73.6 ± 17.3 s	600×
Silica nanopillars on silicon coated glass surface	60%	34.5 ± 11.6 s	600×
Teflon© coated hydrophobic silicon surface	35%	721.75 ± 60.96 s	600×

5.9 Conclusion

At 60% RH, higher surface coverage was observed for Ti nanopillared glass surface compared to 40% RH. It is essential for condensate harvesting. Furthermore, reducing the relative humidity to 40% from 60%, yielded a lower droplet density and area coverage for the Ti nanopillared glass surface. The ‘onset of freezing’ and ‘freezing delta’ was calculated for all the

experimental cases. The longer the onset of freezing, the higher the ‘Final Freezing time’. Both Sample-1 and Sample-2 can accelerate the freezing by order of magnitude compared to plain and hydrophobic surfaces. Moreover, the nanopillar diameter and spacing (Sample-1/Sample-2) can be tuned to get different freezing times.

Chapter 6 - Condensation on plain copper and Graphene Oxide (GO) coated copper surfaces

Graphene [99-108] has demonstrated excellent mechanical and electrical properties. Graphene and graphene oxides have caught many researchers' interest, and it has been already applied for heat transfer phenomena such as condensation [83] and boiling [109] applications. However, all the experiments previously carried out mainly on heat transfer enhancement. The objectives of chapter 6 [110] are to investigate condensing behavior and droplet size distribution on GO coated copper and plain copper surfaces.

6.1 Graphene Oxide (GO) coating on a plain copper surface

Graphene oxide coating was made on the top of the copper block by spray coating. The coating protocol- the plain copper surface was cleaned using a nitrogen gun to remove any dust or debris. Following this treatment, the copper block was dipped into Isopropanol-2 solution before being exposed to UV-Ozone cleaner for 2-3 minutes. Copper (Cu) sample was placed on a hot plate heated at 100 °C. When the plate was heated up enough, spraying of graphene oxide (GO) solution on the top surface of the sample was done. After the solvent evaporates, the graphene oxide layer formed on the top of the copper surface. The surface was fully covered with the black film of the graphene oxide. It was then baked overnight at 90 °C. Temperature below the selected decreases the adherence of the coating to the substrate and beyond this made the film too crispy.

6.2 Surface characterization

To characterize the plain copper and graphene oxide coated (GO) surfaces, contact angle measurement (wetting properties) and microscopic montage stacks analysis (morphology) were conducted in Figure 6.1 and Figure 6.2 respectively.

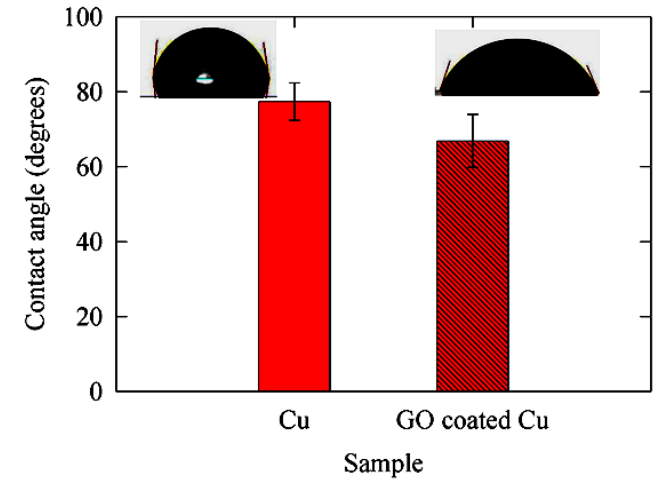

Figure 6.1 Average contact angle of water on plain copper and GO coated copper surface [110].

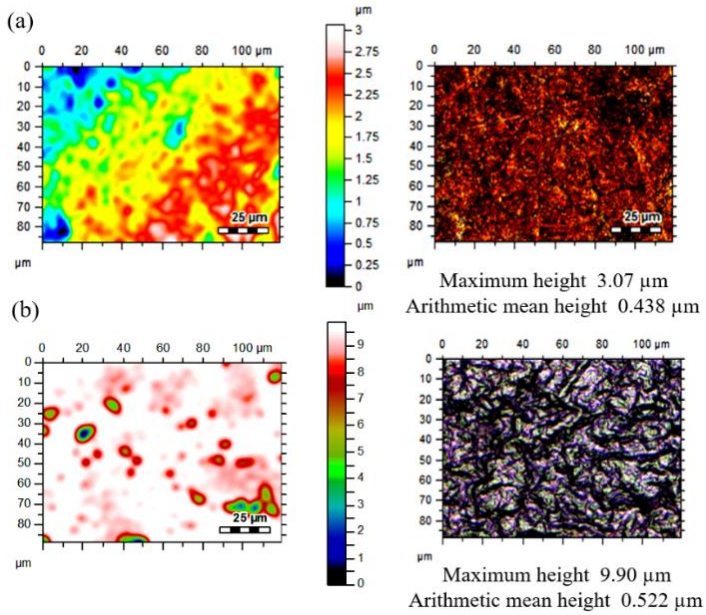

Figure 6.2 Montage images (topography and real image) were taken at 2500× to characterize the surface (a) plain copper and (b) GO coated surface respectively.

6.3 Droplet growth at the initial stage

From Figure 6.3, within the first 60 s, spherical droplets primarily grew by direct condensation and coalescence for plain copper surfaces. However, for GO coated copper surfaces, the droplet dynamics changed. For the GO coated copper surfaces, droplets nucleated, coalescence and span multiple directions by stretching, resulting in the asymmetrical droplets. The droplets may be pinned due to the micro/nanostructure of the graphene flakes on the surface. The micro-nano roughness of the flakes pins the droplets making less movable and stable, which did not prevent droplet growth or merging since droplets continue to grow due to direct condensation at the vapor-liquid interface of the droplet.

Figure 6.3 Droplet growth mechanism for (a) plain copper, 40% RH (b) GO coated copper, 40% RH (c) plain copper, 60% RH and (d) GO coated copper, 60% RH [110].

At 60% RH, the size of the initial nucleated droplets was larger in diameter than 40% RH. For the plain copper surfaces, regular spherical-shaped droplets were formed at 40% RH and 60% RH.

6.4 Surface coverage and droplet size distribution

At later stages of condensation, surface coverage increased significantly compared to the early stages for all the stated cases, as shown in Figure 6.4. Approximate 95% surface coverage was observed for GO coated copper surface, which provides a great insight into the coated surface for condensate harvesting. Further study of droplet diameter distribution was carried out to understand the underlying reason for this higher surface coverage of the coated surface, as shown in Figure 6.5. First, the droplets were uniform for both of the surfaces; the dominant size of the droplet ranges was found 0 µm-10 µm at t=2 minutes, and 0 µm-25 µm at t=29 minutes 40 seconds.

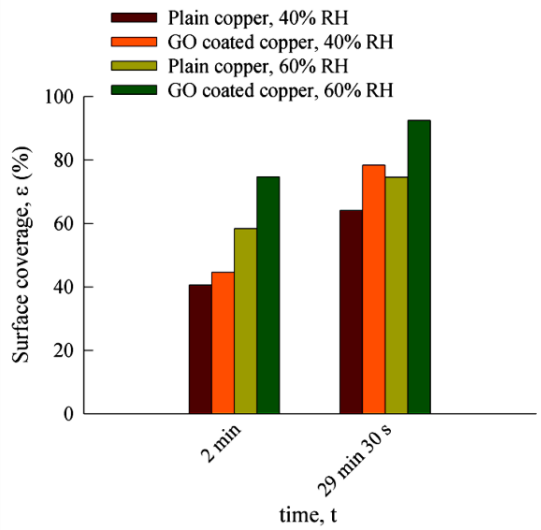

Figure 6.4 The histogram of surface coverage for condensate harvesting applications [110].

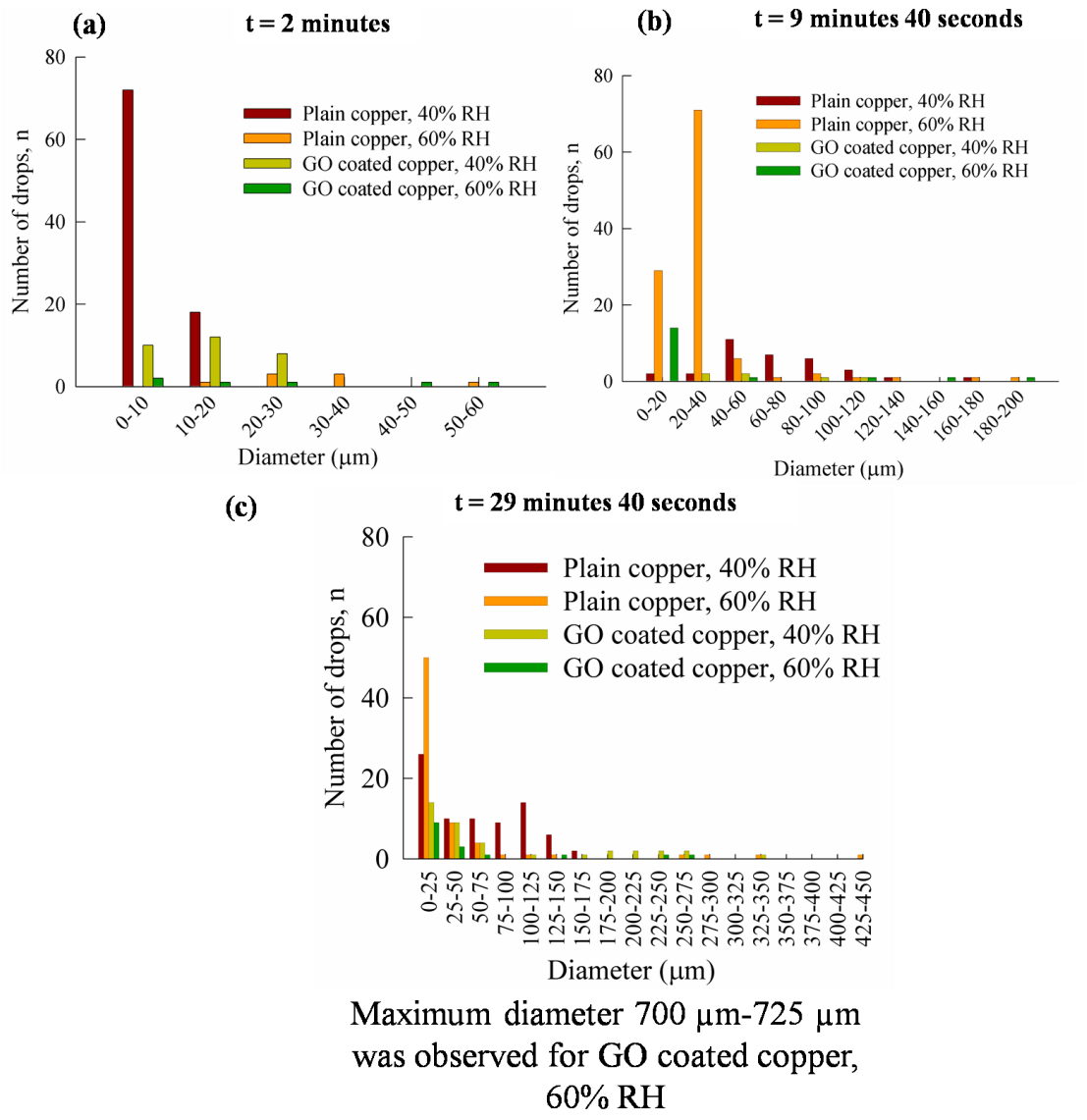

Figure 6.5 Droplet size distribution at three different time [110].

A large number of small-sized droplets appeared for the plain copper, and 60% RH recorded relatively larger sized droplet. The size ranges were found 20 µm-50 µm, 180 µm-200 µm and 700 µm-725 µm for the GO coated surface at three different times considered, as shown in Figure 6.5(a-c).

6.5 Effect of RH on droplet dynamics for different surfaces

Relatively wide range of droplet diameters was observed for GO coated surfaces. The reason might be the pinning of droplets into the micro/nanostructures of the coated surfaces that leads enough time for the first generation droplets to grow larger and made more preferential for subsequent coalescence events to become more significant in size.

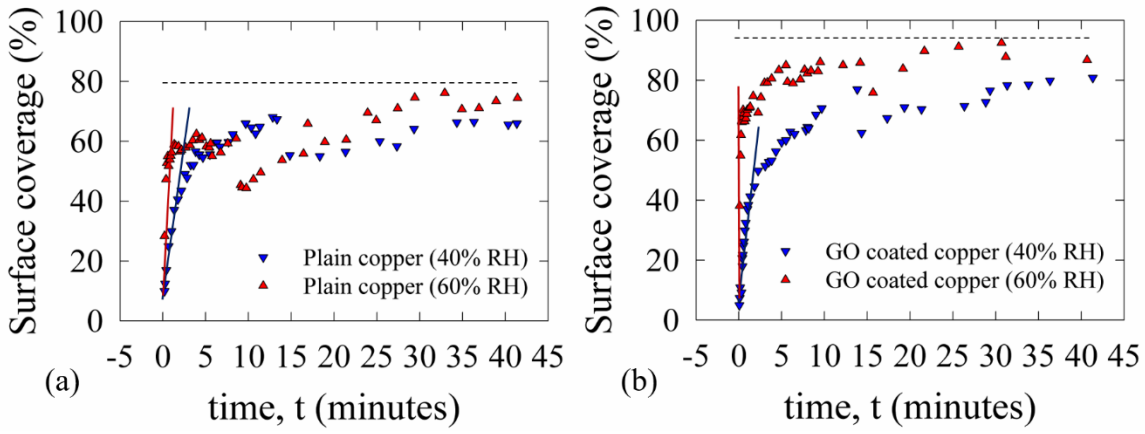

Figure 6.6 Variation of surface coverage for (a) plain copper and (b) GO coated copper surface [110].

At the end of the test, the GO coated surface resulted in higher surface coverage compared to plain copper surfaces, as shown in Figure 6.6. The stable and larger sized droplets generated by the coated surface yields the higher surface coverage.

6.6 Effect of the different surface at 60% RH

The variation of droplet density and surface coverage at a specific RH was discussed in Figure 6.7. The number of droplets per unit area (observed view field) is defined as droplet density. As time passes, the coalescence events happened more spontaneously that reduces droplet density. Although the droplet density seems comparable for both surfaces from Figure 6.7(a), the GO coated copper surface yields higher surface coverage compared to the plain copper surface.

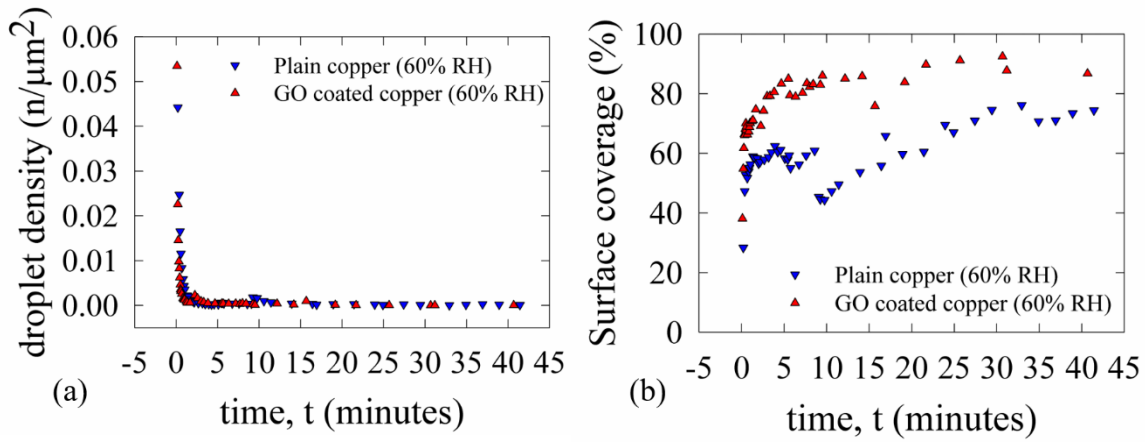

Figure 6.7 Variation of (a) droplet density and (b) surface coverage for plain copper and GO coated copper surfaces at 60% RH [110].

6.7 Growth of a single droplet

Single droplet growth was tracked up to ~ 90 μm diameter on plain copper and GO coated surface to understand the growth dynamics, as shown in Figure 6.8. The graph shifts towards the left for higher RH. At a particular RH, the droplet on a GO coated surface required less time to reach an equivalent final diameter compared to a droplet on plain copper surface.

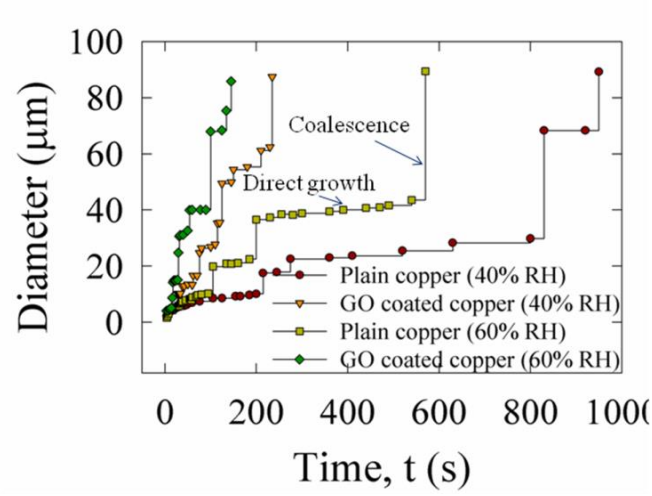

Figure 6.8 Individual droplet growth with time [110].

6.8 Conclusion

The GO coated surface has a significant impact on condensation behavior. The coating procedure is very straightforward. Pinning droplets by the micro/nanostructures of graphene flakes, GO coated surfaces leads to the formation of relatively stable condensate compared to the plain copper surface. Hence, the change in condensation dynamics creates favorable conditions for larger water recovery. The droplet growth rate and surface coverage are found to be higher for the GO coated surface. The transient growth of a single droplet on both surfaces shows the relative importance of coalescence events compared to the inconsistent direct growth in droplet's final diameter.

Chapter 7 - Frost formation on Aluminum (Al) and hydrophobic Aluminum (Al-H) surfaces

7.1 Surface characteristics

Aluminum has significant technical importance as working material. It can be used in HVAC, refrigeration and cryogenic applications, and transmission pipeline [111] etc. However, the main problems are that it oxidizes quickly and wears rapidly. Moreover, Polytetrafluoroethylene (PTFE) is a synthetic fluoropolymer of tetrafluoroethylene that has numerous applications [112]. PTFE is hydrophobic: neither water nor water-containing substances wet PTFE. It is used as the hydrophobic coating agent for the Aluminum surface. The coating protocol has been described in Figure 7.1. The coating procedure is very similar to earlier work [113]. Moreover, Teflon© would act as an excellent protective coating for continuous applications in the harsh environment [114].

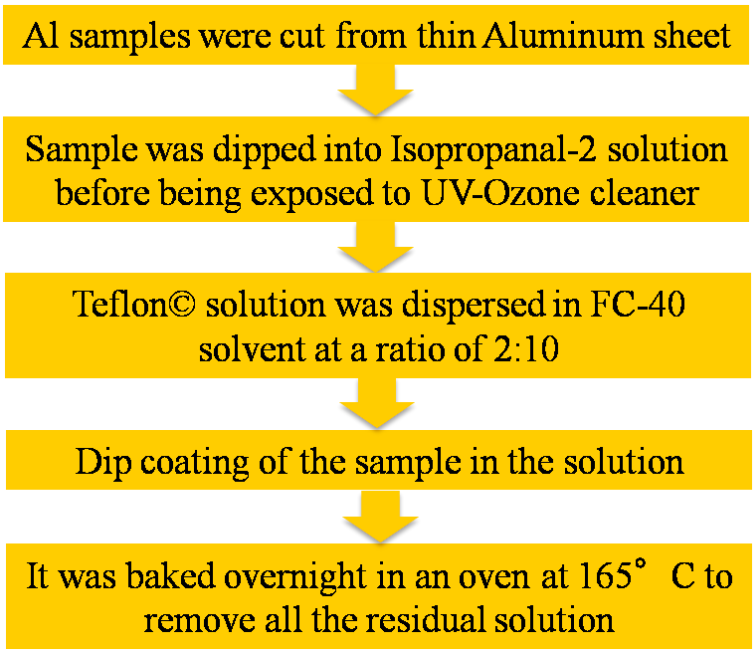

Figure 7.1 The coating procedure for Al-H.

7.2 Contact angle of water on Al and Al-H

After the coating was done, the contact angle of an injected water droplet on these samples were measured to check the wettability of the surfaces [115]. Average contact angle of 60.9 ± 4.55º and 118 ± 0.62° were found for Aluminum (Al), and hydrophobic Aluminum (Al-H) surfaces, as shown in Figure 7.2.

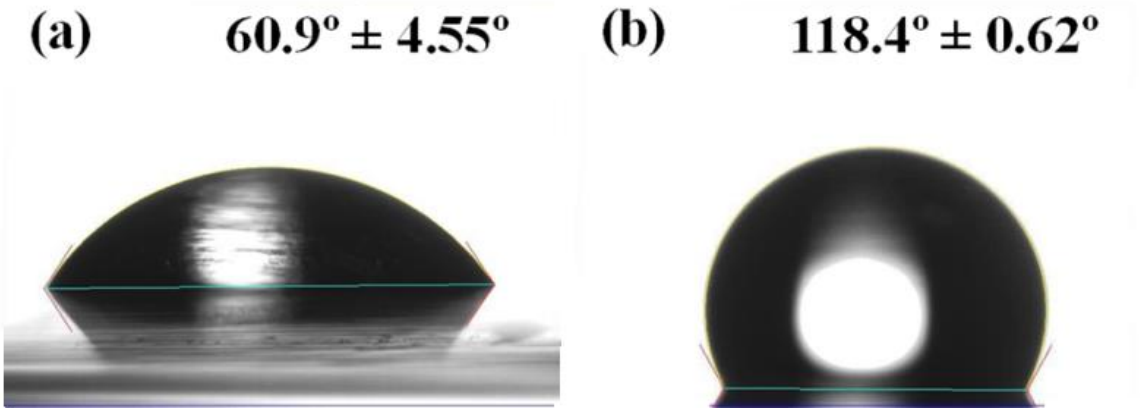

Figure 7.2 Average contact angle of water plain on Al and Al-H surface. The lower standard deviation value for Al-H surfaces indicates the uniformity of the coating on the surfaces [115].

The durability of the coating was checked after ~260 days (~70 icing/deicing tests) of the experimentation with the contact angle measurement at seven different spots of the same sample. The CA was 107.95 ± 3.45°, and ~8.83% decrement of the average contact angle was observed due to repeated cyclic loading and oxidation. The coating was transparent and difficult to find the loss of coating material.

7.3 Droplet shape and wettability

The condensation test has been carried out for the Al and Al-H surfaces to explore the effect of wettability on droplet growth dynamics [115]. Irregular and regular spherical shaped droplets were observed for Al and Al-H surface, as shown in Figure 7.3.

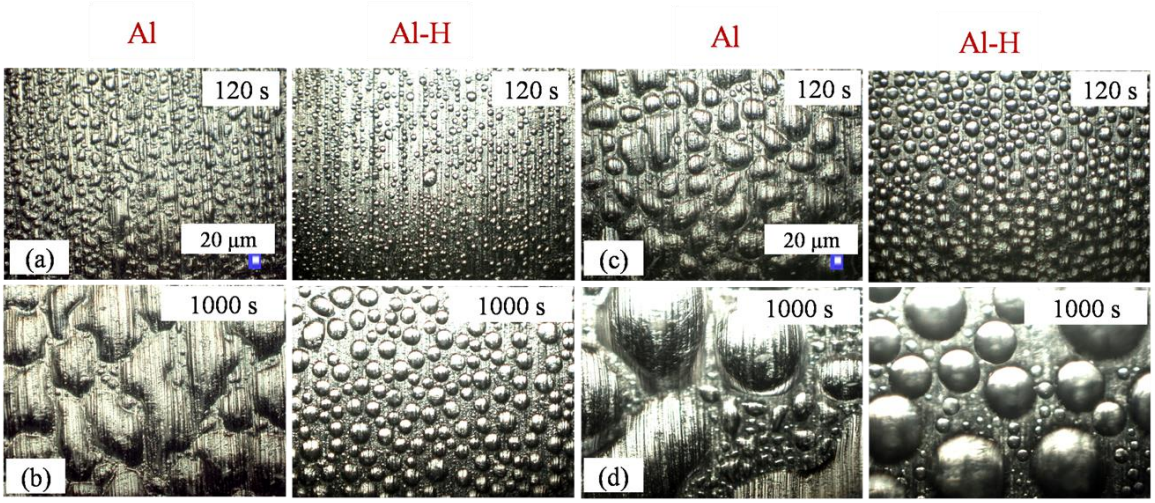

Figure 7.3 Droplet growth mechanism for (a) (b) 40% RH and (c) (d) 60% RH respectively [115].

7.4 Freezing front propagation dynamics

For freezing test, samples were mounted on the Peltier stage and the temperature was reduced to 265 K. In Figure 7.4, at 60% RH, within the first 60 s, asymmetrical shaped droplets primarily grew by direct condensation and coalescence for plain Al surfaces. Moreover, the droplets appeared as a thin sheet very quickly, and the observed view frame froze at t=390 s. For Al surface, fewer coalescence events were observed. However, for Al-H surfaces, the droplet dynamics changed. For the Al-H surfaces, droplets nucleated as spherical shaped and eventually coalesced. The frozen area appeared later for Al-H surface as evident from Figure 7.4(b).

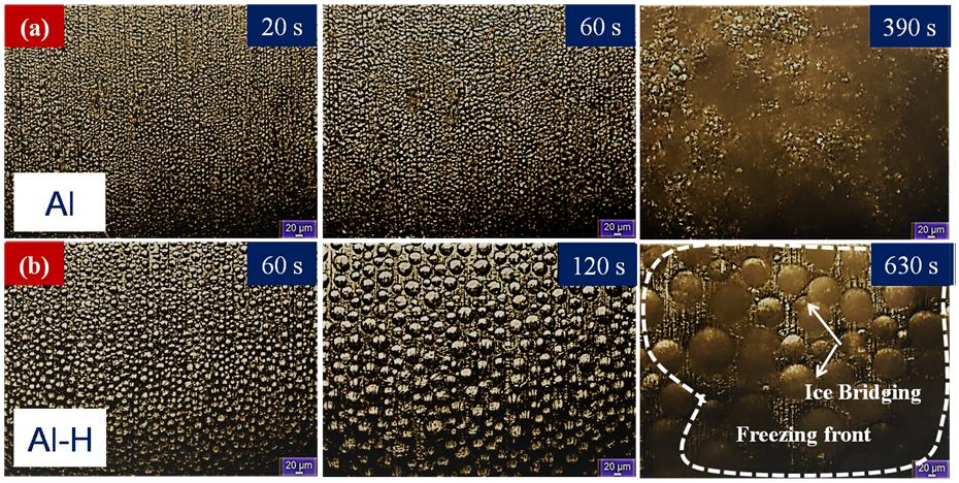

Figure 7.4 Droplet freezing mechanism at 60% RH. The images were represented until the surface within the view field is visualized to be frozen [115].

During testing, little ice bridging was observed between the frozen and liquid droplet within the observed view field, as shown in Figure 7.4(b). This bridging helps to interconnect the cooled liquid droplet with the nearby frozen droplet and turned the liquid droplet into a frozen one. The front propagation velocity is slower for the Al-H surface compared to the Al surface. Increasing droplet mobility, delaying nucleation, creating droplets that project small contact area with the cooling surface, Al-H retards the rate of frost formation. The droplets were seen in coalescence events and become larger in diameter delaying the freezing process [44]. From Figure 7.5, at t=90 s, the droplets nucleated uniformly on the surface. The dominant size of the droplet ranges 25 µm-30 µm (60% RH). With the elapse of time, the distribution peak shifts to the right resulting larger diameter droplet generation due to coalescence events. At t=600 s, the peak shifts to further right to 90 µm-100 µm at the frozen condition, showing the influence of large droplet in subsequent freezing delay [44].

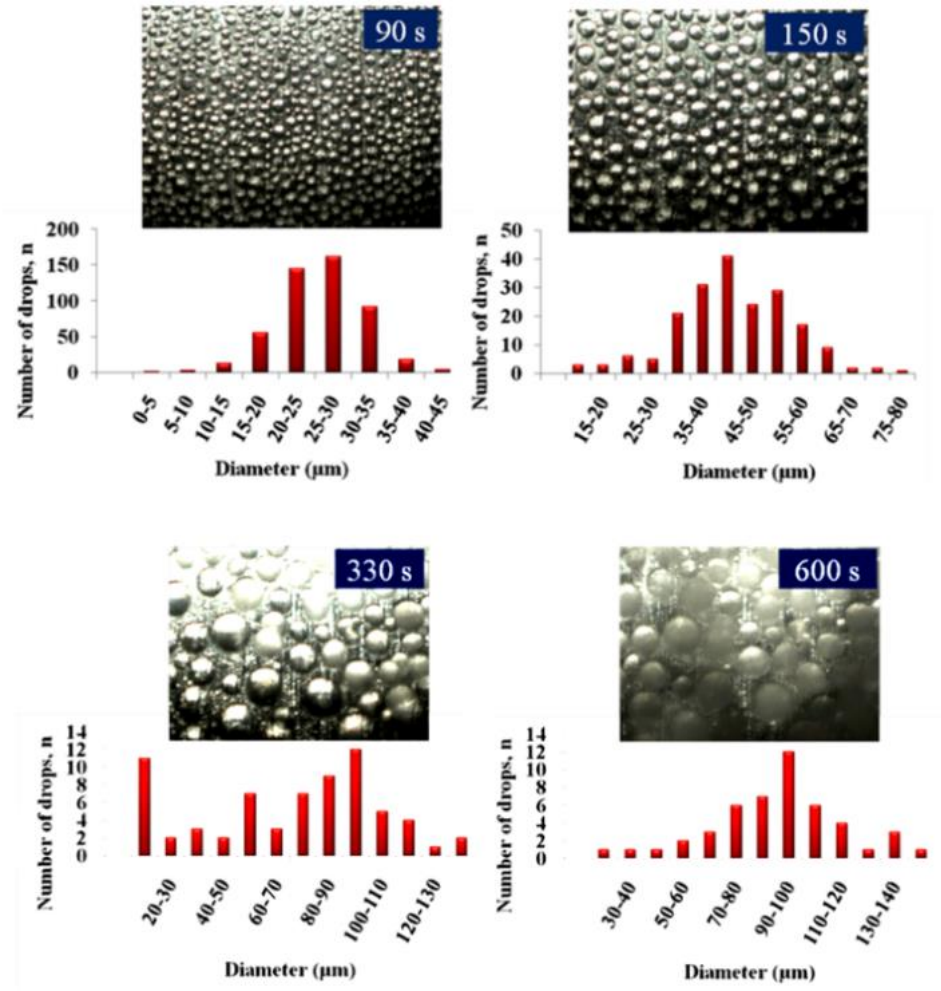

Figure 7.5 Distribution of droplet diameter at (a) t=90 s (b) t=150 s (c) t=330 s and (d) t=600 s for Al-H surfaces at 60% RH [115].

7.5 Freezing front and freezing time

The time required to freeze the whole surface under the microscopic view is considered as 'Final freezing time'. Freezing time is determined based on the consecutive image analysis. The maximum uncertainty of freezing time (±1 minute) was considered as a conservative approximation for the surfaces considered. The highest freezing time ~ 15 minutes was observed for Al-H surface at 40% RH with the minimal front propagation velocity of ~ 1.5 μm/s.

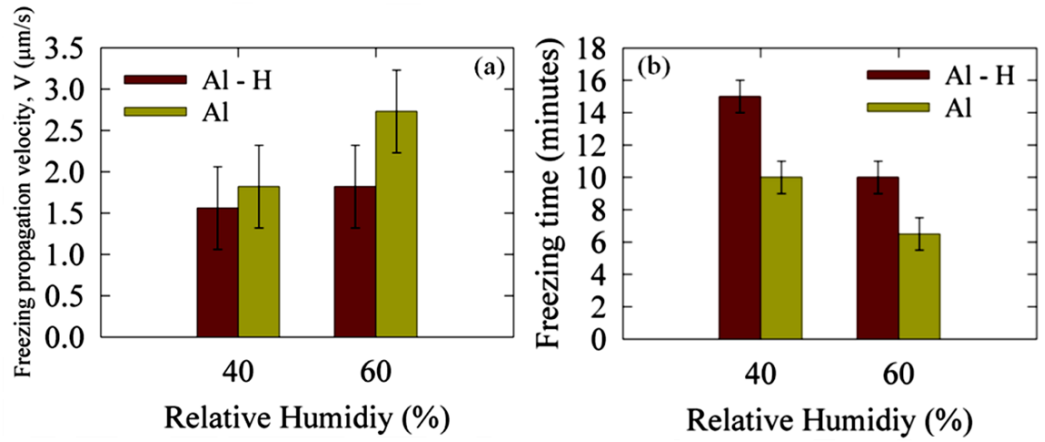

Figure 7.6 Variation of (a) front propagation velocity, (b) final freezing time for all the considered cases [115].

7.6 Conclusion

For bare Al surface, the instantaneous frost front propagation was seen, and frost appeared as a uniform sheet while for Al-H surface, the rate of front propagation was delayed. The rate of droplet coalescence changes the size distribution that controls the effective ice bridging. Maximum ~ 10.5 minutes of the freezing delay was observed for Al-H surface compared to Al surface.

Chapter 8 - Condensation and freezing on hydrophilic and hydrophobic graphene coatings

Understanding of freezing and frost formation mechanism on engineered graphene surfaces is still missing. Hence, such an understanding could enable the development of graphene or graphene derived passive coatings for frost delaying applications. The failure of the surface coating at higher humidity [69], durability based on maximum ~ 40 icing/deicing cycles [56, 116, 117] has already been reported. For hydrophobic coatings, the kinetics and characteristics of ice bridges [43] have not been explicitly discussed. Recently the wetting properties of engineered graphene coatings have been reported by studying the static contact angle of a direct pulsed laser writing (DPLW) of inkjet-printed graphene (IPG) [118]. Das *et al.* [118] showed a direct correlation of a tunable nanostructure with surface energy evolution that was responsible for such wetting behavior. Hence, at Chapter 8, the condensation and freezing test on graphene coating was done [119].

8.1 Surface characteristics

Two samples with different characteristics were considered- a) an atomic flat graphene via CVD process (~ 1 nm to 1.3 nm thick, corresponding to three to four atomic layers of graphene) and b) an engineered graphene coating with higher thickness and higher roughness (~ 5-7 micrometer printed graphene with surface roughness in few hundreds to micrometer scale enabled by a DPLW). The detailed fabrication of the samples can be obtained from the literature [118, 119].

8.2 Contact Angle (CA) of water on graphene coating

Average contact angle measurements were conducted over five different spots on the sample to illustrate the surface wettability, as shown in Figure 8.1.

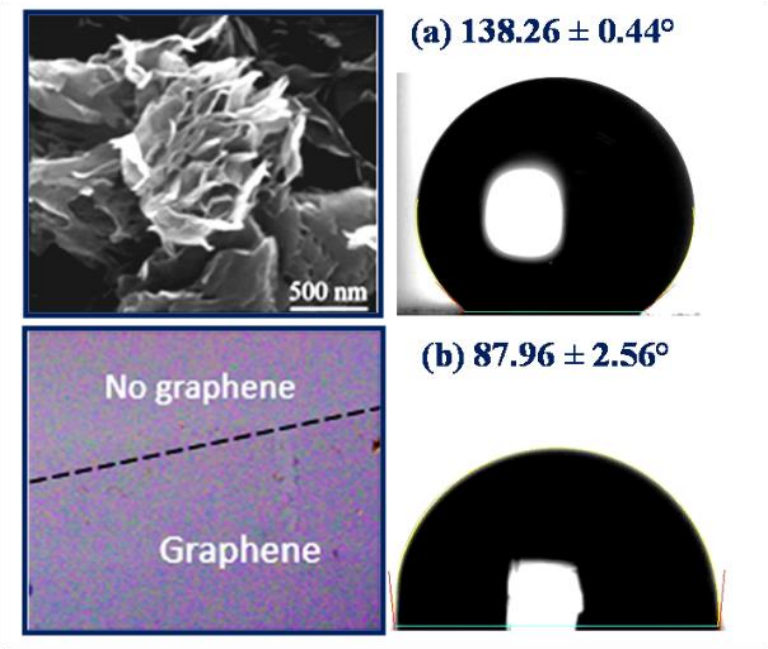

Figure 8.1 The static contact angle of water on (a) IPG 3D-nanostructured graphene coating and (b) an atomic flat graphene coating [119].

Figure 8.1 shows the partial wetting/hydrophilic wetting of the atomic flat graphene coating, and the hydrophobic behavior of the DPLW enabled IPG surface. The corresponding SEM image (of 3D nanostructured, petal-like graphene microstructure) and optical image (of atomic flat graphene) has been shown in Figure 8.1, with the contact angle images. The interfacial (solid-liquid interface) durability of the surface has crucial relevance for practical applications. The change in surface wettability for the atomic flat graphene coating has been explored via ~ 40 cycles of frost testing and ~80 cycles of a sessile droplet (placed droplet on the surface) icing/deicing test as shown in Figure 8.2. Later, the average contact angle was considered for six different spots of the sample in Figure 8.3.

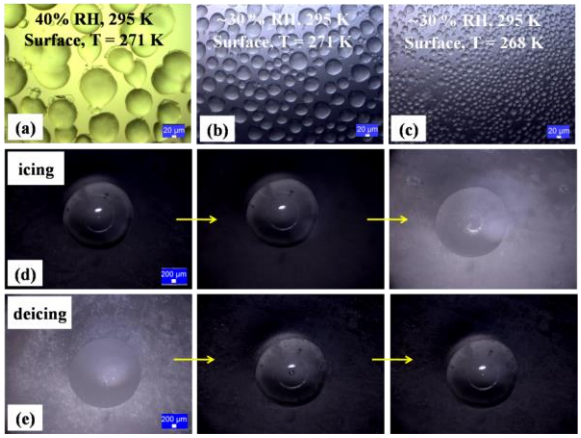

Figure 8.2 Freezing test (a) presented experimental case (b) (c) freezing test on the same sample after ~110 days of the presented experimental case (d) (e) icing and deicing test of a sessile water droplet.

The surface generates spherical-cap shaped droplet in Figure 8.2(b-c) elucidating the wetting stability of the coated surface. Moreover, in Figure 8.2(d-e), icing and deicing test of a sessile water droplet on a spot of the hydrophilic graphene surface at 40% RH and 295 K room temperature has been presented. The surface was kept at a temperature of 265 K. As shown in Figure 8.3, there was no discernable change (<1%) in the contact angle measurement during the cyclic test.

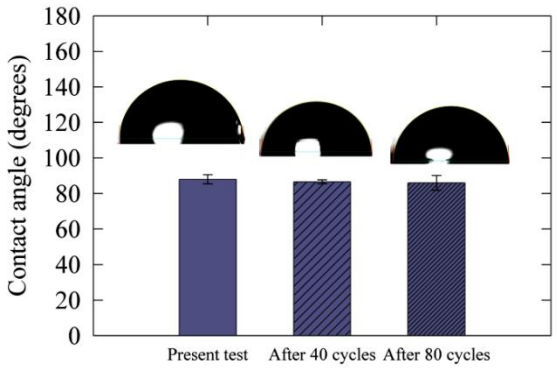

Figure 8.3 Average contact angle of water droplets on the sample after freezing test and sessile droplet icing/deicing test [119].

8.3 Droplet growth during condensation test

Before the frosting test, the condensation test was carried out for hydrophilic and hydrophobic graphene surfaces to reveal the characteristics of droplet shape and size distribution. In Figure 8.4(a), the time-lapsed growth of droplets was observed on atomic flat hydrophilic graphene surface at 40% RH. Both direct growth and coalescence events contributed the droplet growth.

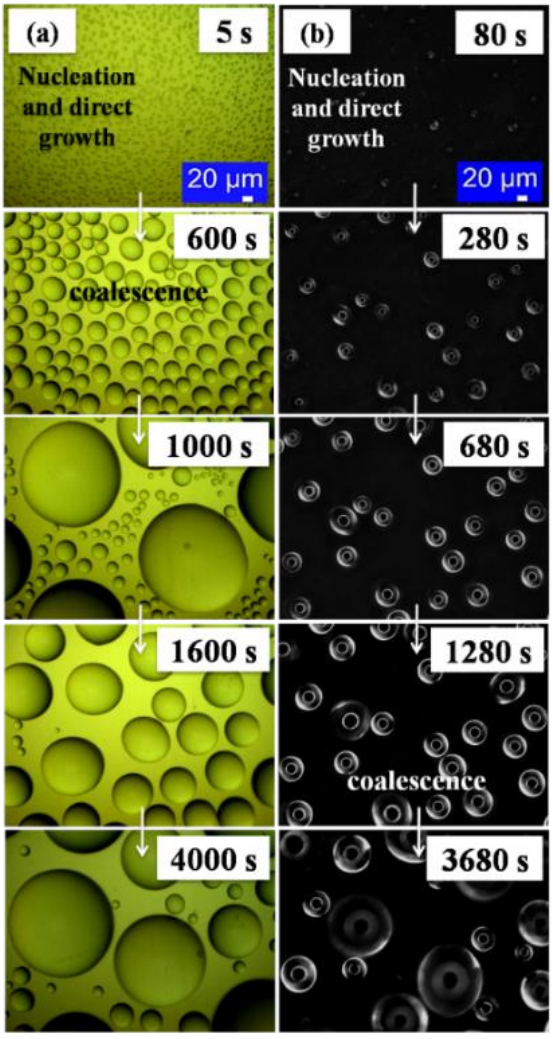

Figure 8.4 Droplet growth mechanism on (a) graphene coated hydrophilic surface, (b) graphene coated hydrophobic surface [119].

Due to higher nucleation energy barrier, the lower rate of droplet nucleation was observed for hydrophobic coating at 40% RH, as shown in Figure 8.4(b). Less coalescence and lower area coverage have also been observed.

8.4 Surface coverage and droplet size distribution

In Figure 8.5(a), a wide variation of droplet diameter was observed for both of the surfaces. The variation is pronounced in the case of the hydrophilic graphene surface due to a higher rate of coalescence events that eventually lead to further renucleation. In Figure 8.5(b), surface coverage in percentage was plotted for both hydrophilic and hydrophobic graphene surfaces, and the difference in the percentage values gradually decreases over the observed time-lapsed.

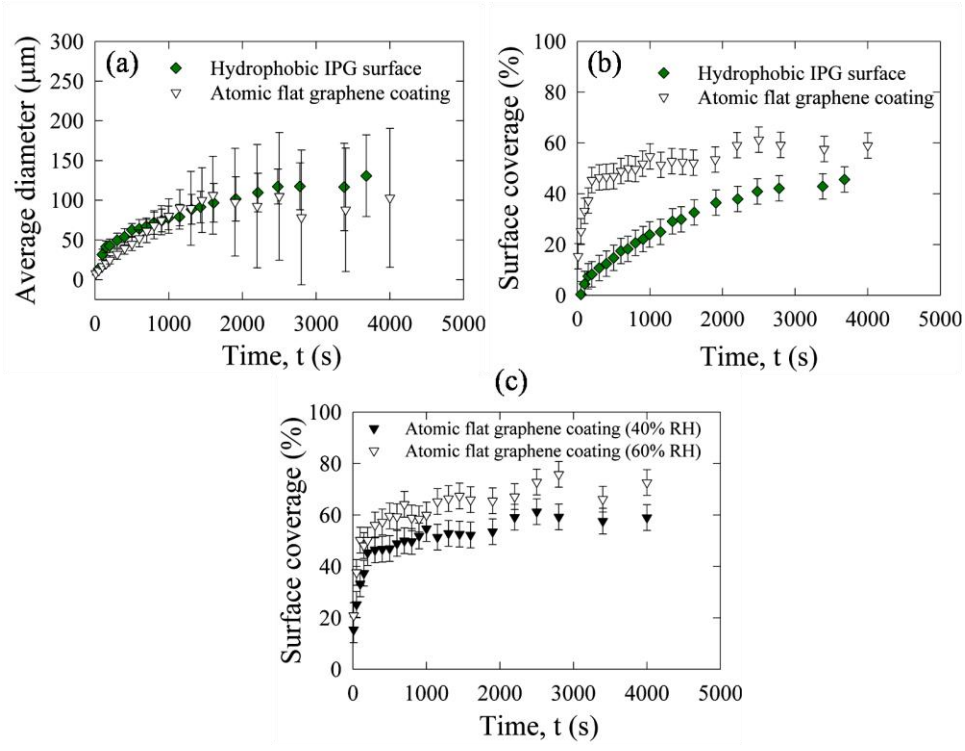

Figure 8.5 Variation of (a) average diameter (b) surface coverage for hydrophilic and hydrophobic graphene coating (c) surface coverage for hydrophilic graphene surface at 40% RH and 60% RH [119].

At 40% RH, at the end of the test, ~40% increment of surface coverage was seen for hydrophilic graphene surface compared to the hydrophobic graphene surface. Altering the RH to 60% results in ~25% increase of surface coverage for the hydrophilic graphene surface.

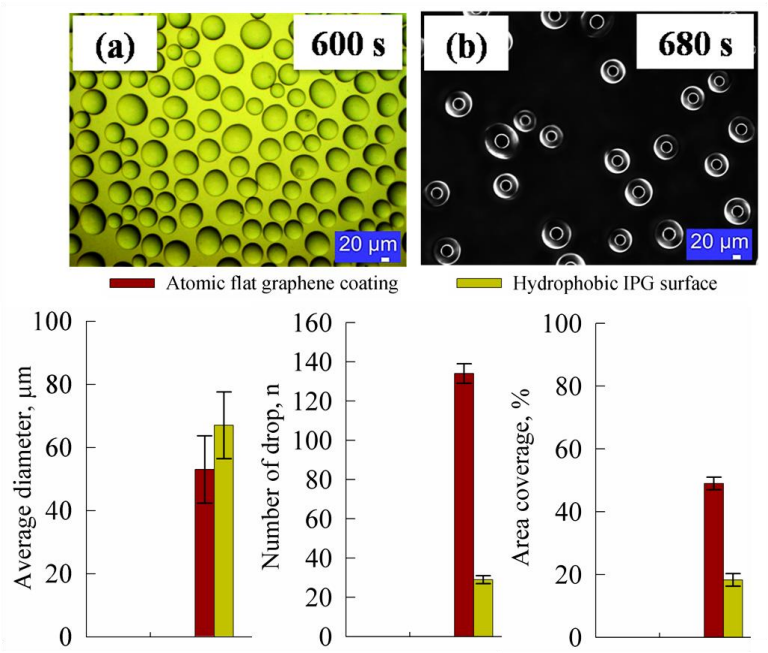

Figure 8.6 Droplet size distribution and area coverage for (a) atomic flat graphene coating (b) hydrophobic graphene coating at 40% RH [119].

Under the same experimental conditions, the wetting properties play a more crucial role in area coverage. In Figure 8.6(b), lower droplet density was observed for the hydrophobic graphene surface. It could be a better insight of hydrophobic graphene surface for frost delaying mechanism and less volume of condensate frost formation. Later, freezing tests were presented. A plain silicon surface was also tested to compare the freezing time.

8.5 Freezing dynamics for hydrophilic graphene surface

First, to evaluate the effect of relative humidity on freezing dynamics, the freezing test for hydrophilic graphene surface has been conducted for 40% RH and 60% RH at various surface temperatures. The different size distribution of droplets was shown in Figure 8.7 and Figure 8.8.

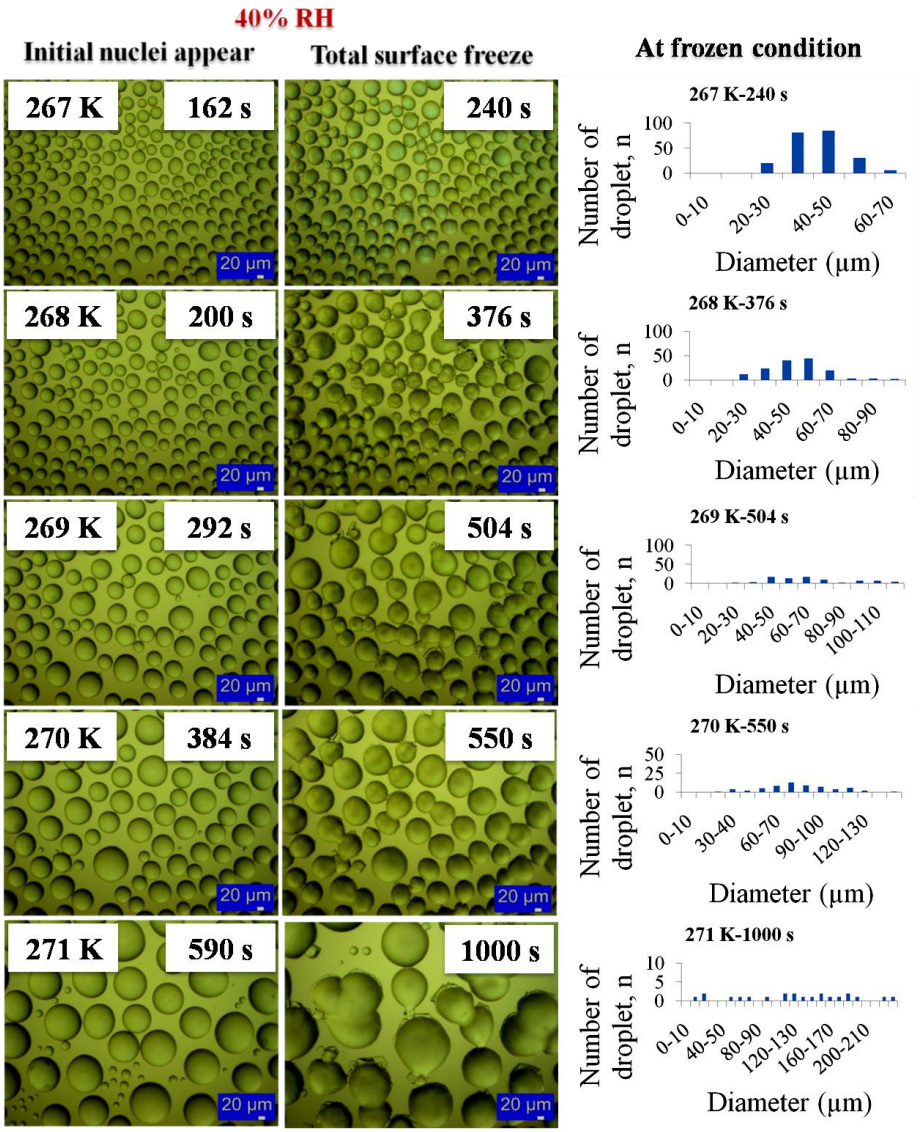

Figure 8.7 Freezing tests on hydrophilic graphene surface at 40% RH for different surface temperatures. The droplet size distribution has been presented at the frozen condition [119].

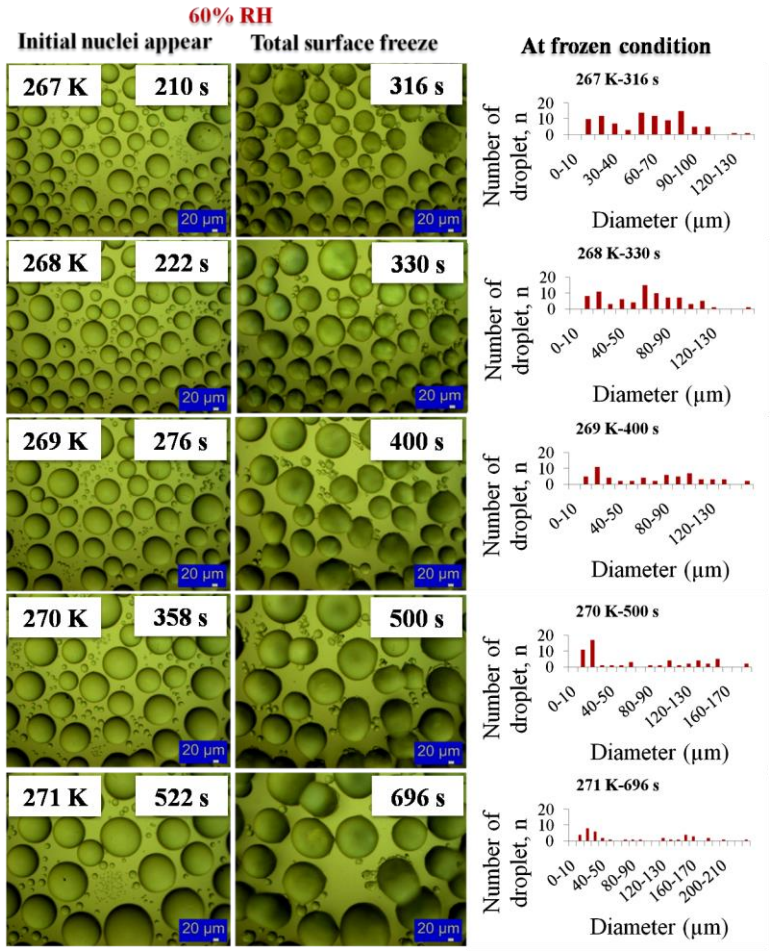

Figure 8.8 Freezing tests on hydrophilic graphene surface at 60% RH for different surface temperatures. The droplet size distribution has been presented at the frozen condition [119].

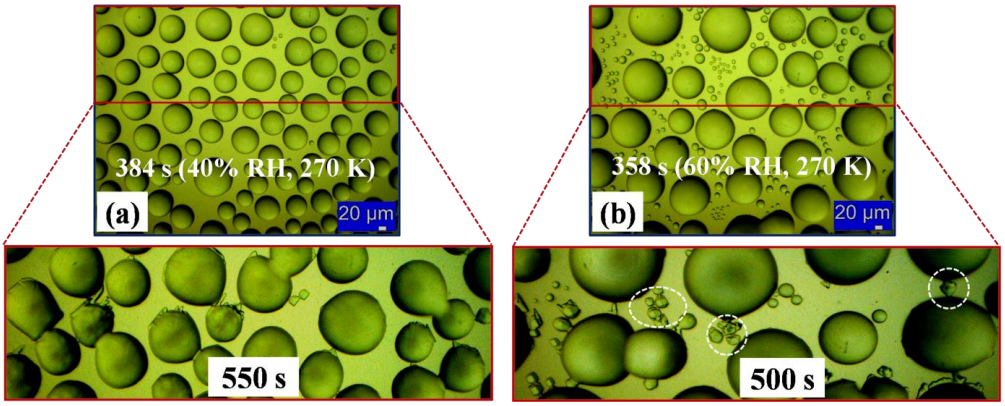

Figure 8.9 The freezing kinetics on hydrophilic graphene surface at 40% RH and 60% RH [119].

At 60% RH, the renucleation rate was found higher for the same time-lapsed, which eventually shifts the droplet distribution to bimodal (Figure 8.8) from lognormal. In Figure 8.9, the coalescence rate and the presence of renucleated droplet (white dotted circle) promote the higher occurrence of ice bridge formation at 60% RH. This smaller regenerated droplet in between the larger droplet might promote the faster propagation of freezing front via effective ice bridging.

On a global basis, the time required to freeze the total surface under the microscopic view of field is evaluated for 40% RH and 60% RH. In Figure 8.10(a-b), the entire time needed for a surface to be frozen is composed of two time components- 1) the time required to appear the first frozen droplet in the view field (onset of freezing) and 2) the front propagation from the first frozen droplet to complete all the successful bridging between the subsequent frozen and cooled liquid. Once the first frozen droplet appeared in the view field, freezing front propagates very quickly via the inter-droplet wave propagation until the whole surface was frozen. This front velocity is relatively slower at higher surface temperatures as larger ice bridges need longer time to propagate. At lower surface temperature (265 K), the occurrence of smaller ice bridging was higher, and the ice bridge spreads very quickly within the view of field. As shown in Figure 8.10(a-c), the relationship between the freezing time and the surface temperature is nonlinear, and maximum ~1.6× freezing delay was observed at 271 K surface temperature for the hydrophilic graphene surface. The front propagation time that initiates from the first frozen nuclei within the microscopic view field were observed to be higher for 40% RH compared to 60% RH.

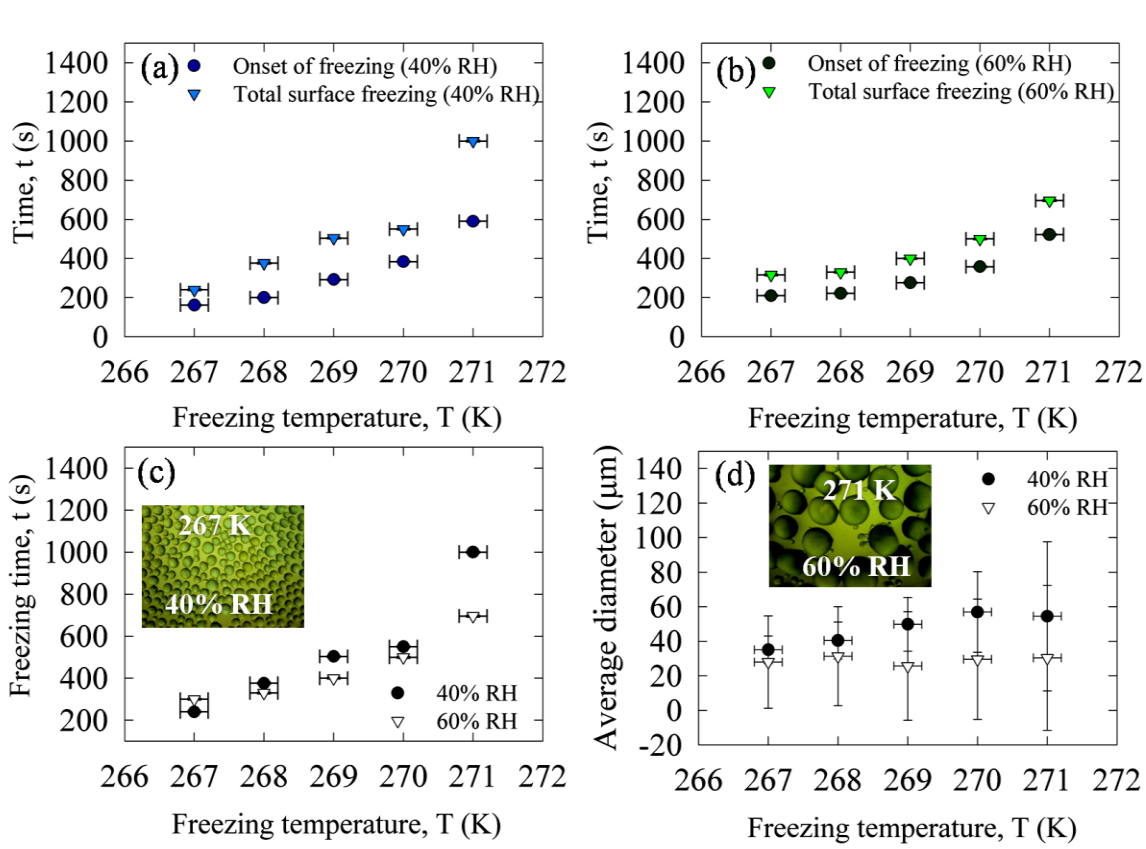

Figure 8.10 (a) (b) Variation of the 'onset of freezing' and 'freezing time' for the atomic flat graphene coating (c) variation of final freezing time and (d) droplet average diameter with various surface temperature [119].

On a local basis, for hydrophilic graphene surface, the freezing front and its propagation mechanism have been described in Figure 8.11 [55]. The bridging helps to interconnect the cooled liquid droplet with the frozen droplet and turned the cooled droplet into a frozen droplet via the water vapor transfer. Different vapor pressure exists over the two different phases (cooled liquid has a higher vapor pressure than ice and cooled liquid begin to equilibrate by losing water). The latent heat rejection from the local frozen droplet released to the surface might evaporate the cooled liquid before the effective ice bride forms [55]. Hence, the success of bridging depends on the relative distance between the droplets as well as diameter of the droplet involved in the bridging process [55].

The lower surface temperature changes the local pressure gradient significantly, enhances the mass transfer to form the effective ice bridge. Hence, the surface freezes faster at lower surface temperature. The front starts and then propagate quickly via the inter-droplet bridging that spreads as chain reaction (white arrow indicated the direction of freezing front propagation). The freezing time is the function of bridging length, bridging time, pressure/vapor concentration gradient over the droplet, and the diameter ratio of the droplet involved in the process of forming ice bridging. However, this ice bridge can be developed effectively between any two of the different sized droplets, as shown in Figure 8.11B. The dashed line in Figure 8.11B indicates the droplet size reduction due to evaporation phenomenon.

The success of ice bridging is dependent on the bridging parameter, $S=l/d$, where l is the edge to edge distance between the droplet involved and d is the diameter of the liquid droplet [55].

Around 25 ice bridges were chosen from ~50 ice bridges as a sampling data for the estimation of S values and other essential parameters (ratio of the frozen droplet to cooled droplet diameter, bridging time) involved in the formation of effective ice bridging. The bridging parameter (S) has also been calculated based on experimental data for three different surface temperatures and was found <1, which is consistent with the literature [55]. When $S>1$, the bridge is not formed as the nearby liquid droplet might evaporate due to heat releases via the latent heat of vaporization from the neighboring just frozen droplet. The bridging time is defined as the total time required to complete an ice bridge between a frozen droplet and a cooled droplet.

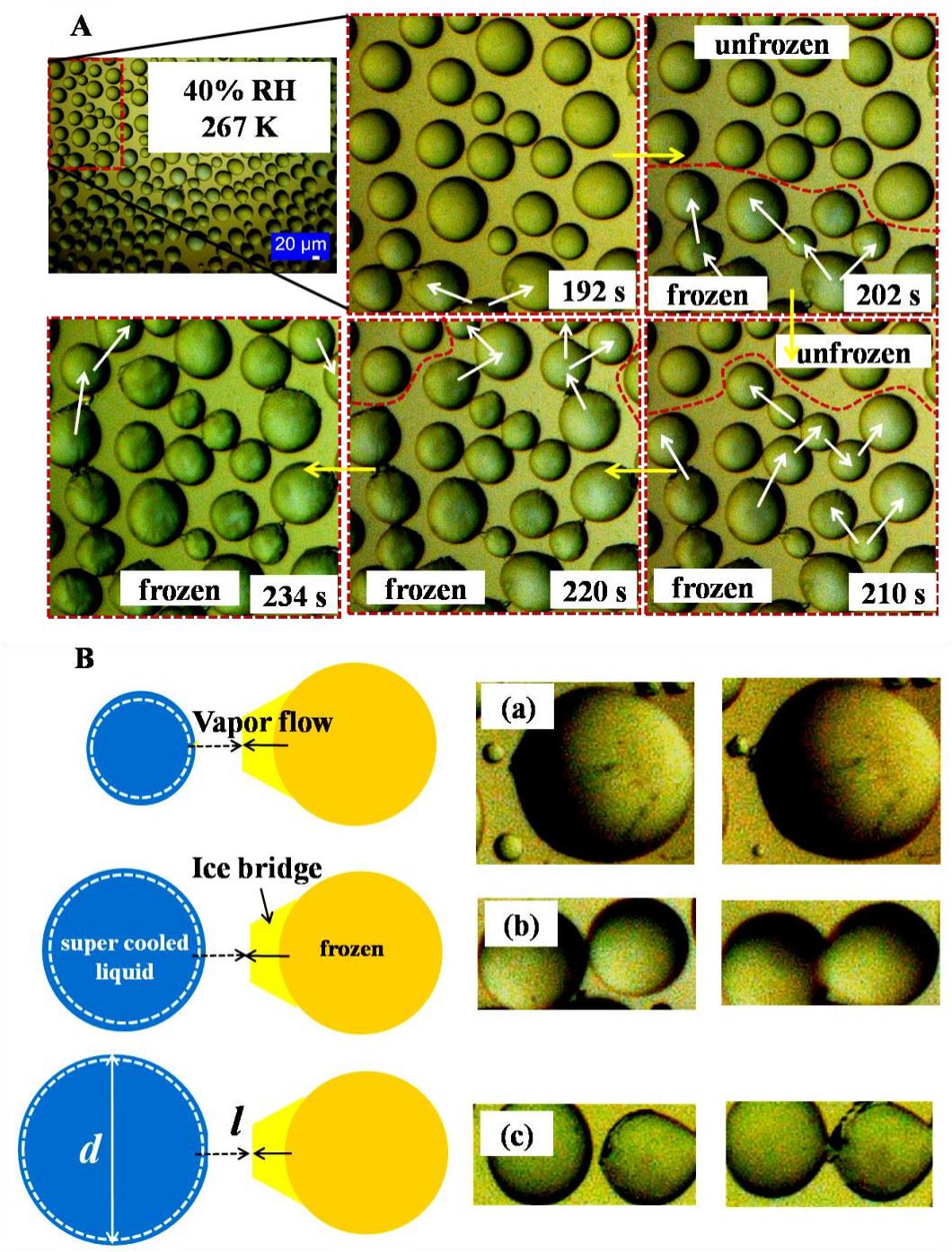

Figure 8.11 (A) Freezing front propagation for hydrophilic graphene surfaces (B) Three different modes of ice bridging, S= l/d [55], that might form between the evaporative liquid droplet and frozen condensate [119].

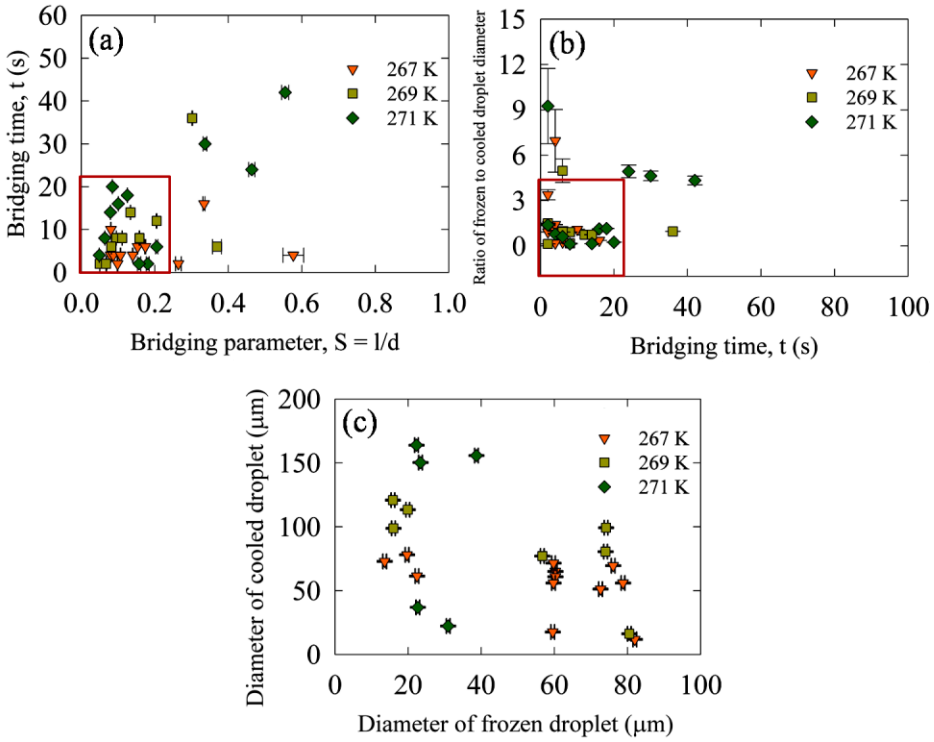

Figure 8.12 Variation of (a) bridging time with the bridging parameter, (b) the ratio of frozen to nearby cooled droplet diameter with the bridging time, and (c) cooled droplet diameter with the frozen droplet diameter for the successful bridges at 60% RH [119].

The effect of bridging parameter on bridging time is illustrated in Figure 8.12(a). For most of the ice bridges (marked in a red box), the value of *S* is found to be less than 0.2 and required less than 22 seconds for the bridge formation. As *S* increases, higher bridging time is observed for 271 K. *S* values close to 0.6 require bridging time less than 5 seconds. The ratio of frozen droplet diameter to cooled liquid droplet diameter is found to be less than 3 for this bridging time (<22 seconds).

In Figure 8.12(c), wide ranges of the frozen droplet and nearby cooled liquid droplet diameters are observed that successfully establish effective ice bridges. From Figure 8.13, it was found that 60% RH requires less time to develop most of the ice bridges compared to 40% RH. As the surface temperature decreases, most of the ice bridge needs less time to complete.

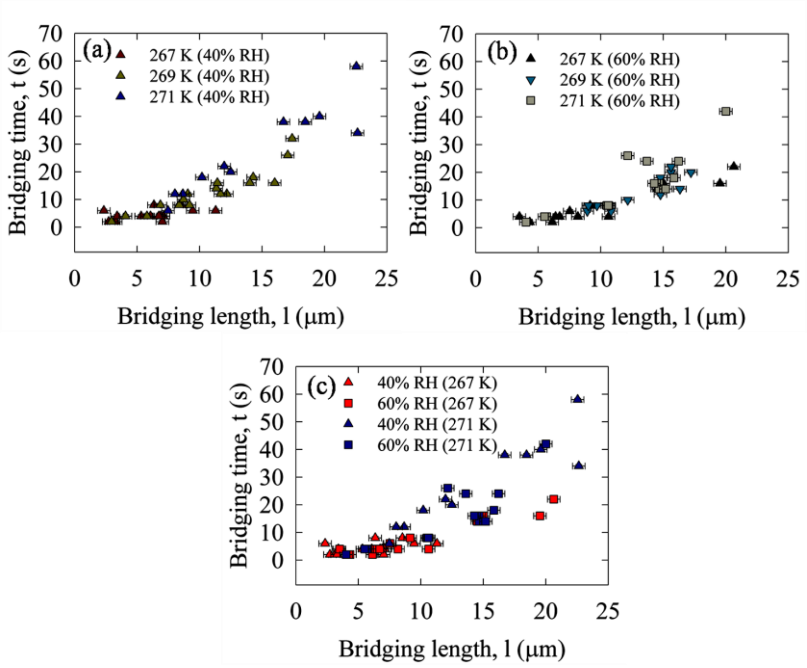

Figure 8.13 Variation of bridging time with bridging length for various surface temperatures [119].

Figure 8.13(c) has been plotted to resolve the effect of RH and surface temperature in ice bridge formation. Although the variations of the bridging time for the plotted data are less sensitive to RH, the effect of the change of surface temperature is easily discernable. Moreover, for most of the data, the ice bridge formation time decreases significantly with the decrease of surface temperature.

8.6 Theoretical ice bridge velocity

The value of individual ice bridge velocity has been reported based on the time required to occur an effective ice bridge between the liquid and frozen droplet. Theoretical velocity has been calculated based on an approach provided in the literature [47, 120]. The mass transfer is mainly by the diffusion process and can be obtained from the theory of mass diffusion. Fick's laws give the most straight forward description of diffusion, states that the diffusion of mass flux (N) is proportional to the concentration (C) gradient.

$$N = -D.\vec{\nabla}C \qquad \text{Eq. 8.1}$$

Here, D is the diffusion coefficient for water vapor from the air and is considered as 10^{-5} m^2 /s [67]. For simplicity, applying linear approximation to the concentration gradient along the bridge length of the formed ice bridge-

$$\left[\vec{\nabla} C\right] \approx \Delta C/l \approx \frac{(\Delta p)}{R_m T_w l} \approx \frac{(P_l - P_i)}{R_m T_w l} \qquad \text{Eq. 8.2}$$

Where C can be found from the ideal gas law and Δp represents the vapor pressure difference between the water and ice phase, which can be obtained from [121].

A mass balance equation has been established for the successful ice bridging between a frozen (i) and cooled liquid (l) droplet via the momentum balance equation, Eq. 8.1-8.2, moreover, it can be written-

$$\rho_i V_i A_i \approx N \times A_l$$

$$\Rightarrow \rho_i V_i A_i \approx \frac{D(P_l - P_i)A_l}{R_m T_w l}$$

$$\Rightarrow V_i \approx \frac{D(P_l - P_i)}{\rho_i R_m T_w l \frac{A_i}{A_l}} \qquad \text{Eq. 8.3}$$

Where V_i is the theoretical ice velocity, ρ_i is the ice density, A_i is the projected ice area, A_l projected liquid area, and l is the bridging length. As the ratio ($\frac{A_i}{A_l}$) decreases, the bridge velocity usually increases (Figure 8.14).

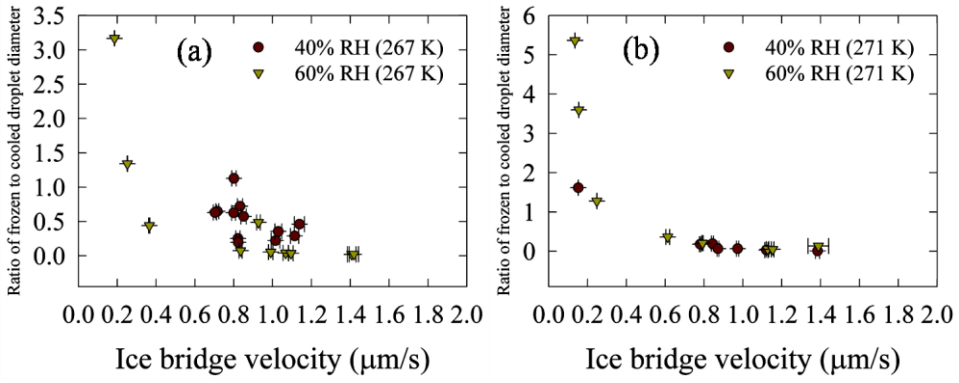

Figure 8.14 Effect of experimental ratio (frozen to cooled droplet diameter) on the ice bridge velocity [119].

8.7 Freezing dynamics for hydrophilic and hydrophobic graphene surface

In Figure 8.15(a), the frost images of condensate droplets for hydrophilic and hydrophobic graphene surfaces have been reported for 267 K-271 K surface temperatures at 60% RH. For hydrophilic graphene surface, at lower surface temperature, droplet density was found to be higher, all the droplets are below freezing temperature and very close to each other (~small *l*). It favors the propagation of freezing front via the successful ice bridging. Droplet size distribution was found to be bimodal, and smaller renucleated droplet triggers the front propagation via ice bridging. Conversely, in Figure 8.15(b), for hydrophobic graphene surface, the droplet dynamics changed significantly. Droplets nucleated as spherical shaped at different spots of the sample and eventually got coalesced at a later stage of the test compared to the hydrophilic graphene surface. Mostly, the droplets froze instantly at the dispersed position, and some ice bridges were observed within the observed view field.

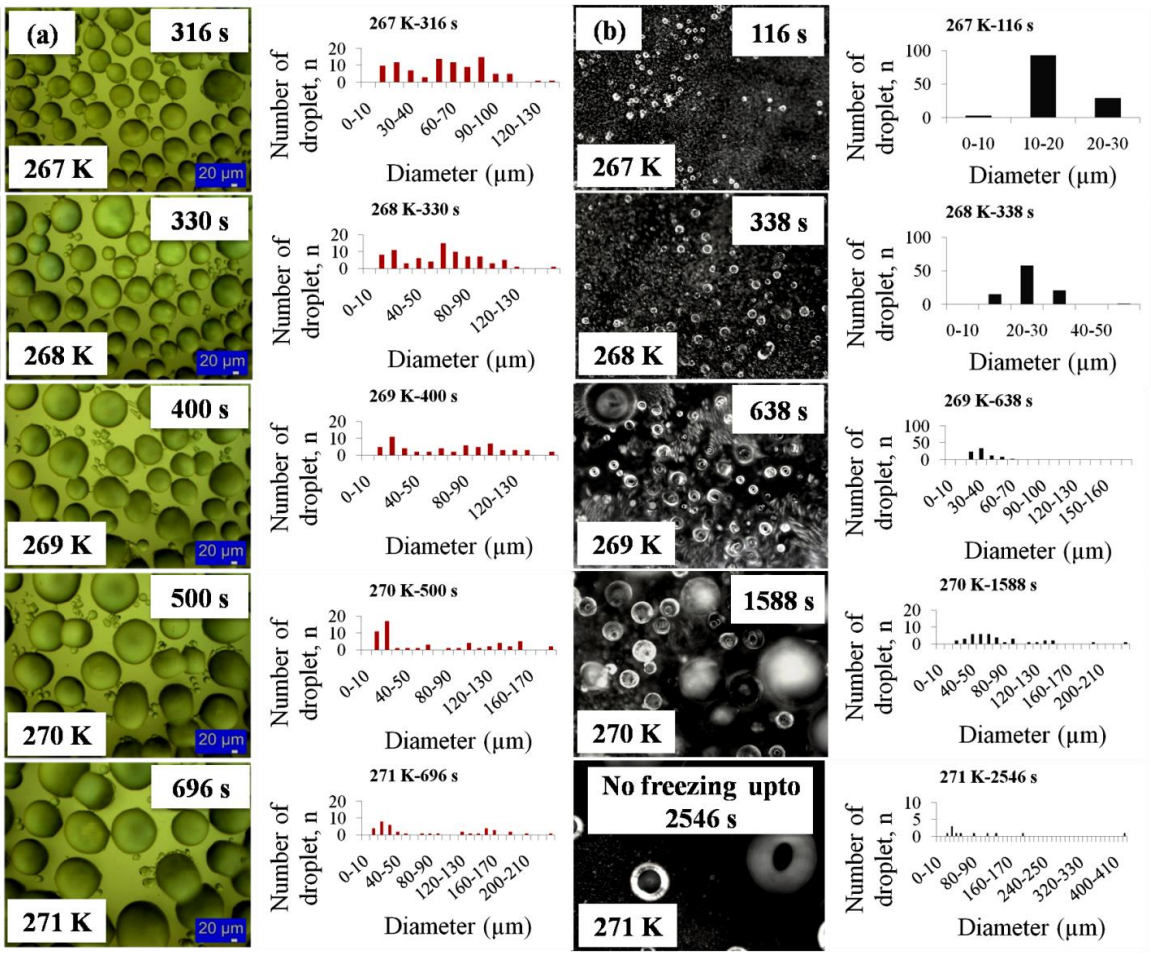

Figure 8.15 Freezing dynamics and droplet size distribution at the frozen condition for various surface temperatures (a) hydrophilic (b) hydrophobic graphene surface [119].

The suppression of the ice bridge was seen that prolongs the freezing time. Lower droplet density and less volume of frost were observed, and droplet distribution can be related to the lognormal distribution at 267 K and 269 K. The distribution shifts to bimodal for surface temperature higher than 269 K.

Maximum ~3.65× freezing delay was observed for this surface at 271 K freezing temperature. Approximate 45.12% area coverage (~less frost formation) with 1088 s (~3×) freezing delay was observed for the hydrophobic graphene surface compared to hydrophilic graphene surface at 270 K surface temperature.

8.8 Freezing dynamics for hydrophobic graphene surface and plain silicon surface

The freezing mechanism of droplets on the plain surface has been described in Figure 8.16. Freezing mechanism on hydrophobic graphene and also plain silicon surfaces for 270 K surface temperatures were described in Figure 8.17(a-c). The images in (a) have been represented until the whole hydrophobic surface appeared to be frozen. Lower occurrence of ice bridging was observed (at 1588 s). In Figure 8.17(b), the 'Jumping effect' of droplets [22, 23, 49] was also observed. In Figure 8.17(b), the solid yellow circle presents the existence of droplet while the dashed yellow circle represents the disappearance of droplets from the field of view due to the 'jumping' phenomenon.

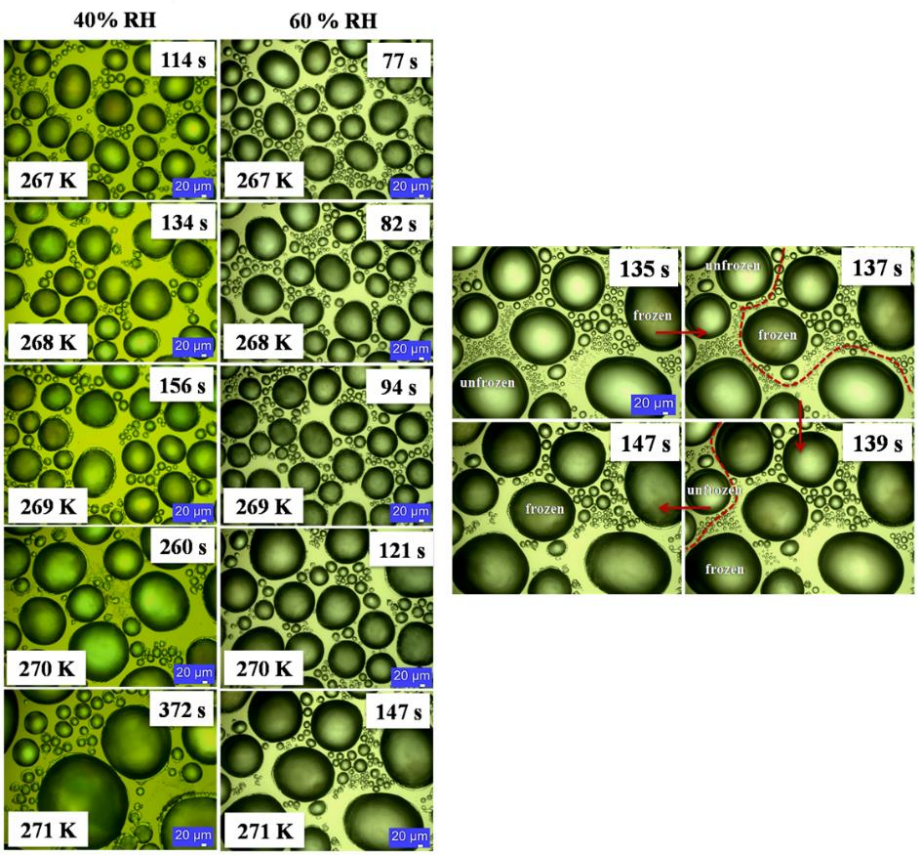

Figure 8.16 Freezing times on plain silicon surface for various surface temperatures [119].

This phenomenon reduces the droplet density, and the probability of the active ice bridge formation as droplet size distribution changes for the hydrophobic surface as stated earlier in Figure 8.15(b). In Figure 8.17(c), the plain silicon surface freezes at 121 s. Around ~13.12× freezing delay was observed for the hydrophobic graphene surface compared to the plain surface at 271 K surface temperature.

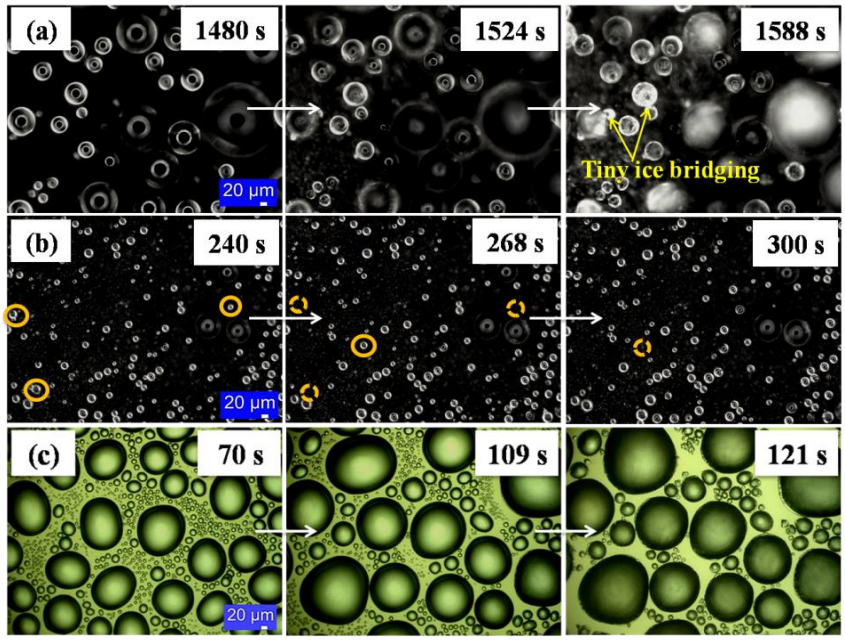

Figure 8.17 (a) Freezing dynamics for hydrophobic graphene surface at 60% RH until t=1588 s (b) droplet mobility enhances the 'jumping' phenomenon (c) the plain silicon surface at 270 K surface temperature [119].

The variation of freezing time with the surface temperature has been shown in Figure 8.18 for all the surfaces at higher humidity (60% RH). Around 1.6×, 3× and 3.65× freezing delay were observed at 269 K, 270 K, and 271 K surface temperature respectively for the coated surfaces. Around 6.78×, 13.12× and 17.32× freezing delay were observed at 269 K, 270 K, and 271 K surface temperatures respectively for the hydrophobic graphene surface compared to the plain silicon surface under same operating condition. Higher freezing time and lower surface coverage were seen for hydrophobic graphene surface. Both of the graphene coated surfaces delay the freezing compared to the plain silicon surface. At the lower freezing temperature,

although the freezing delay is not discernable, the lower volume of frost formation might be an added advantage. The red-cross mark (×) in Figure 8.18(a), indicates 'no freezing' point for the hydrophobic graphene surface until t = 2546 s at 270 K surface temperature.

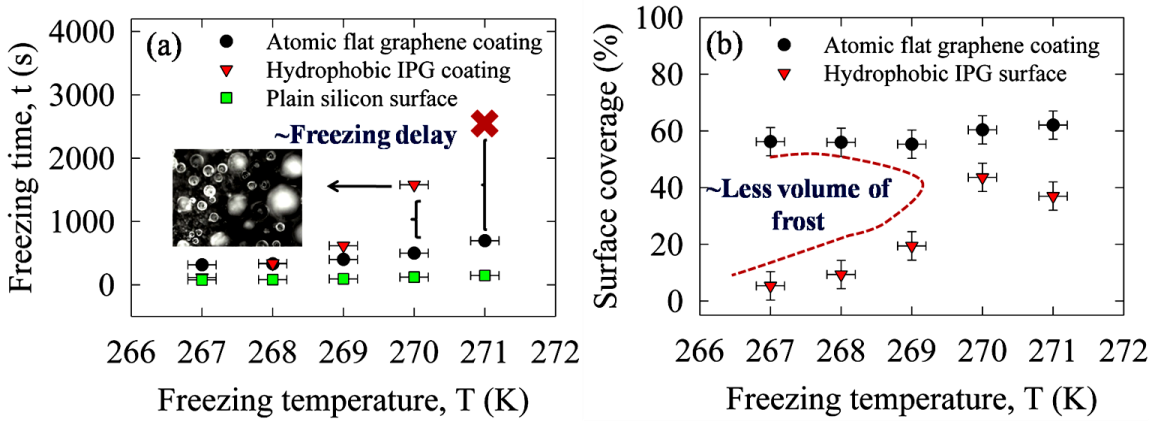

Figure 8.18 Variation of the freezing time for various surface temperatures at 60% RH [119].

8.9 Conclusion

Droplet growth on graphene surfaces goes through initial nucleation, direct growth, coalescence, and sweep off stages. At 40% RH, higher surface coverage (~ 40%) was observed for hydrophilic graphene surface compared to the inkjet-printed hydrophobic graphene surface. It is essential for condensate harvesting. The inkjet-printed hydrophobic graphene surface slows the inter-droplet wave propagation via less number of ice bridging that delays the freezing compared to the hydrophilic graphene surface at 60% RH. Maximum ~3× and ~3.65× freezing delays were observed at 270 K and 271 K surface temperatures for the hydrophobic graphene surface compared to the hydrophilic graphene surface. Around ~6.78×, ~13.12× and ~17.32× freezing delay was also observed at 269 K, 270 K, and 271 K surface temperatures for the hydrophobic coated surface compared to plain silicon surface. This portion of the work shows that the wetting

properties of graphene coatings can affect freezing delay, area coverage, ice bridging, and droplet size distribution.

Chapter 9 - Conclusions and Future work

9.1 Conclusions

The manipulation of the nucleation energy barrier to affect droplet formation can be done either by altering the surface or environmental properties of the operating system. The imaging measurements in an environmental chamber were conducted to resolve the effect of both wettability and humidity. The main outcomes-

- **Fundamental understanding of coalescence events and pinning behavior in droplet growth**

The droplet growth follows mainly nucleation, direct growth, and coalescence events. Droplet growth stages are termed as 'Direct condensation' and 'Coalescence events'. The relative importance of coalescence events in droplet final diameter calculation has been revealed through the tracking of single droplet growth. At higher humidity, the droplet growth rate is higher. At droplet interface, the higher mass transfer happens for the high humid condition. The pinning of the droplet by the nanostructured surfaces reduces the occurrences of coalescence events and changes the droplet dynamics significantly. The formulated mathematical model shows that the pinning mechanism is a function of pillar geometry and the apparent contact angle of the condensed droplet. Furthermore, the pinning by the folded edge and micro-nano structures of GO coated copper surface, changes the droplet dynamics.

- **Acceleration of freezing**

By pinning droplets, nanopillared surface can slow the rate of coalescence events resulting in the acceleration of freezing. The surface can accelerate the freezing by order of magnitude compared to the state-of-art plain surfaces. The relationship between the 'onset of

freezing' and 'Final freezing time' provides valuable insight into the design of the engineered surface.

- **Freezing front propagation**

Approximate ~3.8× freezing delay was observed for Teflon© coated hydrophobic surface at 265 K surface temperature. The durability of the coating was checked via repeated testing as well as contact angle measurements. Effective engineered graphene coating (both hydrophilic and hydrophobic), can delay the freezing by 3.65×-17.32×. The freezing delay, lower volume of condensate frost formation as well as the stability of the coated surface can be integrated in the future for significant energy savings.

9.2 Future work

The present work focuses on condensation and freezing tests in controlled environmental conditions for different engineered surfaces [82, 96, 98, 110, 115, and 119]. The study explores the role of surface structure and wettability on droplet morphology, nucleation density, droplet growth rate and departure behavior. It reveals the fundamental understanding of 'coalescence' and 'pinning' mechanism of droplet growth for the horizontally oriented surface. The 'coalescence' and 'pinning' mechanism of the droplet can be modelled numerically in future to get the temperature gradient along the droplet interface as well as the specimen to calculate the heat flux and HTC, which are still challenging through the experimental procedure. The HTC measurement in freezing is still challenging due to continuous movement of the freezing front, location and shape. The process is complex and transient that can be simulated by CFD program in future to validate the test results.

The tests can be conducted for different tilt angles of the sample to investigate the impact of droplet during the sliding of droplets by the gravity components. The test can be coupled with

forced convection to investigate the droplet sweeping, and perhaps shedding from the tilted sample. The test can also be conducted for different structured surfaces to get insights into water and heat transport for space applications.

Micro-nano structures as well as surface coating technologies has the potential to tune the surface wettability and droplet dynamics, it would be interesting to pattern the metal and chip surface in a way that would have a different wetting and droplet propagation behavior in microfluidics, desalination, water collection and freezing based applications. For the IPG graphene surface, different petal orientation can be tuned to get different wettability (CA) for frost delaying applications. Freezing tests can also be conducted inside the refrigeration system to calculate the insulation imposed by the frost accumulation as well as the corresponding pressure drop or air blockage.

For the low surface tension fluids (hydrocarbons, cryogens and fluorinated refrigerant) that has indusial applications, the condensation and freezing test results are not abundant in the existing literature. Hence, tests can be conducted in future to reveal the droplet dynamics on those surfaces.

References

[1] E. Le Fevre, "A theory of heat transfer by dropwise condensation," *in 3rd International Heat Transfer Conference,* 1966, 1966, pp. 362-375.

[2] J. Blaschke, T. Lapp, B. Hof, and J. Vollmer, "Breath figures: nucleation, growth, coalescence, and the size distribution of droplets," *Physical Review Letters*, vol. 109, p. 068701, 2012.

[3] J. Rose, "Dropwise condensation theory and experiment: a review," *Proceedings of the Institution of Mechanical Engineers, Part A: Journal of Power and Energy,* vol. 216, pp. 115-128, 2002.

[4] R. Leach, F. Stevens, S. Langford and J. Dickinson, "Dropwise condensation: experiments and simulations of nucleation and growth of water drops in a cooling system," *Langmuir*, vol. 22 (21), pp. 8864-8872, 2006.

[5] R. Narhe and D. Beysens, "Water condensation on a super-hydrophobic spike surface," *EPL (Europhysics Letters),* vol. 75 (1), p. 98, 2006.

[6] C.-H. Chen, Q. Cai, C. Tsai, C.-L. Chen, G. Xiong, Y. Yu, et al., "Dropwise condensation on superhydrophobic surfaces with two-tier roughness," *Applied Physics Letters*, vol. 90, p. 173108, 2007.

[7] R. Narhe and D. Beysens, "Growth dynamics of water drops on a square-pattern rough hydrophobic surface," *Langmuir,* vol. 23 (12), pp. 6486-6489, 2007.

[8] A. Leipertz and A. P. Fröba, "Improvement of condensation heat transfer by surface modifications," *Heat Transfer Engineering*, vol. 29, pp. 343-356, 2008.

[9] X. H. Ma, T.Y. Song, Z. Lan, and T. Bai., "Transient characteristics of initial droplet size distribution and effect of pressure on evolution of transient condensation on low thermal conductivity surface," *International Journal of Thermal Sciences*, vol. 49, pp. 1517-26, 2010.

[10] R. Wen, Z. Lan, B. Peng, W. Xu and X. Ma, "Droplet dynamics and heat transfer for dropwise condensation at lower and ultra-lower pressure," *Applied Thermal Engineering*, vol. 88, pp. 265-273, 2015.

[11] M. Mei, B. Yu, M. Zou and L. Luo, "A numerical study on growth mechanism of dropwise condensation," *International Journal of Heat and Mass Transfer*, vol. 54 (9), pp. 2004-2013, 2011.

[12] M. Mei, F. Hu, C. Han and Y. Cheng, "Time-averaged droplet size distribution in steady-state dropwise condensation", *International Journal of Heat and Mass Transfer*, vol. 88, pp. 338-345, 2015.

[13] B. S. Sikarwar, S. Khandekar and K. Muralidhar, "Mathematical modelling of dropwise condensation on textured surfaces," *Sadhana*, vol. 38 (6), pp. 1135-1171, 2013.

[14] K. Rykaczewski, J. H. J. Scott, S. Rajauria, J. Chinn, A. M. Chinn and W. Jones, "Three dimensional aspects of droplet coalescence during dropwise condensation on superhydrophobic surfaces," *Soft Matter*, vol. 7 (19), pp. 8749-8752, 2011.

[15] N. Miljkovic, R. Enright, and E. N. Wang, "Effect of droplet morphology on growth dynamics and heat transfer during condensation on superhydrophobic nanostructured surfaces," *ACS Nano*, vol. 6, pp. 1776-1785, 2012.

[16] R. Enright, N. Miljkovic, A. Al-Obeidi, C. V. Thompson, and E. N. Wang, "Condensation on superhydrophobic surfaces: the role of local energy barriers and structure length scale," *Langmuir*, vol. 28, pp. 14424-14432, 2012.

[17] T.-J. Ko, E. K. Her, B. Shin, H.-Y. Kim, K.-R. Lee, B. K. Hong, et al., "Water condensation behavior on the surface of a network of superhydrophobic carbon fibers with high-aspect-ratio nanostructures," *Carbon*, vol. 50, pp. 5085-5092, 2012.

[18] L. Yin, Y. Wang, J. Ding, Q. Wang, and Q. Chen, "Water condensation on superhydrophobic aluminum surfaces with different low-surface-energy coatings," *Applied Surface Science*, vol. 258, pp. 4063-4068, 2012.

[19] S. Anand, A. T. Paxson, R. Dhiman, J. D. Smith and K. K. Varanasi, "Enhanced condensation on lubricant-impregnated nanotextured surfaces," *ACS Nano*, Vol. 6 (11), pp. 10122-10129, 2012.

[20] J. Feng, Y. Pang, Z. Qin, R. Ma, and S. Yao, "Why condensate drops can spontaneously move away on some superhydrophobic surfaces but not on others," *ACS Applied Materials & Interfaces*, vol. 4, pp. 6618-6625, 2012.

[21] N. Miljkovic, R. Enright and E. N. Wang, "Modeling and optimization of superhydrophobic condensation," *Journal of Heat Transfer*, vol. 135(11), p. 111004, 2013.

[22] R. Enright, N. Miljkovic, N. Dou, Y. Nam, and E. N. Wang, "Condensation on superhydrophobic copper oxide nanostructures," *Journal of Heat Transfer*, vol. 135, p. 091304, 2013.

[23] N. Miljkovic and E. N. Wang, "Condensation heat transfer on superhydrophobic surfaces," *MRS bulletin*, vol. 38, pp. 397-406, 2013.

[24] K. W. Kim, S. C. Do, J. S. Ko, and J. H. Jeong, "Observation of water condensate on hydrophobic micro textured surfaces," *Heat and Mass Transfer*, vol. 49, pp. 955-962, 2013.

[25] K. Yanagisawa, M. Sakai, T. Isobe, S. Matsushita and A. Nakajima, "Investigation of droplet jumping on superhydrophobic coatings during dew condensation by the observation from two directions," *Applied Surface Science*, vol. 315, pp. 212-221, 2014.

[26] G. Li, M. H. Alhosani, S. Yuan, H. Liu, A. A. Ghaferi and T. Zhang, "Microscopic droplet formation and energy transport analysis of condensation on scalable superhydrophobic nanostructured copper oxide surfaces," *Langmuir*, vol. 30 (48), pp. 14498-14511, 2014.

[27] E. Ölçeroğlu, C.-Y. Hsieh, M. M. Rahman, K. K. Lau, and M. McCarthy, "Full-field dynamic characterization of superhydrophobic condensation on biotemplated nanostructured surfaces," *Langmuir*, vol. 30, pp. 7556-7566, 2014.

[28] K. O. Zamuruyev, H. K. Bardaweel, C. J. Carron, N. J. Kenyon, O. Brand, J.-P. Delplanque, et al., "Continuous droplet removal upon dropwise condensation of humid air on a hydrophobic micropatterned surface," *Langmuir*, vol. 30 (33), pp. 10133-10142, 2014.

[29] A. Ghosh, S. Beaini, B. J. Zhang, R. Ganguly, and C. M. Megaridis, "Enhancing dropwise condensation through bioinspired wettability patterning," *Langmuir*, vol. 30, pp. 13103-13115, 2014.

[30] F. M. Mancio Reis, P. Lavieille, and M. Miscevic, "Dropwise condensation enhancement using a wettability gradient," *Heat Transfer Engineering*, vol. 38, pp. 377-385, 2017.

[31] X. Qu, J. B. Boreyko, F. Liu, R. L. Agapov, N. V. Lavrik, S. T. Retterer, et al., "Self-propelled sweeping removal of dropwise condensate," *Applied Physics Letters*, vol. 106 (22), p. 221601, 2015.

[32] S. Chavan, H. Cha, D. Orejon, K. Nawaz, N. Singla, Y. F. Yeung, et al., "Heat transfer through a condensate droplet on hydrophobic and nanostructured superhydrophobic surfaces," *Langmuir*, vol. 32, pp. 7774-7787, 2016.

[33] H. Kim and Y. Nam, "Condensation behaviors and resulting heat transfer performance of nano-engineered copper surfaces," *International Journal of Heat and Mass Transfer*, vol. 93, pp. 286-92, 2016.

[34] D. Seo, S. Oh, S. Shin, and Y. Nam, "Dynamic heat transfer analysis of condensed droplets growing and coalescing on water repellent surfaces," *International Journal of Heat and Mass Transfer*, vol. 114, pp. 934-943, 2017.

[35] R. Wen, Z. Lan, B. Peng, W. Xu, R. Yang, and X. Ma, "Wetting transition of condensed droplets on nanostructured superhydrophobic surfaces: coordination of surface properties and condensing conditions," *ACS Applied Materials & Interfaces*, vol. 9, pp. 13770-13777, 2017.

[36] R. Wen, Q. Li, J. Wu, G. Wu, W. Wang, Y. Chen, et al., "Hydrophobic copper nanowires for enhancing condensation heat transfer," *Nano Energy*, vol. 33, pp. 177-183, 2017.

[37] A. Aili, Q. Ge, and T. Zhang, "How Nanostructures Affect Water Droplet Nucleation on Superhydrophobic Surfaces," *Journal of Heat Transfer*, vol. 139, p. 112401, 2017.

[38] Y. Zhao, D. J. Preston, Z. Lu, L. Zhang, J. Queeney and E. N. Wang, "Effects of millimetric geometric features on dropwise condensation under different vapor conditions," *International Journal of Heat and Mass Transfer*, vol. 119, pp. 931-938, 2018.

[39] D. Attinger, C. Frankiewicz, A. R. Betz, T. M. Schutzius, R. Ganguly, A. Das, et al., "Surface engineering for phase change heat transfer: A review," *MRS Energy & Sustainability-A Review Journal*, vol. 1, 2014.

[40] J. Huang, J. Zhang and L. Wang, "Review of vapor condensation heat and mass transfer in the presence of non-condensable gas," *Applied Thermal Engineering*, vol. 89, pp. 469-484, 2015.

[41] H. Hu, G. Tang, and D. Niu, "Experimental investigation of condensation heat transfer on hybrid wettability finned tube with large amount of noncondensable gas," *International Journal of Heat and Mass Transfer*, vol. 85, pp. 513-523, 2015.

[42] H. Cha, A. Wu, M.-K. Kim, K. Saigusa, A. Liu and N. Miljkovic, "Nanoscale-Agglomerate-Mediated Heterogeneous Nucleation," *Nano Letters*, vol. 17 (12), pp. 7544-7551, 2017.

[43] J. B. Boreyko, R. R. Hansen, K. R. Murphy, S. Nath, S. T. Retterer, and C. P. Collier, "Controlling condensation and frost growth with chemical micropatterns," *Scientific Reports*, vol. 6, 2016.

[44] A. S. Van Dyke, D. Collard, M. M. Derby, and A. R. Betz, "Droplet coalescence and freezing on hydrophilic, hydrophobic, and biphilic surfaces," *Applied Physics Letters*, vol. 107, p. 141602, 2015.

[45] L. Mishchenko, B. Hatton, V. Bahadur, J. A. Taylor, T. Krupenkin, and J. Aizenberg, "Design of ice-free nanostructured surfaces based on repulsion of impacting water droplets," *ACS Nano*, vol. 4, pp. 7699-7707, 2010.

[46] A. Z. Şahin, "An experimental study on the initiation and growth of frost formation on a horizontal plate," *EXPERIMENTAL HEAT TRANSFER An International Journal*, vol. 7, pp. 101-119, 1994.

[47] S. Nath, S. F. Ahmadi, and J. B. Boreyko, "A Review of Condensation Frosting," *Nanoscale and Microscale Thermophysical Engineering*, vol. 21, pp. 81-101, 2017.

[48] R. O. Piucco, C. J. Hermes, C. Melo, and J. R. Barbosa, "A study of frost nucleation on flat surfaces," *Experimental Thermal and Fluid Science*, vol. 32, pp. 1710-1715, 2008.

[49] M. He, J. Wang, H. Li, X. Jin, J. Wang, B. Liu, and Y. Song, "Super-hydrophobic film retards frost formation," *Soft Matter*, vol. 6, pp. 2396-2399, 2010.

[50] K. K. Varanasi, T. Deng, J. D. Smith, M. Hsu, and N. Bhate, "Frost formation and ice adhesion on superhydrophobic surfaces," *Applied Physics Letters*, vol. 97, p. 234102, 2010.

[51] M. He, H. Li, J. Wang, and Y. Song, "Superhydrophobic surface at low surface temperature," *Applied Physics Letters*, vol. 98, p. 093118, 2011.

[52] J. Chen, J. Liu, M. He, K. Li, D. Cui, Q. Zhang, et al., "Superhydrophobic surfaces cannot reduce ice adhesion," *Applied Physics Letters*, vol. 101, p. 111603, 2012

[53] P. Kim, T.-S. Wong, J. Alvarenga, M. J. Kreder, W. E. Adorno-Martinez, and J. Aizenberg, "Liquid-infused nanostructured surfaces with extreme anti-ice and anti-frost performance," *ACS Nano*, vol. 6, pp. 6569-6577, 2012.

[54] A. Alizadeh, M. Yamada, R. Li, W. Shang, S. Otta, S. Zhong, et al., "Dynamics of ice nucleation on water repellent surfaces," *Langmuir*, vol. 28, pp. 3180-3186, 2012.

[55] J. B. Boreyko and C. P. Collier, "Delayed frost growth on jumping-drop superhydrophobic surfaces," *ACS Nano*, vol. 7, pp. 1618-1627, 2013.

[56] Y. Wang, J. Xue, Q. Wang, Q. Chen, and J. Ding, "Verification of icephobic/anti-icing properties of a superhydrophobic surface," *ACS Applied Materials & Interfaces*, vol. 5, pp. 3370-3381, 2013.

[57] L. Mishchenko, M. Khan, J. Aizenberg, and B. D. Hatton, "Spatial control of condensation and freezing on superhydrophobic surfaces with hydrophilic patches," *Advanced Functional Materials*, vol. 23, pp. 4577-4584, 2013.

[58] K. Rykaczewski, S. Anand, S. B. Subramanyam, and K. K. Varanasi, "Mechanism of frost formation on lubricant-impregnated surfaces," *Langmuir*, vol. 29, pp. 5230-5238, 2013.

[59] D. P. Singh and J. P. Singh, "Delayed freezing of water droplet on silver nanocolumnar thin film," *Applied Physics Letters*, vol. 102, p. 243112, 2013.

[60] M. A. Rahman and A. M. Jacobi, "Condensation, frost formation, and frost melt-water retention characteristics on microgrooved brass surfaces under natural convection," *Heat Transfer Engineering*, vol. 34, pp. 1147-1155, 2013.

[61] M. A. Rahman and A. M. Jacobi, "Effects of microgroove geometry on the early stages of frost formation and frost properties," *Applied Thermal Engineering*, vol. 56, pp. 91-100, 2013.

[62] M. A. Rahman and A. M. Jacobi, "Experimental study on frosting/defrosting characteristics of microgrooved metal surfaces," *International Journal of Refrigeration*, vol. 50, pp. 44-56, 2015.

[63] P. Hao, C. Lv, and X. Zhang, "Freezing of sessile water droplets on surfaces with various roughness and wettability," *Applied Physics Letters*, vol. 104, p. 161609, 2014.

[64] G. Fang and A. Amirfazli, "Understanding the anti-icing behavior of superhydrophobic surfaces," *Surface Innovations*, vol. 2, pp. 94-102, 2014.

[65] Z.-J. Wang, D.-J. Kwon, K. L. DeVries, and J.-M. Park, "Frost formation and anti-icing performance of a hydrophobic coating on aluminum," *Experimental Thermal and Fluid Science*, vol. 60, pp. 132-137, 2015.

[66] Z. Zuo, R. Liao, C. Guo, Y. Yuan, X. Zhao, A. Zhuang, et al., "Fabrication and anti-icing property of coral-like superhydrophobic aluminum surface," *Applied Surface Science*, vol. 331, pp. 132-139, 2015.

[67] Y. Zhao and C. Yang, "Retarded condensate freezing propagation on superhydrophobic surfaces patterned with micropillars," *Applied Physics Letters*, vol. 108, p. 061605, 2016.

[68] H. Kim, D. Kim, H. Jang, D. R. Kim, and K.-S. Lee, "Microscopic observation of frost behaviors at the early stage of frost formation on hydrophobic surfaces," *International Journal of Heat and Mass Transfer*, vol. 97, pp. 861-867, 2016.

[69] Y. Zhang, M. R. Klittich, M. Gao, and A. Dhinojwala, "Delaying Frost Formation by Controlling Surface Chemistry of Carbon Nanotube-Coated Steel Surfaces," *ACS Applied Materials & Interfaces*, vol. 9, pp. 6512-6519, 2017.

[70] S. Chavan, J. Carpenter, M. Nallapaneni, J. Chen, and N. Miljkovic, "Bulk water freezing dynamics on superhydrophobic surfaces," *Applied Physics Letters*, vol. 110, p. 041604, 2017.

[71] S. Wang, W. Zhang, X. Yu, C. Liang, and Y. Zhang, "Sprayable superhydrophobic nano-chains coating with continuous self-jumping of dew and melting frost," *Scientific Reports*, vol. 7, p. 40300, 2017.

[72] Y. Zhao, R. Wang, and C. Yang, "Interdroplet freezing wave propagation of condensation frosting on micropillar patterned superhydrophobic surfaces of varying pitches," *International Journal of Heat and Mass Transfer*, vol. 108, pp. 1048-1056, 2017.

[73] S. Chavan, D. Park, N. Singla, P. Sokalski, K. Boyina, and N. Miljkovic, "Effect of Latent Heat Released by Freezing Droplets during Frost Wave Propagation," *Langmuir*, vol. 34, pp. 6636-6644, 2018.

[74] M. N. Martino, L. Otero, P. Sanz, and N. Zaritzky, "Size and location of ice crystals in pork frozen by high-pressure-assisted freezing as compared to classical methods," *Meat Science*, vol. 50, pp. 303-313, 1998.

[75] B. Li and D.-W. Sun, "Novel methods for rapid freezing and thawing of foods–a review," *Journal of Food Engineering*, vol. 54, pp. 175-182, 2002.

[76] B. Li and D.-W. Sun, "Effect of power ultrasound on freezing rate during immersion freezing of potatoes," *Journal of Food Engineering*, vol. 55, pp. 277-282, 2002.

[77] L. Zheng and D.-W. Sun, "Innovative applications of power ultrasound during food freezing processes—a review," *Trends in Food Science & Technology*, vol. 17, pp. 16-23, 2006.

[78] E. Alizadeh, N. Chapleau, M. De Lamballerie, and A. Le-Bail, "Effect of different freezing processes on the microstructure of Atlantic salmon (Salmo salar) fillets," *Innovative Food Science & Emerging Technologies*, vol. 8, pp. 493-499, 2007.

[79] H. Kiani and D.-W. Sun, "Water crystallization and its importance to freezing of foods: A review," *Trends in Food Science & Technology*, vol. 22, pp. 407-426, 2011.

[80] R. N. Bohm, A. R. Betz, and E. Kinzel, "NANOSTRUCTURED SURFACE SIGNIFICANTLY ALTERS DROPLET DYNAMICS AND FREEZING BEHAVIOR," in *ASTFE Digital Library*, 2017.

[81] Q. Zeng and S. Xu, "Thermodynamics and characteristics of heterogeneous nucleation on fractal surfaces," *The Journal of Physical Chemistry C*, vol. 119, pp. 27426-27433, 2015.

[82] M. R. Haque, C. Qu, E. C. Kinzel, and A. R. Betz, "Droplet Growth Dynamics during Atmospheric Condensation on Nanopillar Surfaces," *Nanoscale and Microscale Thermophysical Engineering*, vol. 22, pp. 270-295, 2018.

[83] D. J. Preston, D. L. Mafra, N. Miljkovic, J. Kong, and E. N. Wang, "Scalable graphene coatings for enhanced condensation heat transfer," *Nano Letters*, vol. 15, pp. 2902-2909, 2015.

[84] J. C. Hulteen and R. P. Van Duyne, "Nanosphere lithography: a materials general fabrication process for periodic particle array surfaces," *Journal of Vacuum Science & Technology A: Vacuum, Surfaces, and Films*, vol. 13, pp. 1553-1558, 1995.

[85] W. Wu, A. Katsnelson, O. G. Memis, and H. Mohseni, "A deep sub-wavelength process for the formation of highly uniform arrays of nanoholes and nanopillars," *Nanotechnology*, vol. 18, p. 485302, 2007.

[86] A. Bonakdar, M. Rezaei, R. L. Brown, V. Fathipour, E. Dexheimer, S. J. Jang, et al., "Deep-UV microsphere projection lithography," *Optics Letters*, vol. 40, pp. 2537-2540, 2015.

[87] O. Shavdina, L. Berthod, T. Kampfe, S. Reynaud, C. Veillas, I. Verrier, et al., "Large Area Fabrication of Periodic TiO2 Nanopillars Using Microsphere Photolithography on a Photopatternable Sol–Gel Film," *Langmuir*, vol. 31 (28), pp. 7877-7884, 2015.

[88] C. Qu and E. C. Kinzel, "Polycrystalline metasurface perfect absorbers fabricated using microsphere photolithography," *Optics Letters*, vol. 41, pp. 3399-3402, 2016.

[89] S. Suzuki and K. Ueno, “Apparent contact angle calculated from a water repellent model with pinning effect,” *Langmuir,* vol. 33, pp. 138-143, 2016.

[90] A. Zdziennicka, K. Szymczyk, J. Krawczyk, and B. Jańczuk, “Some remarks on the solid surface tension determination from contact angle measurements,” *Applied Surface Science,* vol. 405, pp. 88-101, 2017.

[91] I.-T. Pai, C. Leu, and M.-H. Hon, “A hierarchical structure through imprinting of a polyimide precursor without residual layers,” *Journal of Micromechanics and Microengineering,* vol. 18, p. 105005, 2008.

[92] R. N. Wenzel, “Resistance of solid surfaces to wetting by water,” *Industrial & Engineering Chemistry,* vol. 28, pp. 988-994, 1936.

[93] H. Kim, S. Yang, S. R. Rao, S. Narayanan, E. A. Kapustin, H. Furukawa, et al., “Water harvesting from air with metal-organic frameworks powered by natural sunlight,” *Science,* vol. 356, pp. 430-434, 2017.

[94] J. E. Castillo, J. A. Weibel, and S. V. Garimella, “The effect of relative humidity on dropwise condensation dynamics,” *International Journal of Heat and Mass Transfer,* vol. 80, pp. 759-766, 2015.

[95] J. W. Harris and H. Stöcker, *Handbook of mathematics and computational science:* Springer Science & Business Media, 1998.

[96] R. Bohm, M. R. Haque, C. Qu, E. C. Kinzel, and A. R. Betz, “Accelerated freezing due to droplet pinning on a nanopillared surface,” *AIP Advances,* vol. 8, p. 125228, 2018.

[97] J. Park, H.-S. Han, Y.-C. Kim, J.-P. Ahn, M.-R. Ok, K. E. Lee, et al., “Direct and accurate measurement of size dependent wetting behaviors for sessile water droplets,” *Scientific Reports,* vol. 5, p. 18150, 2015.

[98] M. R. Haque, C. Zhu, C. Qu, E. C. Kinzel, and A. R. Betz, “Experimental Investigation of Condensation and Freezing Phenomenon on Hydrophilic and Hydrophobic Titanium (Ti) Nanopillared Glass Surfaces,” *Selected for publication in a special edition of Heat Transfer Engineering from MNF-2018 conference* (Accepted).

[99] A. Geim and K. Novoselov, “The rise of graphene,” *NatureMaterials,* 6: 183–191," ed: nMarch, 2007.

[100] J. S. Bunch, *Mechanical and electrical properties of graphene sheets*: Cornell University Ithaca, NY, 2008.

[101] A. C. Neto, F. Guinea, N. M. Peres, K. S. Novoselov, and A. K. Geim, “The electronic properties of graphene,” *Reviews of Modern Physics,* vol. 81, p. 109, 2009.

[102] S. Bae, H. Kim, Y. Lee, X. Xu, J.-S. Park, Y. Zheng, et al., "Roll-to-roll production of 30-inch graphene films for transparent electrodes," *Nature Nanotechnology*, vol. 5, pp. 574-578, 2010.

[103] K. M. Shahil and A. A. Balandin, "Thermal properties of graphene and multilayer graphene: Applications in thermal interface materials," *Solid State Communications*, vol. 152, pp. 1331-1340, 2012.

[104] A. C. Ferrari and D. M. Basko, "Raman spectroscopy as a versatile tool for studying the properties of graphene," *Nature Nanotechnology*, vol. 8, p. 235, 2013.

[105] R. Chen, S. R. Das, C. Jeong, M. R. Khan, D. B. Janes, and M. A. Alam, "Co-Percolating Graphen-Wrapped Silver Nanowire Network for High Performance, Highly Stable, Transparent Conducting Electrodes," *Advanced Functional Materials*, vol. 23, pp. 5150-5158, 2013.

[106] E. P. Randviir, D. A. Brownson, and C. E. Banks, "A decade of graphene research: production, applications and outlook," *Materials Today*, vol. 17, pp. 426-432, 2014.

[107] A. C. Ferrari, F. Bonaccorso, V. Fal'Ko, K. S. Novoselov, S. Roche, P. Bøggild, et al., "Science and technology roadmap for graphene, related two-dimensional crystals, and hybrid systems," *Nanoscale*, vol. 7, pp. 4598-4810, 2015.

[108] G. Zhao, X. Li, M. Huang, Z. Zhen, Y. Zhong, Q. Chen, et al., "The physics and chemistry of graphene-on-surfaces," *Chemical Society Reviews*, vol. 46, pp. 4417-4449, 2017.

[109] N. Li and A. R. Betz, "Boiling Performance of Graphene Oxide Coated Copper Surfaces at High Pressures," *Journal of Heat Transfer*, vol. 139, p. 111504, 2017.

[110] M. R. Haque and A. R. Betz, "Atmospheric Condensation Performance of Plain Copper and Graphene Oxide Coated Copper surfaces," in *ASME 2018 16th International Conference on Nanochannels, Microchannels, and Minichannels*, 2018, pp. V001T06A002-V001T06A002.

[111] R. Liao, Z. Zuo, C. Guo, Y. Yuan, and A. Zhuang, "Fabrication of superhydrophobic surface on aluminum by continuous chemical etching and its anti-icing property," *Applied Surface Science*, vol. 317, pp. 701-709, 2014.

[112] M. Mishra and Y. Yagci, *Handbook of vinyl polymers: radical polymerization, process, and technology: CRC press*, 2008.

[113] M. M. Derby, A. Chatterjee, Y. Peles, and M. K. Jensen, "Flow condensation heat transfer enhancement in a mini-channel with hydrophobic and hydrophilic patterns," *International Journal of Heat and Mass Transfer*, vol. 68, pp. 151-160, 2014.

[114] J. R. Davis, *Corrosion of aluminum and aluminum alloys: Asm International*, 1999.

[115] M. R. Haque and A. R. Betz, “Frost Formation on Aluminum and Hydrophobic Surfaces,” in *ASME 2018 16th International Conference on Nanochannels, Microchannels, and Minichannels*, 2018, pp. V001T04A001-V001T04A001.

[116] T. Chen, Q. Cong, Y. Qi, J. Jin, and K.-L. Choy, “Hydrophobic durability characteristics of butterfly wing surface after freezing cycles towards the design of nature inspired anti-icing surfaces,” *PloS One*, vol. 13, p. e0188775, 2018.

[117] J. B. Boreyko, B. R. Srijanto, T. D. Nguyen, C. Vega, M. Fuentes-Cabrera, and C. P. Collier, “Dynamic defrosting on nanostructured superhydrophobic surfaces,” *Langmuir*, vol. 29, pp. 9516-9524, 2013.

[118] S. R. Das, S. Srinivasan, L. R. Stromberg, Q. He, N. Garland, W. E. Straszheim, et al., “Superhydrophobic inkjet printed flexible graphene circuits via direct-pulsed laser writing,” *Nanoscale*, 2017.

[119] M. R. Haque, S. R. Das, A. R. Betz, “Experimental Investigation of Condensation and Freezing Phenomena on Hydrophilic and Hydrophobic Graphene Coating,” *Applied Thermal Engineering*, vol. 160, 113987, 2019.

[120] S. Nath and J. B. Boreyko, “On localized vapor pressure gradients governing condensation and frost phenomena,” *Langmuir*, vol. 32, pp. 8350-8365, 2016.

[121] D. M. Murphy and T. Koop, “Review of the vapour pressures of ice and supercooled water for atmospheric applications,” *Quarterly Journal of the Royal Meteorological Society*, vol. 131, pp. 1539-1565, 2005.

Appendix A. Surface characteristics

Table A.1 Summary of different samples with CA.

Engineered surface	Fabrication method	Wettability	Applications
(a) Silica nanopillar on silicon coated glass surface and (b) Plain silicon surface [82]	MPL process (reusable microsphere array, scalable-low-cost large area patterning with flexible, and high-throughput fabrication of infrared metasurfaces)	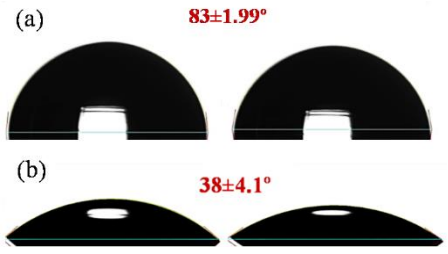	➢ Condensate harvesting ➢ Time management in water collection at arid and dry regions
Silica nanopillar on silicon coated glass surface and Teflon© coated silicon surface [96]	MPL and spray coating process	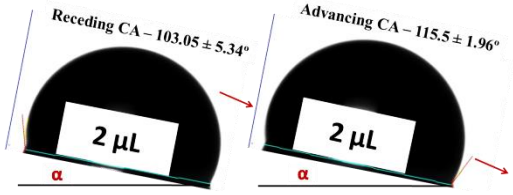 CA of water on Teflon© coated silicon surface	➢ Would reduce the daily power consumption for freezing based food processing, agricultural processing, and desalination.
(a) Titanium (Ti) nanopillar-ed glass surface and (b) Teflon© coated Ti pillared surface [98]	MPL process and spray coating	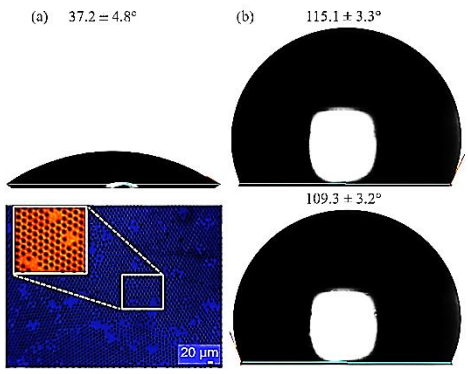	➢ Reduce power in desirable freezing ➢ Promote dropwise condensation

Plain copper and Graphene Oxide (GO) coated copper surface [110]	Spray coating of Graphene Oxide (GO) solution on copper	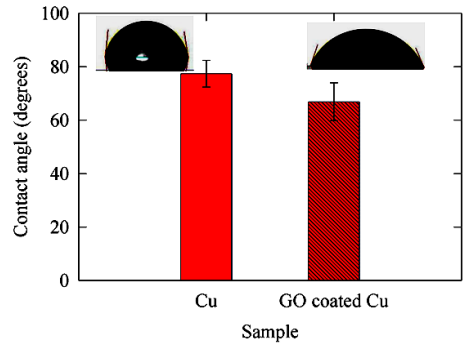	➢ Condensate harvesting
Aluminum (Al) and Hydrophob -ic Aluminum (Al-H) surface [115]	Dip coating of Teflon solution on Al surface	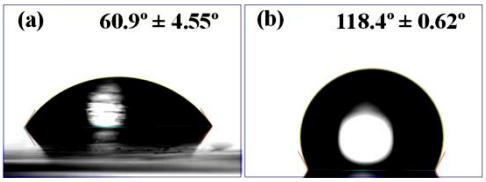	➢ Frost delaying for the surfaces of a car windshield, airplanes, air-conditioning duct, transportation, refrigeration, and other structures
Hydrophili c and Hydrophob ic Graphene (IPG) coating [119]	CVD and IPG with DPLW	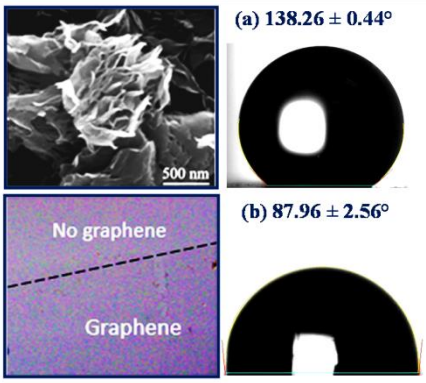	➢ Promotion of dropwise condensation for typical industrial systems such as condenser unit etc. ➢ Frost delaying

Appendix B. Summary of the current work

Table B.1 Summary of the present work.

Engineered surface	Condensation /Freezing	Outcomes	Applications
Silica nanopillar on silicon coated glass surface [82]	condensation	➢ The pinning effect suppresses the coalescence of droplets ➢ Pinning mechanism is the function of pillar diameter, height, spacing, and apparent contact angle of a droplet ➢ ~12.87% and ~24.13% increment of surface coverage compared to plain silicon surface	➢ Condensate harvesting ➢ Time management in water collection at arid and dry regions
Silica nanopillar on silicon coated glass surface [96]	freezing	➢ One order of magnitude acceleration of freezing compared to a plain silicon surface ➢ Significant acceleration of freezing compared to Teflon© coated silicon surface although the wetting properties (CA) are quite similar	➢ Would reduce the daily power consumption for freezing based applications
Titanium (Ti) nanopillared glass surface [98]	condensation/ freezing	➢ Higher (~95%) surface coverage for the pillared surface at 60% RH compared to 40% RH ➢ Pinning effect is controlled by the pillar dimensions (diameter, height, and spacing) ➢ Teflon© coated pillared surface promotes dropwise condensation ➢ Acceleration of freezing compared to plain surface	➢ Reduce power is desirable in freezing applications ➢ Promote dropwise condensation, such as for the condenser surfaces in industrial power plant applications
Plain Copper and Graphene	condensation	➢ The pinning effect caused by the micro/nanostructures of	➢ Condensate harvesting

Oxide (GO) coated copper surface [110]		the graphene flakes ➢ Approximate 95% surface coverage was observed for GO coated copper surface compared to the plain copper surface ➢ At 60% RH, the maximum average diameter of the droplet was ~ 88 µm for plain copper and ~ 111 µm for GO coated surface; droplet density appears similar ➢ The contribution of the coalescence mechanism in droplet growth was found more significant for 60% RH compared to 40% RH	
Aluminum (Al) and Hydrophobic Aluminum (Al-H) surfaces [115]	condensation /frosting	➢ At 60% RH, surface froze faster than 40% RH ➢ The Al and Al-H surface required 6.5 ± 1 and 10 ± 1 minutes ➢ Around ~8.83% decrement of average contact angle during durability check ➢ Protective coatings can mitigate the negative aspects (oxidation etc.) of Aluminum	➢ Frost delaying for the surfaces of a car windshield, airplanes, air-conditioning duct, transportation, refrigeration, and other structures
Hydrophilic and Hydrophobic Graphene (IPG) coating [119]	Condensation /frosting	➢ Hydrophobic IPG surface ➢ Maximum ~3× and ~3.65× freezing delays were observed for hydrophobic graphene compared to hydrophilic graphene ➢ Around ~6.78×, ~13.12× and ~17.32× freezing delay was observed for the hydrophobic graphene compared to plain silicon surface	➢ Applications in the thermal system ➢ Promotion of dropwise condensation for typical industrial systems (condenser unit) ➢ Frost delaying mechanism on hydrophobic graphene coating can be useful for the surfaces of turbine blades, aircraft, antennas, boats, or electronic devices.